Investigation on the integration of a cross polarization interference canceller (XPIC) into a Nokia specific digital radio system

Driesen, B.

Award date:
2001

TECHNISCHE UNIVERSITEIT EINDHOVEN

FACULTEIT ELEKTROTECHNIEK

LEERSTOEL Signal Processing Systems

Investigation on the Integration of a cross Polarization Interference Canceller (XPIC) into a Nokia specific Digital Radio System

B. Driesen

SPS 06-01

Verslag van een afstudeerproject verricht binnen de leerstoel Signal Processing Systems , o.l.v. prof.dr.ir. J.W.M. Bergmans en dr.ir. D. Gaschler in de periode november 2000 – augustus 2001

Eindhoven, augustus 2001

Investigation on the Integration of a Cross Polarization Interference Canceller (XPIC) into a Nokia specific Digital Radio System

by Bas Driesen

Preface

The compilation of this report is the result of my master thesis at the Department of Electrical Engineering at the Eindhoven University of Technology. The empirical research was done at and sponsored by Nokia Networks in Düsseldorf Germany. During November 1st 2000 to August 21st 2001 I have been working with the Radio Architecture and Integration Team of the System Competence Area. They have been great colleagues and with some of them I spent some enjoyable moments after working-hours. Team, thanks for the nice atmosphere and for your support.

I would like to thank my supervisor, Prof. Dr. Ir. J.W.M. Bergmans of the Signal Processing Systems Group in Eindhoven, for his useful critics and his cooperation. I would also like to thank my supervisor at Nokia, Dr. Ir. D. Gaschler of the Radio Architecture and Integration Team, for the fruitful discussions and for being a great source of inspiration. I am grateful to the both of them for proofreading my manuscript, which enabled me to make it magnitudes better.

Furthermore I would like to thank my family for all their love, support and encouragement. Finally I would like to express my gratitude to my dear girlfriend, for her patience and understanding, especially in times when thoughts about the thesis controlled the weekends.

Bas Driesen
Düsseldorf, August 10th 2001

Abstract

Bandwidth efficiency of digital radio systems can be increased when the horizontal and vertical polarization of the antenna are used. All kind of factors can influence the degree of orthogonality between the polarization directions, resulting in interference in each direction. To preserve receiver operation it is necessary to consider techniques that cancel this interference. A Cross Polarization Interference Canceller (XPIC) is able to achieve just this.

Integrating an XPIC into an existing radio architecture involves dealing with many problems. This report deals with the interaction between XPIC, Automatic Gain Control (AGC), Adaptive Transversal Equalizer (ATE) and Phase Estimator (PE) under different channel assumptions. Additionally, timing differences between horizontally and vertically polarized receiver and frequency variations in the oscillators of the transmitters and receivers are studied.

Still, some remaining matters should be subjected to future research. Especially the influence of interference on the slow (non-decision aided) loops and the pilot detection module should be investigated.

Table of Contents:

1. Introduction

The increasing demand in voice and high-speed data traffic tends to provoke a saturation of the spectrum in digital radio systems, furthermore events such as spectral pricing are more and more common. These are two reasons for implementing systems with higher spectral efficiency. Efficient bandwidth utilization can be obtained by using high-level modulation techniques. Nowadays multilevel Quadrature Amplitude Modulation (QAM) and Trellis Coded Modulation (TCM) schemes are widely used.

Another interesting way to provide higher bandwidth efficiency is co-channel operation or frequency re-use. This technique enables the transmission of two separate channels on the same carrier frequency, using the horizontal and the vertical polarization of the antenna. This technique can double the capacity of the system compared to conventional radio systems. The transmission in orthogonal polarizations works well as long as the discrimination between the two polarization directions is sufficiently high. This requires ideal antennas and operation of the radio under ideal propagation conditions. However, Cross Polarization Interference (XPI) is caused due to various phenomena like rainfall, multipath propagation and equipment imperfections. Together with Inter Symbol Interference (ISI) this may cause serious impairments in detection.

To ensure proper operation it is necessary to introduce techniques that increase the Cross Polarization Discrimination (XPD). Taking into account the time-varying nature of the involved phenomena it is interesting to consider an adaptive structure to cancel the XPI, such a structure is called Cross Polarization Interference Canceller (XPIC). Often they work in cooperation with an ISI-reducing Adaptive Transversal Equalizer (ATE). A global structure of a dual polarized digital radio system with XPIC and ATE may look like Figure 1 [1], [2], [3].

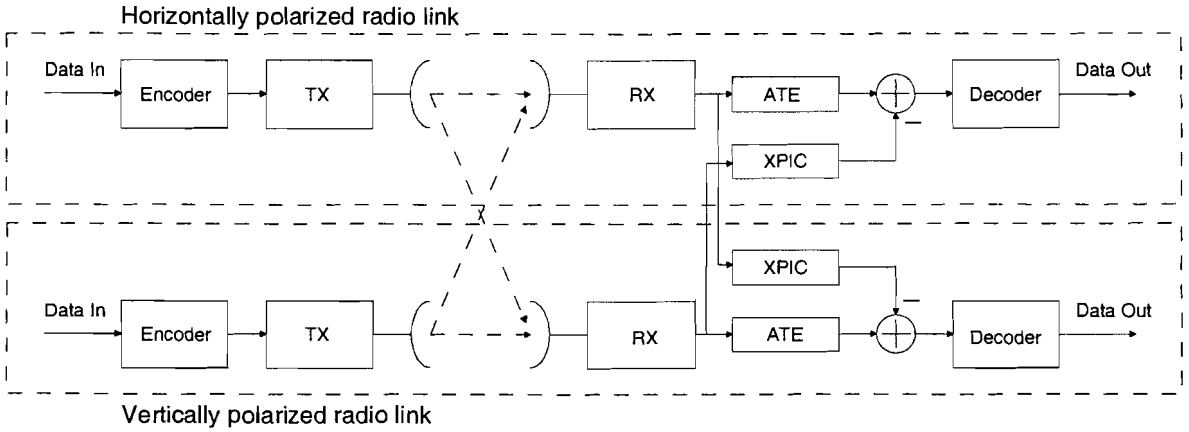

Figure 1: Global structure of a dual-polarized radio

Co-Channel (CC) operation is interesting because it doubles the capacity of the transmission link without increasing the number of modulation levels. To be able to

achieve comparable performance (bit error rate) for co-channel systems as for single polarized radio systems an XPIC needs to be introduced in the receiver.

The XPIC is a well-known subject in literature, with lot of discussions devoted to it. Especially upgrading the available single polarized radio to a dual polarized radio has been a major issue. The main reason for this is that the product can be sold as a single polarized radio system when less capacity is needed and as a dual polarized radio system when more capacity is needed. Allowing the customer to buy a single polarized radio system first and maybe upgrading it to a dual polarized radio system in the future. Operation of a dual polarized radio system comprises of two interconnected radios, this means that the single polarized radio system needs to be compatible with the dual polarized radio system. Just like other manufacturers Nokia is interested in upgrading its radio system. However there are of course some differences between the Nokia radio system and the radio systems described in the literature.

In this study the integration of an XPIC into a Nokia specific digital radio system is investigated. Interactions between XPIC, Automatic Gain Control (AGC), Phase Estimator (PE) as well as the ATE are studied. Furthermore the XPIC's performance and the system's performance are measured under different channel conditions and equipment imperfections.

First the Nokia specific digital radio system is explained in Chapter 2. After that some fundamentals of adaptive filter theory are recalled in Chapter 3, necessary for a deeper understanding of the XPIC. Then Chapter 4 elaborates on the XPIC and a basic simulation model is derived. Chapter 5 treats the studied aspects as mentioned in the former paragraph on the basis of simulations, verified by theoretical analyses. Additionally, it provides an overview of the corresponding findings in the literature. Finally Chapter 6 and Chapter 7 give the conclusions and the recommendations of this study.

2. Short Haul Digital Line-of-sight Radio Relay Systems

Short Haul Digital Line-of-sight Radio Relay Systems are radios used for point-to-point communication with a range of typically less than 5 kilometers. Figure 2 depicts such a digital radio system.

Figure 2: Digital radio system

Nowadays digital radio systems have become cheaper and furthermore their capacity has grown, therefore more and more applications use radio connections for high-speed point-to-point communication. A configuration where they are often seen in is a GSM/UMTS network. A common structure is depicted in Figure 3.

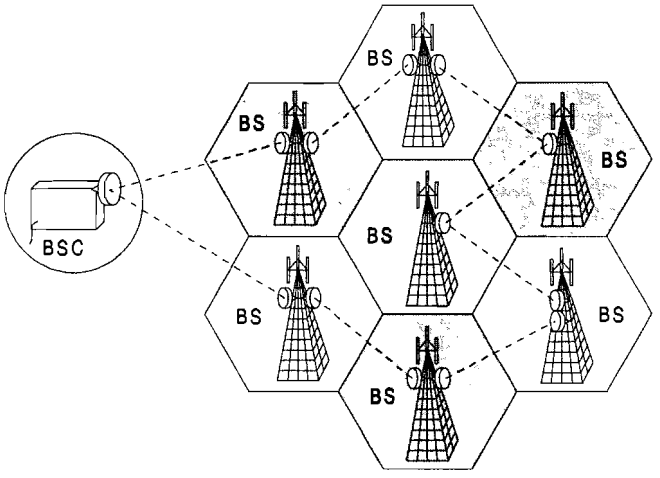

Figure 3: Line-of-sight radio in GSM/UMTS network

Advanced data services require accurate frequency and timing distribution over the telecommunication network nodes. Two types of network nodes can be distinguished, namely nodes that multiplex several channels, called multiplex nodes, and nodes that redirect the channels to different locations, called switching nodes. At the moment providers are using Synchronous Digital Hierarchy (SDH) to synchronize their network structures, whereas they used to use Plesiochronous Digital Hierarchy (PDH).

The PDH standard only partly synchronizes the network structure. Switching nodes are synchronized through a master clock, but multiplex nodes work on independent high-

precision clocks. This was thought to be the most promising solution, because the costs of very accurate quartz or atomic oscillators was foreseen to decrease progressively. But stabilization of the oscillator costs and more stringent synchronization requirements, caused by increasing data rates, made it necessary to search for more accurate solutions.

The SDH standard synchronizes every part of the network structure with the same extremely accurate master clock and is therefore more precise. The frames and signals in such a system are named Synchronous Transport Modules (STM) and several levels are defined. All levels are integer multiples of STM-1 (155,520 Mb/s) and are logically named STM-x, where x is an integer, so e.g. STM-4 = 4 * STM-1 [4]. Digital line-of-sight radio systems normally have STM-1 capacity.

2.1 Nokia specific digital radio system

An overview of a typical Nokia line-of-sight radio is given in Figure 4 and Figure 6. The specific blocks in transmitter and receiver are described next.

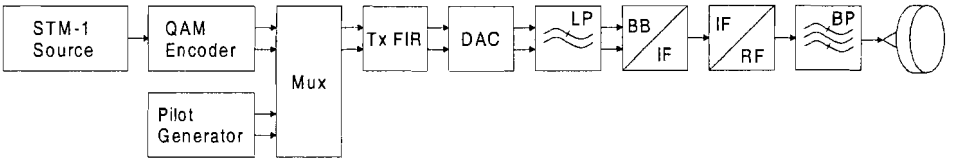

Figure 4: Transmitter overview

The transmitter consists of an STM-1 source followed by the M-ary QAM encoder. The encoder comprises an M-symbol alphabet in which $^{2}\log M$ bits of data are mapped to a symbol. The alphabet can be expressed as a constellation diagram, where the horizontal axis represents the in-phase component and the vertical axis the quadrature component. The M symbols have equal distance in this plane, as depicted in Figure 5 for 16 QAM [5]. The in-phase component is interpreted as the real symbol part and the quadrature component is interpreted as the imaginary symbol part. Real and imaginary symbol parts are handled separately in the next blocks, together they form the complex baseband signal.

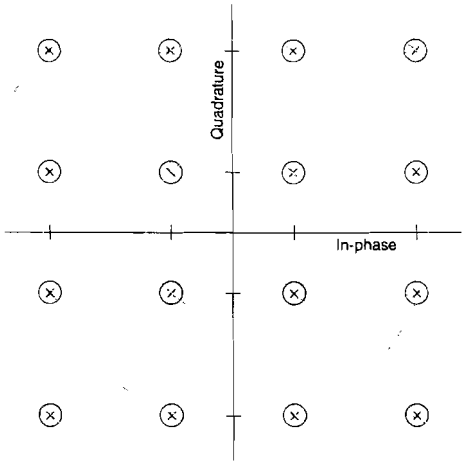

Figure 5: Constellation diagram of 16 QAM

The data symbols are then multiplexed with a predefined symbol sequence generated by the pilot generator. This symbol sequence is a QPSK modulated pseudo-random bit sequence. Each QPSK modulated symbol is called a pilot. The fixed distance between two pilots after multiplexing is called the pilot spacing. At the receiver side these pilots function as a training sequence for several blocks.

Next the pulses of the multiplexed symbol stream are shaped by the Tx FIR pulse shaping filter. The Tx FIR pulse shaping filter is designed in a way minimizing the Inter Symbol Interference (ISI). ISI occurs due to the bandlimited nature of the channel. The most popular pulse shaping filter used in mobile communication is the raised cosine filter. The optimal configuration in the sense of best SNR is achieved when the transfer function is equally divided between transmitter and receiver, resulting in a root raised cosine filter on both sides [5].

At this point the digital baseband signal is converted to an analog signal by a digital to analog converter. The analog baseband (BB) signal is converted into an Intermediate Frequency (IF) signal, after lowpass filtering to suppress the spectral replica of the baseband signal. Finally an up-converter converts the IF signal into a Radio Frequency (RF) signal, which is transmitted after final bandpass filtering.

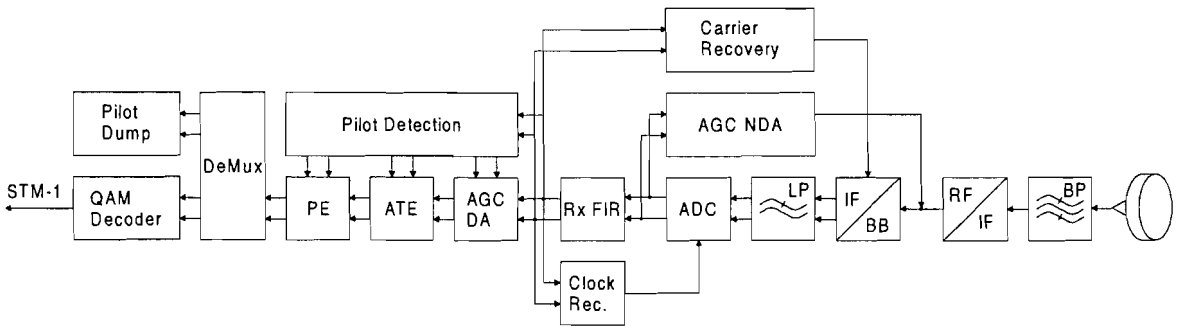

Figure 6: Receiver overview

Once the signal arrives at the receiver the opposite actions are performed. The signal is first bandpass filtered, then down-converted from RF to IF, demodulated from IF to baseband and converted into a digital signal by an analog to digital converter after a lowpass filtering process.

Rx FIR performs the second half of the pulse shaping and clock recovery extracts the clock from the baseband signal. All digital blocks work on this extracted clock. The Non Decision Aided (NDA) Automatic Gain Control (AGC) is a rough normalization of the gain on reducing the dynamic ranges of the signal in the receiver blocks. Non ideal oscillators in down-converter and demodulator result in a baseband signal with zero-frequency offset. Large zero-frequency offsets are first in slow steps decreased by the software of the receiver until a certain range in the order of 100 kHz is reached. At that point the carrier recovery removes the remaining frequency offset from the baseband signal. When the frequency offset is equal or less than 20 kHz pilot detection can take place.

The task of the pilot detection is to detect the sample position of the pilots and to regenerate the same pilot sequence as in the transmitter. These pilots then serve as a reference for adjacent blocks to perform their specific error measurement.

When the pilots are regenerated the remainder of the receiver starts to function, because these are all Decision Aided blocks (DA) relying on the regenerated pilots for their corresponding error measurements. The DA Automatic Gain Control (AGC) then corrects the remaining gain offset of the baseband signal by comparing the regenerated pilot symbols with the pilot symbols in the baseband signal.

Next the Adaptive Transversal Equalizer (ATE) suppresses the ISI caused by multipath propagation. The ATE in this example is an adaptive filter structure that adjusts its coefficients minimizing an error on every pilot symbol. The FIR filter structure should adapt in ideal circumstances to the inverse system function of the channel.

Afterwards the PE estimates and compensates the remaining phase noise that is not compensated by the carrier recovery loop. The carrier recovery loop is only able to track relatively slow phase changes, due to its relatively small loop bandwidth. Whereas the PE is able to compensate for the fast phase noise by comparing the regenerated pilots with the ISI free pilots in the baseband data stream, resulting in an estimated phase error. At the end the data symbols are de-rotated according to estimated phase error.

Finally the data symbols and the pilot symbols are de-multiplexed. The pilot symbols are discarded and the data symbols are mapped to the corresponding bits by the M-ary QAM decoder.

3. Fundamentals of adaptive filter theory

This Chapter recalls some well-known concepts from the Wiener filter theory and leads to Least Mean Square (LMS) algorithm used by the XPIC.

3.1 Wiener filters

Wiener filters are the class of linear discrete-time filters that provide estimates of a desired response, given a set of input samples, such that the mean-square value of the difference between the desired signal and estimate (estimation error) is minimized. Next the estimate or filter response at time n is denoted by $y(n)$, the desired response by $d(n)$, the input by $u(n)$, the filter coefficients by $w_0, w_1, w_2, \ldots$, and the estimation error by $e(n)$. Figure 7 represents the Wiener filter problem.

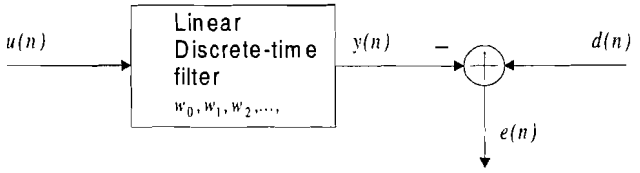

Figure 7: Block diagram representing Wiener filter problem

The filter problem is greatly simplified if a FIR filter structure is used, to perform the estimation of the desired response. Figure 8 gives the simplification of the Wiener filter problem, the output of the filter can then be expressed as

$$y(n) = \sum_{k=0}^{M-1} w_k^* u(n-k) \qquad (1)$$

where the asterisk represents complex conjugation.

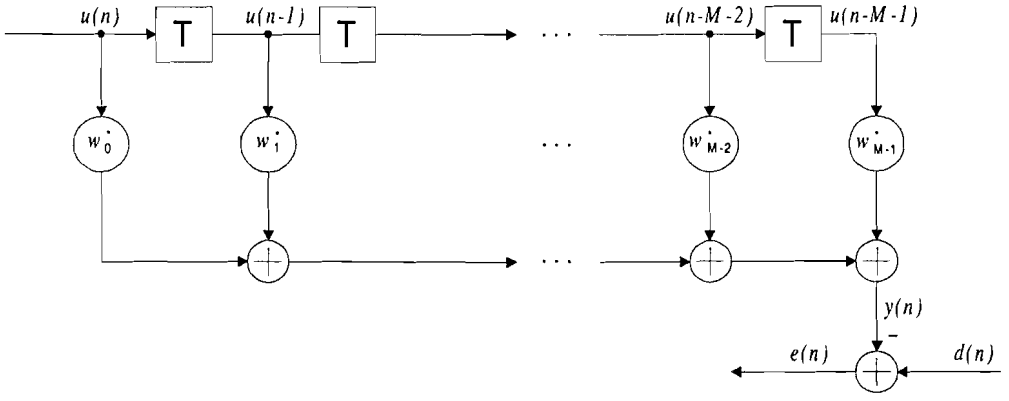

Figure 8: Wiener filter problem with FIR structure

The estimation error can be expressed as

$$e(n) = d(n) - y(n). \tag{2}$$

To optimize the filter the mean squared value of the estimation error as in Eq. (3) must be minimized.

$$J = E\left[|e(n)|^2\right] = E\left[e(n)e^*(n)\right] \tag{3}$$

where E denotes the statistical expectation across infinite ensembles. A minimum occurs when the derivative of the estimation error with respect to the filter coefficients becomes zero. The 1st derivative with respect to the k^{th} tap coefficient of the estimation error can be shown to be

$$\nabla_k J = -2E\left[u(n-k)e^*(n)\right]. \tag{4}$$

Equating Eq. (4) to zero states condition (5) leading to the optimum filter coefficients.

$$E\left[u(n-k)e^*(n)\right] = 0, \qquad k=0,1,2,\ldots \tag{5}$$

Reformulating this condition by expressing the estimation error in the desired response and the filter output, and then substituting Eq. (1) in (5) gives

$$E\left[u(n-k)\left(d^*(n) - \sum_{i=0}^{M-1} w_{i,opt}u^*(n-i)\right)\right] = 0, \qquad k=0,1,2,\ldots \tag{6}$$

where $w_{i,opt}$ stands for the i^{th} optimal filter coefficient. Expanding this expression and rearranging the terms leads to

$$\sum_{i=0}^{M-1} w_{i,opt} E\left[u(n-k)u^*(n-i)\right] = E\left[u(n-k)d^*(n)\right], \qquad k=0,1,2,\ldots \tag{7}$$

The first expectation of Eq. (7) can be interpreted as the autocorrelation of the filter input $r(i-k) = E\left[u(n-k)u^*(n-i)\right]$ and the second as the cross-correlation between the filter input and the desired response $\rho(-k) = E\left[u(n-k)d^*(n)\right]$. Thus the system of equations (7) can be rewritten as

$$\sum_{i=0}^{M-1} w_{i,opt} r(i-k) = \rho(-k), \qquad k=0,1,2,\ldots \tag{8}$$

These equations are known as the Wiener-Hopf equations for the specific case of a FIR structure. They define the optimum filter coefficients in terms of two correlation functions. The system of equations (8) can be formulated into a matrix form, which gives a more convenient notation. First of all let **R** denote the M-by-M correlation matrix of the tap inputs

$$\mathbf{R} = E\left[\mathbf{u}(n)\mathbf{u}^H(n)\right] = \begin{bmatrix} r(0) & r(1) & \cdots & r(M-1) \\ r^*(1) & r(0) & \cdots & r(M-2) \\ \vdots & \vdots & & \vdots \\ r^*(M-1) & r^*(M-2) & \cdots & r(0) \end{bmatrix} \tag{9}$$

where $\mathbf{u}(n)$denotes the M-by-1 tap-input vector, defined as

$$\mathbf{u}(n) = [u(n), u(n-1), \ldots, u(n-M+1)]^T \tag{10}$$

the superscript T stands for the transposition operation and the superscript H stands for the Hermitian adjoint or the conjugated transposed. Second let $\boldsymbol{\rho}$ denote the M-by-1 cross-correlation vector between the tap-inputs and the desired response

$$\boldsymbol{\varrho} = E\left[\mathbf{u}(n)d^*(n)\right] = [\rho(0) \quad \rho(-1) \quad \cdots \quad \rho(1-M)]^T. \tag{11}$$

Now the Wiener-Hopf equations can be rewritten in the compact matrix notation form:

$$\mathbf{R}\mathbf{w}_{opt} = \boldsymbol{\varrho}, \tag{12}$$

where $\mathbf{w}_{opt}$ denotes the M-by-1 optimum tap-weight vector defined as

$$\mathbf{w}_{opt} = \left[w_{opt,0}, w_{opt,1}, \ldots, w_{opt,M-1}\right]^T. \tag{13}$$

Premultiplying both sides with the inverse of the autocorrelation matrix $\mathbf{R}^{-1}$ assuming that the autocorrelation matrix $\mathbf{R}$ is nonsingular will lead to the solution to the Wiener-Hopf equations

$$\mathbf{w}_{opt} = \mathbf{R}^{-1}\boldsymbol{\varrho}. \tag{14}$$

For the computation of the optimum tap-weights the autocorrelation matrix $\mathbf{R}$ and the cross-correlation vector $\boldsymbol{\rho}$ must be known. Solving the Wiener-Hopf equations directly requires a lot of computational power and presents therefore serious difficulties, especially when the filter consist of a large number of tap weights and when the input data rate is high. In the next subchapter the method of steepest decent is described; an alternative procedure for computing the optimal filter coefficients in a recursive fashion. That is calculating the tap-weights starting from an initial value and improving it iteratively. Eventually the values will converge to the Wiener-Hopf solution [6].

When studying a filter problem it is useful to have a simple expression for the minimum of the mean squared error. Inserting the optimum tap-weights into Eq. (1) results in an optimal filter output

$$y_{opt}(n) = \mathbf{w}_{opt}^{H}\mathbf{u}(n). \tag{15}$$

When the linear discrete-time filter in Figure 8 operates in optimum condition the estimation error takes on the following form

$$e_{opt}(n) = d(n) - y_{opt}(n). \tag{16}$$

The minimum mean squared error is then defined by

$$J_{\min} = E\left[e_{opt}(n)e_{opt}^{*}(n)\right]. \tag{17}$$

Substituting Eq. (16) into Eq. (17) and using Eq. (15) and Eq. (14) leads to

$$J_{\min} = \sigma_d^2 - \varrho^H \mathbf{R}^{-1}\varrho. \tag{18}$$

This definition shows the minimum mean squared error in terms of the variance of the desired response σ_d^2, the autocorrelation matrix $\mathbf{R}$ and the cross-correlation vector ρ [6].

3.2 Method of Steepest Decent

The method of steepest decent is an optimization technique that is based on gradient adaptation. The gradient derived in the previous chapter can be written in the following matrix notation

$$\nabla\mathbf{J}(n) = -2\varrho + 2\mathbf{R}\mathbf{w}(n) \tag{19}$$

where $\nabla\mathbf{J}(n)$ is the M-by-1 gradient vector defined by

$$\nabla\mathbf{J}(n) = [\nabla_0 J(n) \quad \nabla_1 J(n) \quad \cdots \quad \nabla_{M-1} J(n)]^T \tag{20}$$

and in which $\mathbf{w}(n)$ is the instantaneous tap-weight vector at time n defined by

$$\mathbf{w}(n) = [w_0(n) \quad w_1(n) \quad \cdots \quad w_{M-1}(n)]^T. \tag{21}$$

It can be shown that the mean squared estimation error J of Eq. (3) is a squared function of the tap-weights. The mean squared estimation error can therefore be seen as a multi-dimensional parabolic-shaped surface with respect to the tap-weights. A property of a parabola is that its gradient always points away from its minimum. The method of steepest decent uses this information in a recursive way. Adding a small fraction of the negative error gradient to the old tap-weight vector forms a new tap-weight vector. Proceeding in an iterative way will finally result into the optimal filter coefficients. Accordingly the updated value of the tap-weight vector at time n +1, the tap-weight vector at time n and the mean squared error gradient vector at time n form the recursive relation

$$\mathbf{w}(n+1) = \mathbf{w}(n) + \frac{1}{2}\mu[-\nabla \mathbf{J}(n)] \tag{22}$$

where μ is called the step-size parameter and is a positive real-valued constant. The factor ½ is used merely to cancel the factor 2 in the error gradient. Now substituting Eq. (19) in (22) gives the final form of the update algorithm [6]

$$\mathbf{w}(n+1) = \mathbf{w}(n) + \mu[\varrho - \mathbf{R}\mathbf{w}(n)], \qquad n=0,1,2,\ldots \tag{23}$$

3.3 The Least-Mean-Square Algorithm

The Least-Mean-Square (LMS) algorithm differs form the method of steepest decent, it does not compute the actual mean squared error gradient vector, but it calculates an instantaneous estimate of this vector. The big advantage is that this does not require any prior knowledge about the correlation matrix **R** of the tap inputs and the cross-correlation vector ρ of the tap inputs and the desired response. However the drawback of this algorithm is that the tap-weights approach the Wiener solution, but will never exactly reach it. In general there will be always a random motion around the minimum of the estimation error surface, causing a misadjustment. This means the final value of the mean-squared error J consist of the minimum mean squared error J_{min} plus an excess mean squared error J_{ex}, due to the instantaneous estimate of the gradient vector. When the expectation operation in the gradient vector of Eq. (4) is left out, it will result in the instantaneous estimate of the gradient vector

$$\hat{\nabla}\mathbf{J}(n) = -2\mathbf{u}(n)d^*(n) + 2\mathbf{u}(n)\mathbf{u}^H(n)\hat{\mathbf{w}}(n) \tag{24}$$

where ^ indicates an estimate. Using this gradient estimate in the steepest decent algorithm described in Eq. (22) rises a new recursive relation for updating the filter coefficients:

$$\hat{\mathbf{w}}(n+1) = \hat{\mathbf{w}}(n) + \mu\mathbf{u}(n)\left[d^*(n) - \mathbf{u}^H(n)\hat{\mathbf{w}}(n)\right] = \hat{\mathbf{w}}(n) + \mu\mathbf{u}(n)e^*(n). \tag{25}$$

The LMS filter algorithm involves two processes, namely a filtering process that computes the filter output and an adaptive process that automatically adjusts the tap weights. The last one is called the adaptive weight-control mechanism. Figure 9 shows a schematic solution to the filtering problem making use of the complex LMS algorithm [6].

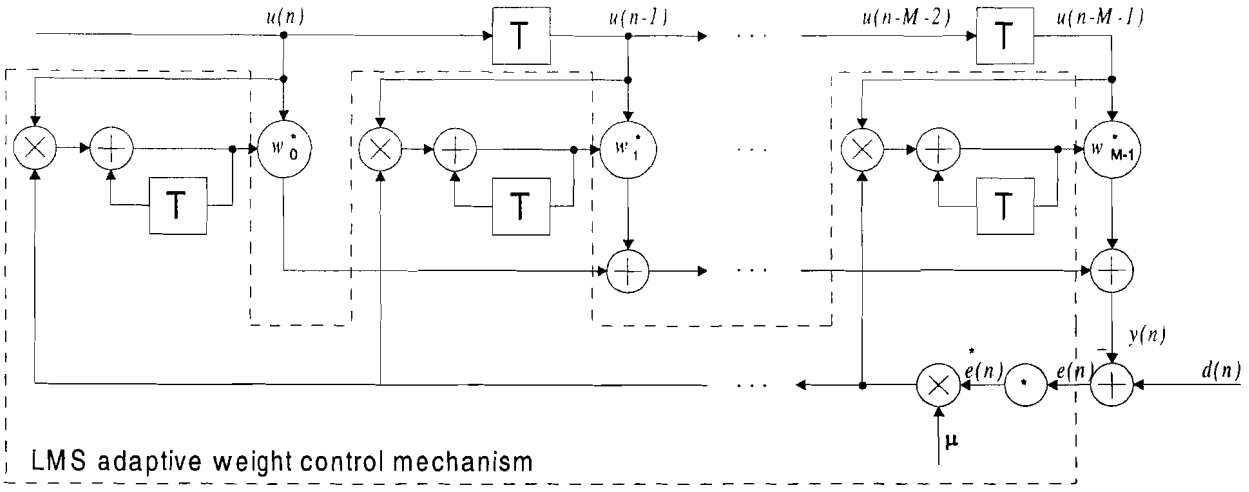

Figure 9: Schematic solution to the filtering problem using the complex LMS algorithm.

The convergence of the mean squared error J or the performance of the LMS algorithm depends on three factors. That are the step-size parameter μ, the tap input power defined as

$$E\left[|u(n-k)|^2\right] \text{ for the } k^{\text{th}} \text{ tap} \tag{26}$$

and the minimum mean squared error J_{min}. To assure convergence of the filter taps the step-size parameter is restricted to a certain range, from [6] it is shown to be

$$0 < \mu < \frac{2}{tr[\mathbf{R}]} = \frac{2}{\sum_{k=0}^{M-1} E\left[|u(n-k)|^2\right]} \tag{27}$$

where $tr[\mathbf{R}]$ stands for the trace of the matrix $\mathbf{R}$. The mean squared error J can be written as $J = J_{min} + J_{ex}$, where the excess mean squared error J_{ex} of the LMS algorithm [6] is approximated by

$$J_{ex} \approx \frac{\mu}{2} J_{\min} tr[\mathbf{R}] = \frac{\mu}{2} J_{\min} \sum_{k=0}^{M-1} E\left[|u(n-k)|^2\right]. \tag{28}$$

The rate of convergence of the mean squared error J of the LMS algorithm can be approximated by a single exponential. The number of iteration needed for the mean squared error to decrease a factor of 1/e is called the adaptation time and from [6] it shown to be

$$\tau \approx \frac{1}{2\mu\lambda_{av}} = \frac{M}{2\mu \sum_{k=0}^{M-1} E\left[|u(n-k)|^2\right]} \tag{29}$$

where μ is the step-size parameter and λ_{av} is the average of the eigenvalues of the correlation matrix **R.**

4. Cross Polarization Interference Canceller

The capacity of radio systems can be doubled when operating in co-channel mode. This technique enables the transmission of two separate channels on the same carrier frequency, using the horizontal and the vertical polarization of the antenna. The transmission in orthogonal polarizations works well as long as the discrimination between the two polarization directions is sufficiently high. This demands operation of the radio under near-ideal propagation conditions. However, Cross-Polarization Interference (XPI) is caused due to various phenomena like rainfall, multipath propagation and equipment imperfections. To ensure operation it is necessary to introduce techniques that increase the Cross-Polarization Discrimination (XPD), especially when high-level modulation schemes are in use. This is accomplished with an adaptive filter that is able to take into account the time-varying nature of the involved phenomena. Such a structure is called Cross Polarization Interference Canceller (XPIC).

Usually data is transmitted on either vertical or horizontal polarization, and new channels are reserved when more capacity is needed. These channels are normally located directly next to the old ones. To minimize the interference between two channels, data in the adjacent channel is transmitted on the opposite polarization. A system that operates like this is called an Alternating Pattern (AP) system. However instead of reserving another channel data can also be transmitted into the same channel via the above-discussed manner. Even more capacity can be allocated if the channel next to the old one is used in the same way. Such a system is called a Co-Channel (CC) system. In Figure 10 the channel allocation for an alternating pattern and for a co-channel system are given. As pointed out earlier, co-channel systems need an XPIC to decrease the XPI. An additional consequence of co-channel operation is that co-channel systems need to have better confined spectra with respect to alternating pattern systems, due to the fact that the adjacent channels transmit on the same polarization planes [7]. This will result in stricter filter conditions for the co-channel case.

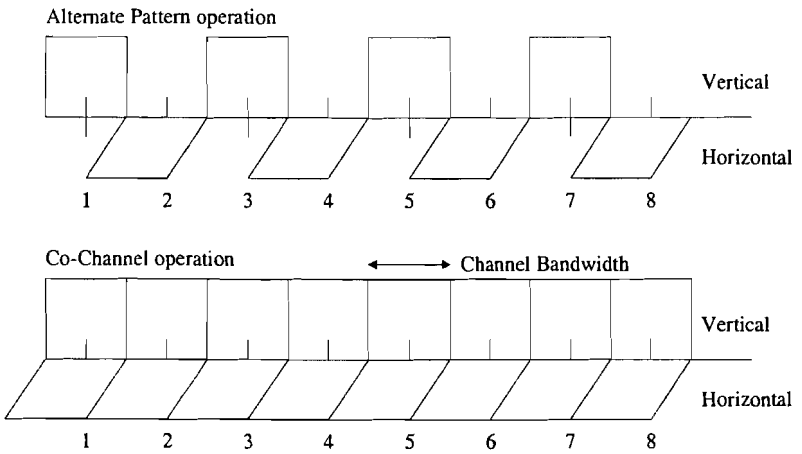

Figure 10: Alternating Pattern and Co-Channel operation

4.1 Definitions

The XPI and the XPD are two important parameters related to the XPIC, their definitions are given by:

$$XPI = 20\log\frac{|E_{HH}|}{|E_{VH}|} \quad [\text{dB}] \tag{30}$$

Where E_{HH} and E_{VH} are vectors of the electromagnetic waves depicted in Figure 11.

$$XPD = 20\log\frac{|E_{HH}|}{|E_{HV}|} \quad [\text{dB}] \tag{31}$$

Where E_{HH} and E_{HV} are vectors of the electromagnetic waves depicted in Figure 11.

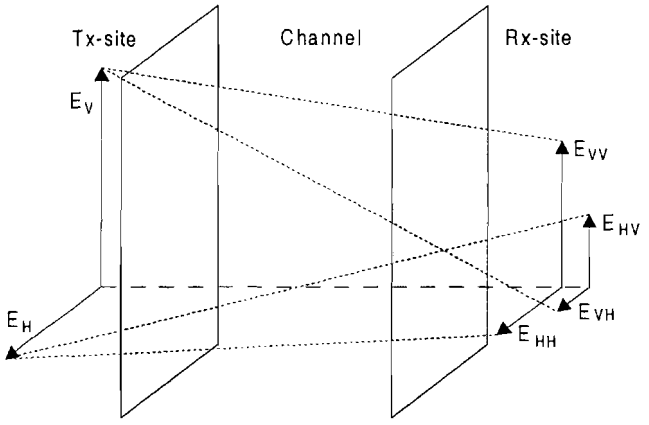

Figure 11: Dual polarized system suffering form XPI

Propagation measurements normally give the XPD rather than XPI, but in most cases they are the same [1]. In that case the XPI and the XPD are denoted by

$$XPD = XPI = 10\log\frac{1-\gamma}{\gamma} \quad [\text{dB}] \tag{32}$$

with $\frac{1-\gamma}{\gamma} = \frac{|E_{HH}|^2}{|E_{VH}|^2} = \frac{|E_{HH}|^2}{|E_{HV}|^2}$. The difference in XPD using an XPIC and not using an XPIC is called the XPIC's Improvement Factor (XIF).

4.2 Functionality of the XPIC

The global structure of a dual-polarized radio is depicted in Figure 1. The transmitter and receiver chains are similar to those treated in Chapter 2. The only differences are extra XPIC paths in both receivers. The adaptive structure of the XPIC is built out of a filter bank and an adaptive weight control mechanism, similar to the ATE. The XPIC is a DA module, estimating the unwanted XPI on every pilot symbol using the LMS method

described in Chapter 3. It correlates the differently polarized signals in the receiver. An essential detail then is the uniqueness of horizontal and vertical sources. Although the sources may be identical when instead of a QAM scheme a TCM scheme is used. A prerequisite then is the use of different scramblers for each polarization [8].

Furthermore from the literature [9] it is shown that when the filter lengths of the XPIC and ATE are equal, the XPIC can be placed preceding the ATE, can be placed parallel to the ATE or the ATE can be placed preceding the XPIC. When the filters have different spans it is a disadvantage to place the longer filter in front of the shorter one, since it can cause far echoes due to their individual tap weighting [9]. The shorter filter is than not able to exercise control over the extra taps of the longer filter. Because of a less complex circuitry the parallel variant is chosen.

To get more insight in the XPIC and for the sake of simplicity it is useful to derive a simplified model of the dual-polarized radio structure. A radio model at baseband is considered, this means that all blocks after the Tx pulse shaping filter and before the Rx pulse shaping filter are left out (upconverters, filters, etc.). Upsamlers and downsamplers are included in the model to be able to vary the sampling rates at different points. Figure 12 depicts the simplified radio model and it forms the basis for the simulations in the next chapter.

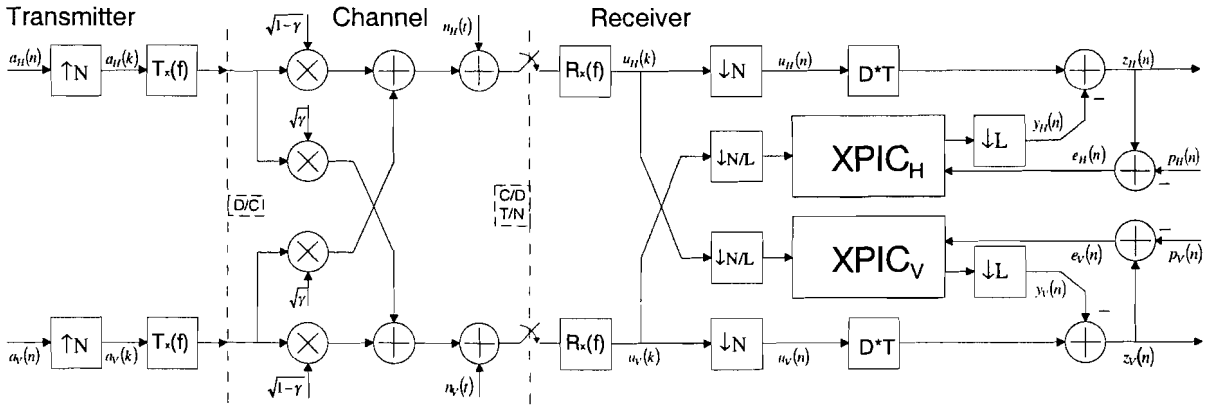

Figure 12: Simplified dual-polarized radio model

Next the horizontal polarization is referred to as H and the vertical polarization as V. The complex data streams in the transmitters are denoted by $a_H(n)$ and $a_V(n)$. They are assumed to be zero mean in such a way that

$$E[a_H(n)a_H^*(m)] = E[a_V(n)a_V^*(m)] = \begin{cases} 0 & n \neq m \\ E[|a_H(n)|^2] = \sigma_a^2 & n = m \end{cases}. \quad (33)$$

Upsampling by a factor N results in upsampled complex data streams

$$a_H(k) = \sum_{n=-\infty}^{\infty} a_H(n)\delta(k - nN) \quad (34)$$

$$a_V(k) = \sum_{n=-\infty}^{\infty} a_V(n)\delta(k-nN).$$

The overall transfer function of the pulse shaping filters and the channel $\mathbf{Q}\left(e^{j\Omega NT'}\right)$ can be denoted in matrix form as

$$\mathbf{Q}\left(e^{j\Omega NT'}\right) = T_x\left(e^{j\Omega NT'}\right)\mathbf{C}(\Omega)R_x\left(e^{j\Omega NT'}\right) = N\left(e^{j\Omega NT'}\right)\begin{pmatrix} C_{HH}(\Omega) & C_{VH}(\Omega) \\ C_{HV}(\Omega) & C_{VV}(\Omega) \end{pmatrix} \quad (35)$$

where $T_x\left(e^{j\Omega NT'}\right)$ and $R_x\left(e^{j\Omega NT'}\right)$ are the time-discrete root raised cosine frequency responses $\sqrt{N\left(e^{j\Omega NT'}\right)}$ of the pulse shaping filter, with $T' = T/N$. The matrix $\mathbf{C}(\Omega)$ represents the dually polarized propagation channel, in which $C_{HH}(\Omega)$ and $C_{VV}(\Omega)$ are the co-polar responses and $C_{VH}(\Omega)$ and $C_{HV}(\Omega)$ are the unwanted cross-polar responses. The signal after the receiver's pulse shaping filter can be written as

$$\begin{aligned} u_H(k) &= \sum_n \left[a_H(n)q_{HH}(k-nN) + a_V(n)q_{VH}(k-nN)\right] + v_H(k) \\ u_V(k) &= \sum_n \left[a_V(n)q_{VV}(k-nN) + a_H(n)q_{HV}(k-nN)\right] + v_V(k) \end{aligned} \quad (36)$$

where $q_{ij}(k)$ is the inverse time-discrete Fourier transform of the i^{th}/j^{th} element of the overall transfer function $\mathbf{Q}\left(e^{j\Omega NT'}\right)$. $v_H(k)$ and $v_V(k)$ are two independent noise processes, generated by filtering and sampling the two independent noise processes $n_H(t)$ and $n_V(t)$ at the receiver [3]. When the channel is assumed to be flat and if only the depolarization effects are considered, Eq. (36) can be rewritten after downsampling with a factor N as

$$\begin{aligned} u_H(kN) = u_H(n) &= \sqrt{1-\gamma}\,a_H(n) + \sqrt{\gamma}\,a_V(n) + v_H(n) \\ u_V(kN) = u_V(n) &= \sqrt{1-\gamma}\,a_V(n) + \sqrt{\gamma}\,a_H(n) + v_V(n). \end{aligned} \quad (37)$$

The amount of XPI in the horizontal and vertical polarization is assumed to be equal, where the parameter γ is a measure for the XPD.

If the input signals of the XPICs are also downsampled with a factor N (L=1), then the horizontal baseband signal in Eq. (37) serves as input for the XPIC in the vertical radio link and the vertical baseband signal in Eq. (37) serves as input for the XPIC in the horizontal radio link. For now the AGCs and PEs are left out. The ATEs are redundant because the channel does not suffer from any multipath fading at this point. Both ATEs are replaced by a delay of D symbols, enabling the center tap of the XPIC's filter bank to be configured.

The outputs of the XPICs must compensate the unwanted XPI signals. When an XPIC filter length of M is chosen, the outputs can be written in a similar form as Eq. (15)

$$y_H(n) = \mathbf{w}_{VH}^H(n)\mathbf{u}_V(n)$$

$$y_V(n) = \mathbf{w}_{HV}^H(n)\mathbf{u}_H(n). \tag{38}$$

In which $\mathbf{w}_{VH}(n)$ and $\mathbf{w}_{HV}(n)$ are the M-by-1 instantaneous tap-weight vectors of respectively the horizontal XPIC and the vertical XPIC at time n defined by Eq. (21), and $\mathbf{u}_V(n)$ and $\mathbf{u}_H(n)$ are the M-by-1 tap-input vectors of respectively the horizontal XPIC and the vertical XPIC at time n defined by Eq. (10). These outputs are then subtracted from the delayed baseband signals to form the corrected signals

$$\begin{aligned} z_H(n) &= u_H(n-D) - \mathbf{w}_{VH}^H(n)\mathbf{u}_V(n) \\ z_V(n) &= u_V(n-D) - \mathbf{w}_{HV}^H(n)\mathbf{u}_H(n). \end{aligned} \tag{39}$$

Subtracting the regenerated pilot signals from the corrected signals gives the estimation error in the horizontal and vertical branches:

$$\begin{aligned} e_H(n) &= z_H(n) - p_H(n) = z_H(n) - a_H(n-D) \\ e_V(n) &= z_V(n) - p_V(n) = z_V(n) - a_V(n-D). \end{aligned} \tag{40}$$

They can be expressed in a similar form as treated in Chapter 3, that is

$$\begin{aligned} e_H(n) &= u_H(n-D) - a_H(n-D) - y_H(n) = d_H(n) - y_H(n) \\ e_V(n) &= u_V(n-D) - a_V(n-D) - y_V(n) = d_V(n) - y_V(n) \end{aligned} \tag{41}$$

where $d_H(n)$ and $d_V(n)$ represent the desired responses for the XPICs.

4.3 XPIC Filter Structure

The algorithm behind the adaptive XPIC structure is the complex LMS algorithm. However the realization of this algorithm is a bit different than presented in Chapter 3. Instead of having single complex signals, the signals consist of two parts: a real part named the in-phase component and an imaginary part named quadrature component. This leads to the following notation for the data and tap-weights for the horizontal receiver branch

Tap-input vector: $\mathbf{u}_V(n) = \mathbf{u}_{V,I}(n) + j\mathbf{u}_{V,Q}(n)$ (42)

Regenerated pilots : $p_H(n) = p_{H,I}(n) + jp_{H,Q}(n)$ (43)

Tap-weight vector: $\hat{\mathbf{w}}_{VH}(n) = \hat{\mathbf{w}}_{VH,I}(n) + j\hat{\mathbf{w}}_{VH,Q}(n)$ (44)

Transversal filter output: $y_H(n) = y_{H,I}(n) + jy_{H,Q}(n)$ (45)

Corrected signal: $z_H(n) = z_{H,I}(n) + jz_{H,Q}(n)$ (46)

Estimation error: $e_H(n) = e_{H,I}(n) + je_{H,Q}(n)$ (47)

where I and Q stand for the in-phase and quadrature component respectively. Using these definitions in the expressions of: the filter output Eq. (38), the estimation error Eq. (2), the update relation Eq. (25) and the corrected signal Eq. (39) gives:

Filter output (in-phase):
$$y_{H,I}(n) = \hat{\mathbf{w}}_{VH,I}^{T}(n)\mathbf{u}_{V,I}(n) - \hat{\mathbf{w}}_{VH,Q}^{T}(n)\mathbf{u}_{V,Q}(n) \quad (48)$$

Filter output (quadrature):
$$y_{H,Q}(n) = \hat{\mathbf{w}}_{VH,I}^{T}(n)\mathbf{u}_{V,Q}(n) + \hat{\mathbf{w}}_{Q}^{T}(n)\mathbf{u}_{V,I}(n) \quad (49)$$

Corrected signal (in-phase):
$$z_{H,I}(n) = u_{H,I}(n-D) - y_{H,I}(n) \quad (50)$$

Corrected signal (quadrature):
$$z_{H,Q}(n) = u_{H,Q}(n-D) - y_{H,Q}(n) \quad (51)$$

Estimation error (in-phase):
$$e_{H,I}(n) = z_{H,I}(n) - p_{H,I}(n) \quad (52)$$

Estimation error (quadrature):
$$e_{H,Q}(n) = z_{H,Q}(n) - p_{H,Q}(n) \quad (53)$$

Update relation (in-phase):
$$\hat{\mathbf{w}}_{VH,I}(n+1) = \hat{\mathbf{w}}_{VH,I}(n) + \mu\left[e_{H,I}(n)\mathbf{u}_{V,I}(n) - e_{H,Q}(n)\mathbf{u}_{V,Q}(n)\right] \quad (54)$$

Update relation (quadrature):
$$\hat{\mathbf{w}}_{VH,Q}(n+1) = \hat{\mathbf{w}}_{VH,Q}(n) + \mu\left[e_{H,I}(n)\mathbf{u}_{V,Q}(n) + e_{H,Q}(n)\mathbf{u}_{V,I}(n)\right] \quad (55)$$

Of course the same analysis can be applied for the vertical receiver branch. The structure resulting from these equations is called the canonical model in literature [6]. Figure 13 represents this model and Figure 14 shows the update algorithm in detail. The thick lines in the figures are vectors or multi real valued signals and the thin lines are simple real valued signals. Form the figures it can be seen that this model consists of four real LMS algorithms with cross coupling between them, see also the resemblance between the update part and the adaptive weight control mechanism in Figure 9. The XPIC structure used in the simulation environment in the next Chapter is similar to the canonical model.

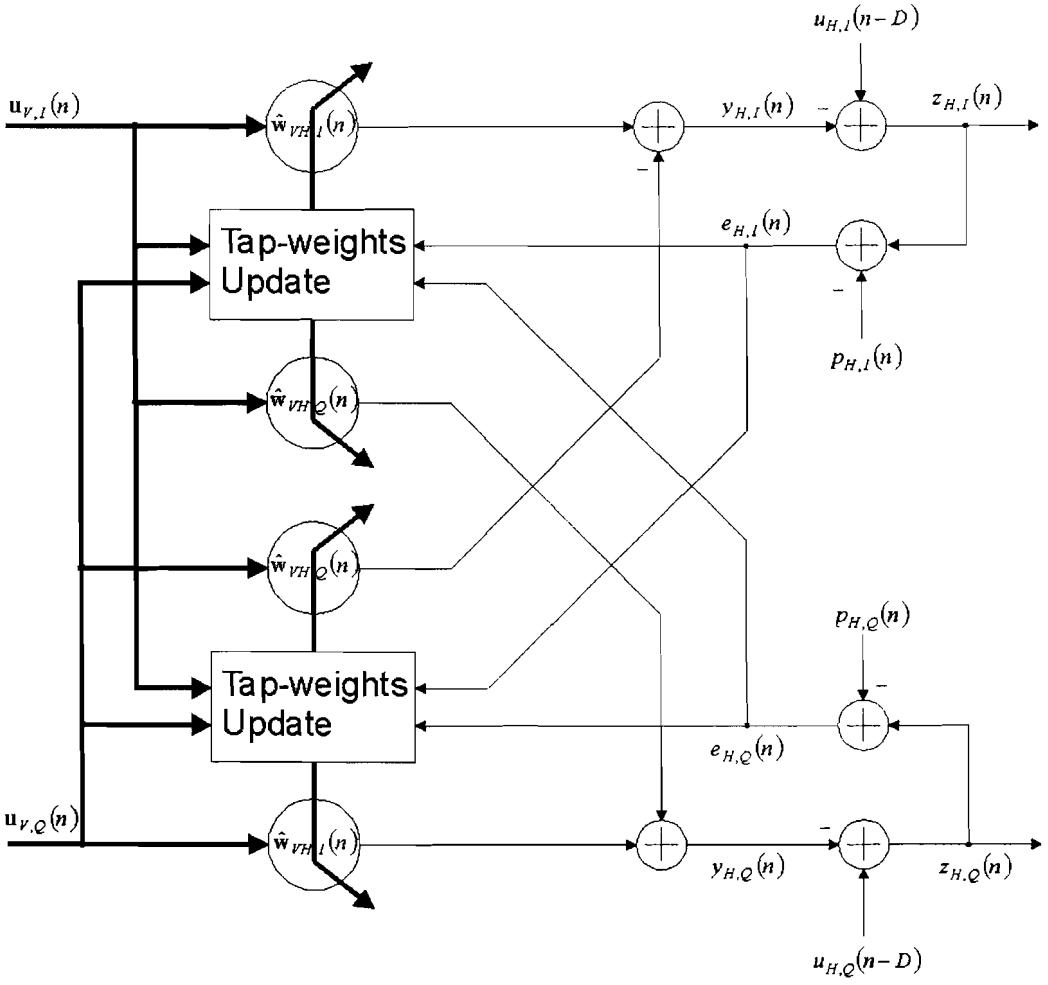

Figure 13: Canonical model for the filtering problem.

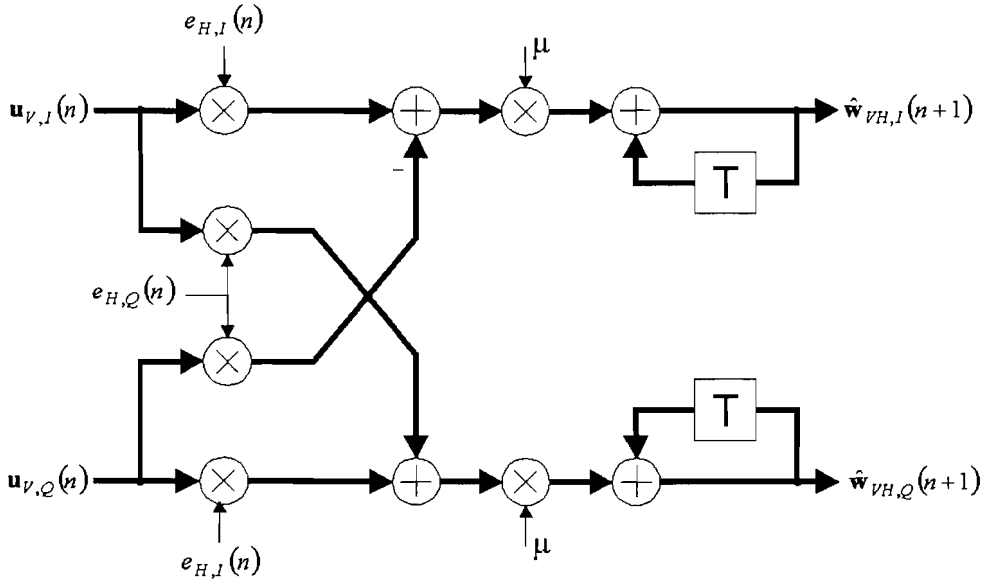

Figure 14: Tap-weights update part

5. Simulations

In the following Chapter a Synopsis tool named CoCentric System Studio is used for simulation purposes. CoCentric System Studio is a system-level design suite consisting of tools, methodologies, and libraries that enables the design and simulation of systems-on-a-chip. System Studio provides several types of model implementations. The Data Flow Graph (DFG) is most suitable for creating the XPIC environment. A dataflow model is a model in which the instances it contains communicate by means of FIFO (first in, first out) queues of data travelling on the nets. The model schematic is graphically represented as a block diagram in which the modules can be ordered hierarchically. System Studio already contains a wide selection of standard modules that can be instantiated into the design. This prevents writing all building blocks manually and therefore allows fast operation. The XPIC's simulation environment represents a dual polarized baseband radio that is built out of mainly standard modules.

The simulations carried out can be distinguished into two categories. The first category holds simulations that focus primarily on the XPIC and are called XPIC specific simulations. The second category holds simulations that focus on the whole system and are called system performance simulations. Furthermore all simulations are devoted to the horizontal receiver chain only, since the same results can be obtained for the vertical receiver chain.

The XPIC specific simulations highlight four specific factors that influence the XPIC's performance. First of all the position of the decision aided AGC in the receiver branch is considered. Secondly time delays between the signal in the horizontal receiver branch and the vertical receiver branch are considered. Thirdly frequency offsets at different locations in the radio are considered and finally the influence of phase shifts in the channel branches on the performance of the XPIC is investigated.

The system performance simulations compare the performance of the system with and without XPIC in two different channel situations. The first channel does not suffer from multi-path fading and the second one does.

5.1 XPIC Specific Simulations

The measurements in this section are primarily related to the performance of the XPIC under different equipment assumptions and channel conditions.

5.1.1 System Considerations

The transmitter side of the simulation environment is depicted in Figure 15, it consists of two transmitters with independent bit sources. The bits are translated into symbols by a 16 QAM encoder and are then multiplexed –a pilot spacing of five symbols is adopted– with QPSK encoded pilot symbols. The QAM and QPSK encoded symbols are normalized to have unity power. Furthermore the pilots in horizontal and vertical transmitter are synchronized. Next the multiplexed signal is upsampled by a factor N and

modified by a root-raised cosine pulse shaping filter before leaving the transmitter. The root-raised cosine filter has a rolloff factor of 0.34 and a cutoff frequency that is normalized to the sample frequency of 0.5/N. Additionally the transmitter feeds the bare pilot sequences as a reference to the receiver. Consequently there will be no need for pilot detection in the receiver.

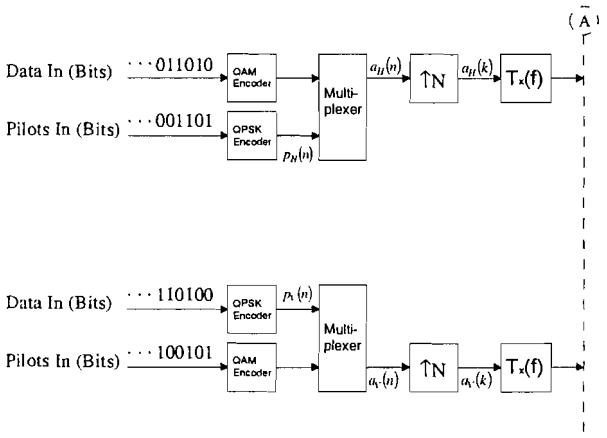

Figure 15: Transmitter structure

An XPI channel as mentioned in the previous Chapter is used, multipath fading is not accounted for. The channel model is depicted in Figure 16.

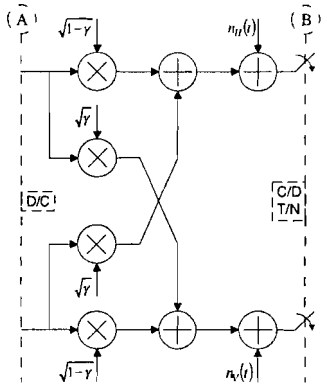

Figure 16: Channel model

The receiver side of the simulation environment is depicted in Figure 17. It consists of two receivers with equal functionality. The incoming signal is shaped by the same root-raised cosine filter as in the transmitter and is downsampled by a factor of N in the equalizer's path and by a factor of N/L in the XPIC's path. This signal is the XPIC's input for the other polarized radio. The XPIC has 17 taps, in line with the number of taps of the designed ATE in the existing Nokia receiver. The step-size parameter is set at 0.001, providing a fast rate of convergence and a negligible excess mean squared error. The ATE is replaced with a delay of D symbols that demarcates the center tap of the XPIC. The compensation signal output by the XPIC is downsampled with a factor L to achieve equal sampling rates at the adder. The sample factor N in the transmitter and

receiver is set to 4 to be able to insert fractional delays of ¼ symbol into the model. In the existing Nokia radio this upsampling is done to simplify the analog filter conditions.

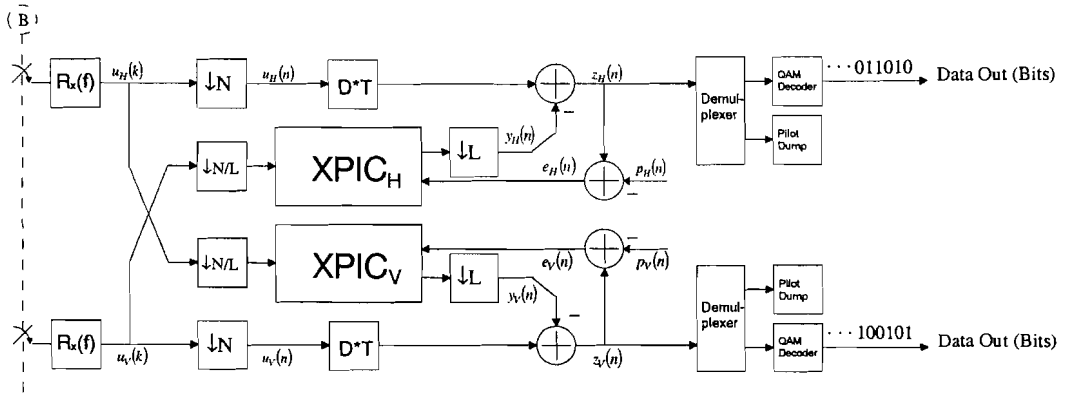

Figure 17: Receiver structure

The performance of the XPIC is monitored by measuring the error signal power of the XPIC, defined as the squared magnitude of the error samples. It is averaged over 100 samples to make it smoother. Comparing it with the actual XPI signal power gives information about the operational status of the XPIC. Additionally 1000 samples of the scatter or constellation diagram of the corrected signal are measured when the process has reached steady state. Before convergence of the XPIC the constellation diagram represents a 16 QAM payload signal superimposed with a 16 QAM interference signal plus a QPSK pilot signal superimposed with a QPSK interference signal. After convergence of the XPIC tap weights it should represent constellation points of a clear 16 QAM plus a QPSK signal without superposition of interference. The interfered and ideal constellation diagram are depicted in Figure 18 for an XPD parameter γ=0.05.

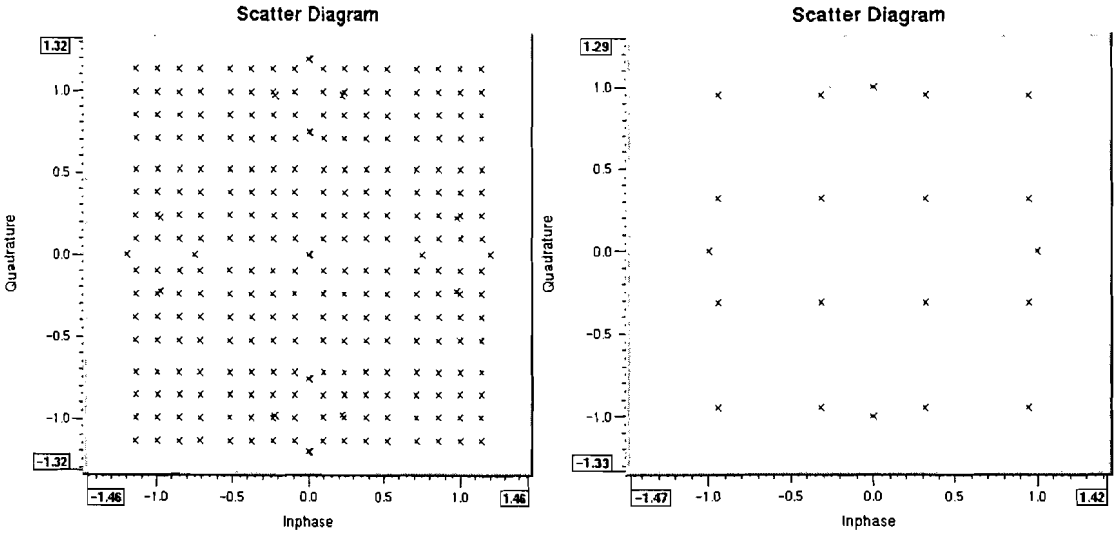

Figure 18: Worst case and ideal constellation diagram

5.1.2 Positioning the Decision Aided AGC

5.1.2.1 Problem Sketch

Parts of the receiver and especially the ATE and the XPIC are decision aided blocks. This means that their operation depends upon the regenerated pilots. This poses high demands on the pilot detection. Loss of pilot synchronization is not tolerated. Varying delays in the receiver are therefore not allowed. Hence it is highly preferable to have an equalizer filter structure with a fixed center tap. Fixing the center tap means setting one tap weight to a fixed value, normally one. The result is that this kind of equalizer is not able to compensate the small remaining attenuation or amplification effects after the NDA AGC. However an important attribute is that the pilots inside the received data stream should have the same magnitude as the reference pilots. Otherwise a gain error will be introduced upon calculating the error signal for the XPIC and ATE. Consequently a DA AGC that is able to correct the gain of the received pilots accompanies the ATE. The AGC compares the magnitude of the received pilots with the magnitude of the reference pilots. After multiplication with a loop constant K the resulting signal is integrated. This integrated signal is subtracted from one, ending up in a gain correction for the received signal. The structure of the AGC is depicted in Figure 19.

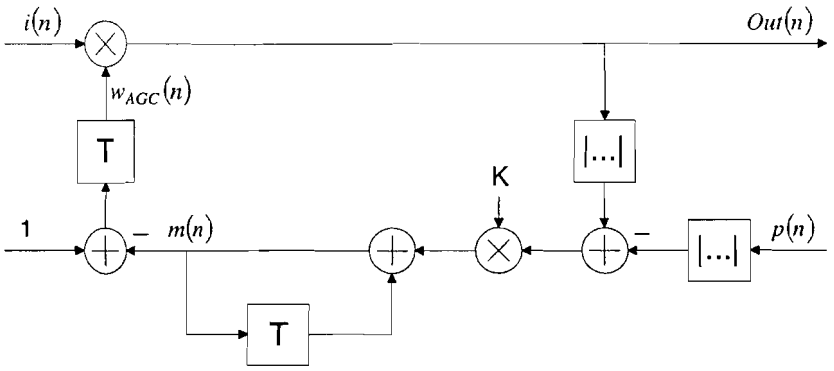

Figure 19: AGC structure

The relation between in- and output is given by

$$Out(n) = i(n)w_{AGC}(n) = i(n)(1 - m(n-1)) = i(n)\left(1 - \left\{K\left(|Out(n-1)| - |p(n-1)|\right) + m(n-2)\right\}\right) \quad (56)$$

where $w_{AGC}(n)$ stands for the real AGC coefficient at time n. In the following simulations the real AGC coefficient is set to its optimum value. This optimum value can easily be computed because the used channel only suffers from a constant attenuation and it does not model any fading conditions. The question that arises now is; is there an optimal position for this AGC?

From a previous study [2] it is known that the XPIC is unable to converge to its optimal coefficients, due to the fact that the input of the XPIC is contaminated with interference from the other branch. However this study only deals with the operation of the XPIC on itself, based on one simple channel assumption.

5.1.2.2 Simulation Outline

Four different receiver structures are considered under a noiseless channel ($n(t)$=0) and an XPD of γ=0.05:

1. *A receiver structure without AGC.*
2. *A receiver structure with AGC positioned in front of the XPIC, depicted in Figure 20 by* ①.
3. *A receiver structure with AGC positioned parallel to the XPIC, depicted in Figure 20 by* ②.
4. *A receiver structure with AGC positioned behind the XPIC, depicted in Figure 20 by* ③.

In Figure 20 the ATE is represented by the delay D and the AGCs are represented by the parameters $w_{AGC,H}$ and $w_{AGC,V}$. The delay D is set to D=9 and the downsample factor L is set to L=1.

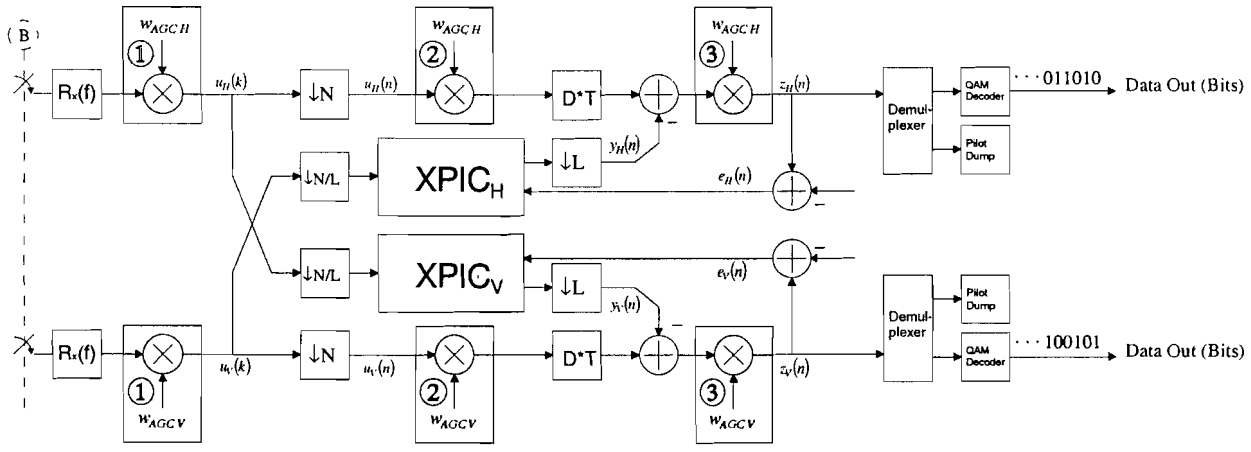

Figure 20: Different positions for the AGC in the receiver structure

5.1.2.3 Simulation Results

The simulation results of the first situation are depicted in Figure 21. The dotted error signal power curve represents the error measured before the XPIC and the solid error signal power curve represents the error measured after the XPIC. The error signal power decreases to the steady state value of approximately 0.0056. This gain error is caused by the fact that the reference pilots and the pilots into the data stream do not have the same magnitude.

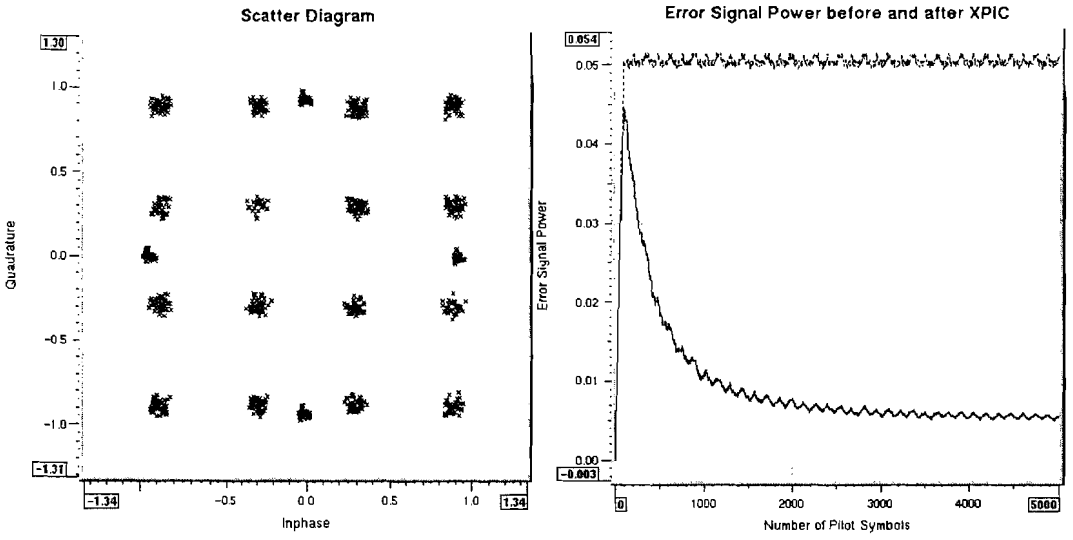

Figure 21: Simulation results for situation one

Theoretical analysis results in the same steady state gain error. Calculating the variance of desired XPIC's response (Eq. (41)) leads to

$$\sigma_d^2 = 2\sigma_a^2\left(1-\sqrt{1-\gamma}\right)+\sigma_v^2 \tag{57}$$

where σ_v^2 denotes the variance of the white noise process $v_H(n)$. Computing the 17-by-17 autocorrelation matrix and the 17-by-1 cross-correlation vector gives

$$\mathbf{R} = E\left[\mathbf{u}_V(n)\mathbf{u}_V^H(n)\right] = \sigma_a^2\left(1+\frac{\sigma_v^2}{\sigma_a^2}\right)\mathbf{I} \tag{58}$$

$$\varrho = E\left[\mathbf{u}_V(n)d_H^*(n)\right] = \left[0 \;\cdots\; 0 \;\; \sigma_a^2\sqrt{\gamma}\left(2\sqrt{1-\gamma}-1\right)^2 \;\; 0 \;\cdots\; 0\right]^T \tag{59}$$

where $\mathbf{I}$ stands for the 17-by-17 identity matrix. The absence of noise results in $\sigma_v^2 = 0$ and taking into account that QPSK (amplitude 1) encoded pilots are used results in $\sigma_a^2 = 1$. Now substituting Eq. (57), Eq. (58) and Eq. (59) in Eq. (18) leads to

$$J_{\min} = 2\left(1-\sqrt{1-\gamma}\right)-\gamma\left(2\sqrt{1-\gamma}-1\right)^2. \tag{60}$$

With the XPD parameter γ=0.05 this results in the value 0.0056 for the minimum mean squared error, which is equal to the simulated steady state value of the error signal power.

The simulation results for case two are shown in Figure 22. The error signal power decreases to the steady state value of approximately 0.0026. In this case both AGCs have the same gain $w_{AGC,H} = w_{AGC,V} = 1/\sqrt{1-\gamma}$. The received pilots and the reference pilots are at that point equal in size. Afterwards however the output of the XPIC is added to this

signal. This output signal $y_H(n)$ of the XPIC will contain a small portion of the transmitted horizontal signal, due to the fact that the input signal $\mathbf{u}_V(n)$ to the XPIC contains interference from horizontal path. This interference is now responsible for the introduced gain error.

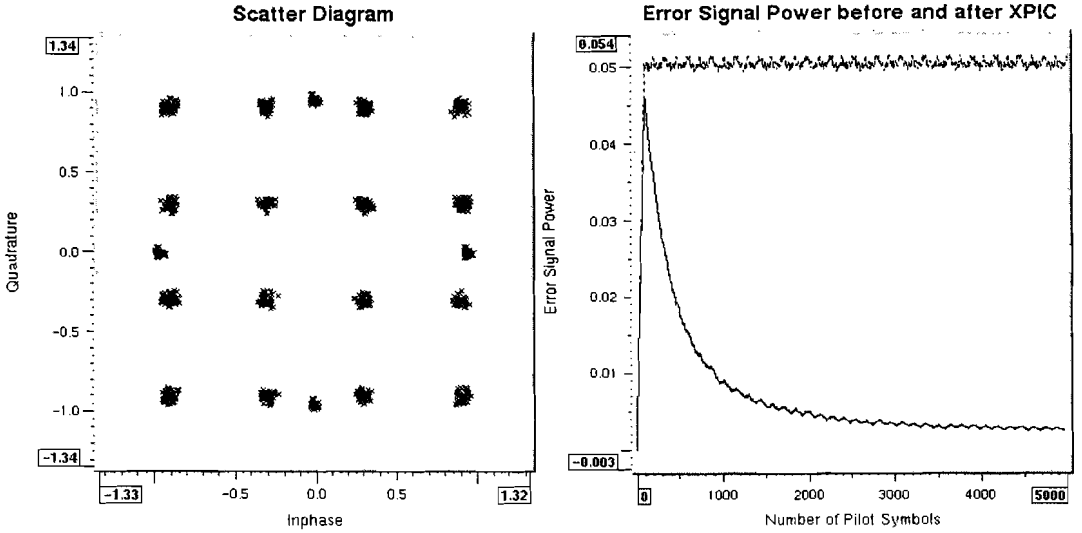

Figure 22: Simulation results for case two

Also in this case the steady state gain error obtained via theoretical analysis matches the simulation. The horizontal and vertical baseband signals are given by

$$u_H(n) = a_H(n) + \frac{\sqrt{\gamma}}{\sqrt{1-\gamma}} a_V(n) + \frac{1}{\sqrt{1-\gamma}} v_H(n)$$
$$u_V(n) = a_V(n) + \frac{\sqrt{\gamma}}{\sqrt{1-\gamma}} a_H(n) + \frac{1}{\sqrt{1-\gamma}} v_V(n). \qquad (61)$$

Computation of the variance of the desired XPIC's response, the autocorrelation matrix and the cross-correlation vector result in

$$\sigma_d^2 = \frac{\gamma}{1-\gamma}\sigma_a^2 + \frac{1}{1-\gamma}\sigma_v^2 \qquad (62)$$

$$\mathbf{R} = E\left[\mathbf{u}_V(n)\mathbf{u}_V^H(n)\right] = \frac{\sigma_a^2}{1-\gamma}\left(1+\frac{\sigma_v^2}{\sigma_a^2}\right)\mathbf{I} \tag{63}$$

$$\varrho = E\left[\mathbf{u}_V(n)d_H^*(n)\right] = \left[0 \;\cdots\; 0 \;\; \sigma_a^2\frac{\sqrt{\gamma}}{\sqrt{1-\gamma}} \;\; 0 \;\cdots\; 0\right]^T. \tag{64}$$

With $\sigma_v^2 = 0$ and $\sigma_a^2 = 1$ this leads to the following minimum mean squared error

$$J_{\min} = \frac{\gamma^2}{1-\gamma}. \tag{65}$$

Substituting the XPD parameter γ value in this equation gives a minimum mean squared error of 0.0026, indeed corresponding to the simulated steady state gain error.

The simulation results for case three are shown in Figure 23. The error signal power decreases again to the steady state value of approximately 0.0026. Also the AGCs take on the same gain as in the previous simulation $w_{AGC,H} = w_{AGC,V} = 1/\sqrt{1-\gamma}$. The pilots in the data stream and the reference pilots are again at that point equal in size, but again when the output signal $y_H(n)$ of the XPIC is added to the baseband signal $u_H(n)$ a gain error will occur.

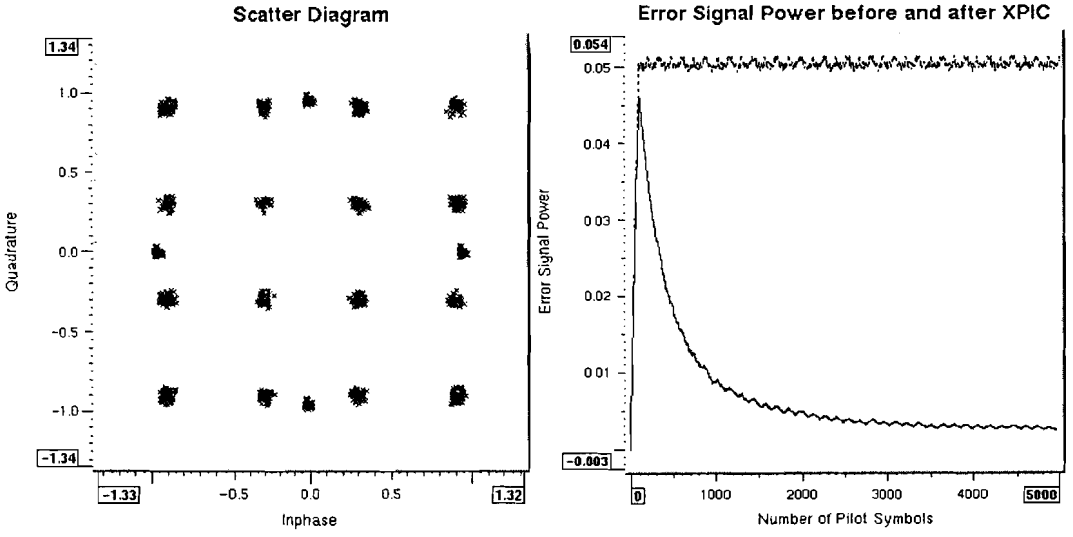

Figure 23: Simulation results for case three

Theoretical analysis shows the same result as in the simulation case. The desired response and its variance in this situation are given by

$$d(n) = \frac{1}{\sqrt{1-\gamma}} u_H(n-D) - a_H(n-D) \tag{66}$$

$$\sigma_d^2 = \frac{\gamma}{1-\gamma}\sigma_a^2 + \frac{1}{1-\gamma}\sigma_v^2 . \tag{67}$$

Computation of the autocorrelation matrix and the cross-correlation vector results in

$$\mathbf{R} = E\left[\mathbf{u}_V(n)\mathbf{u}_V^H(n)\right] = \sigma_a^2\left(1 + \frac{\sigma_v^2}{\sigma_a^2}\right)\mathbf{I} \tag{68}$$

$$\varrho = E\left[\mathbf{u}_V(n)d_H^*(n)\right] = \left[0 \;\cdots\; 0 \;\; \sigma_a^2\sqrt{\gamma} \;\; 0 \;\cdots\; 0\right]^T . \tag{69}$$

Again with $\sigma_v^2 = 0$ and $\sigma_a^2 = 1$ this leads to the following minimum mean squared error

$$J_{\min} = \frac{\gamma^2}{1-\gamma} . \tag{70}$$

Notice that the minimum mean squared error has the same form as in the previous simulation. When the value of the XPD parameter γ is substituted in Eq. (70) this will again lead to a minimum mean squared error of 0.0026. Also in this case the calculated value corresponds to the simulated one.

Simulation results for situation four are depicted in Figure 24. The error signal power decreases to zero, because also the horizontal signal contribution in the XPIC's output is compensated for. The error signal power starts however at a higher level because the AGC is directly set to its optimal value.

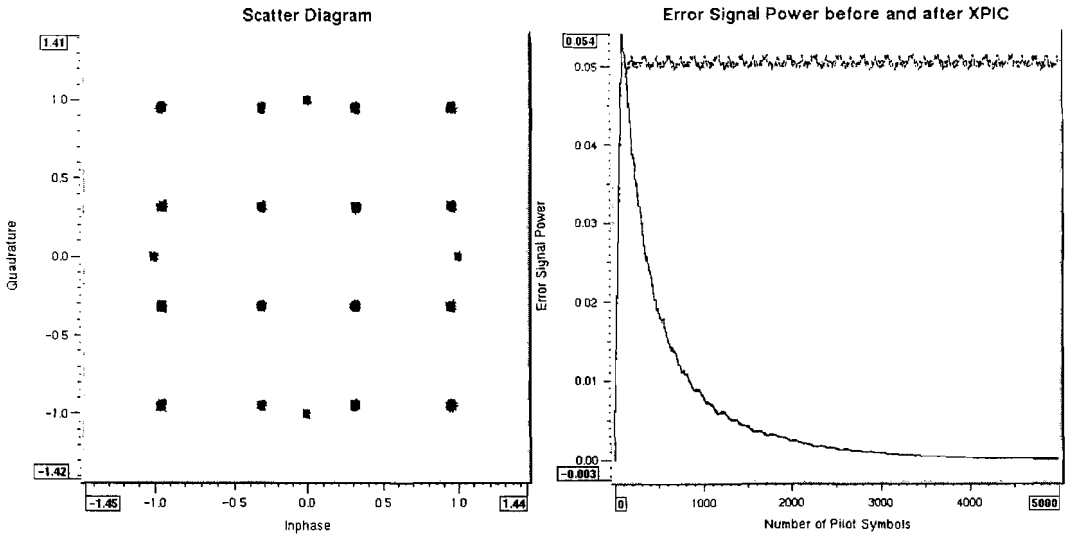

Figure 24: Simulation results for situation three

The value, which the AGC takes on, can be calculated. First the gain parameter $w_{AGC,H}$ is assumed unknown and seen as an extension of the filter structure. The error signal can then be written as

$$\begin{aligned} e_H(n) &= w^*_{AGC,H} u_H(n-D) - w^*_{AGC,H} \mathbf{w}^H_{VH} \mathbf{u}_V(n) - a_H(n-D) \\ e_H(n) &= w^*_{AGC,H} u_H(n-D) - \mathbf{w}^H_{tot} \mathbf{u}_V(n) - a_H(n-D). \end{aligned} \tag{71}$$

The desired response in this case is

$$d(n) = a_H(n-D). \tag{72}$$

Computation of the optimal filter coefficients gives again Eq. (12) with

$$\mathbf{w} = \begin{pmatrix} w_{AGC,H} \\ -\mathbf{w}_{tot} \end{pmatrix}, \quad \mathbf{R} = \begin{pmatrix} r_{HH} & \mathbf{r}^T_{HV} \\ \mathbf{r}_{VH} & \mathbf{R}_{VV} \end{pmatrix}, \quad \varrho = \begin{pmatrix} \rho_H \\ \varrho_V \end{pmatrix} \tag{73}$$

where

$$\begin{aligned} r_{HH} &= E\left[u_H(n-D) u^*_H(n-D)\right] = \sigma_a^2 \left(1 + \frac{\sigma_v^2}{\sigma_a^2}\right) \\ \mathbf{r}_{VH} &= \mathbf{r}^*_{HV} = E\left[\mathbf{u}_V(n) u^*_H(n-D)\right] = \left[0 \ \cdots \ 0 \ \ 2\sigma_a^2 \sqrt{\gamma}\sqrt{1-\gamma} \ \ 0 \ \cdots \ 0\right]^T \\ \mathbf{R}_{VV} &= E\left[\mathbf{u}_V(n) \mathbf{u}^H_V(n)\right] = \sigma_a^2 \left(1 + \frac{\sigma_v^2}{\sigma_a^2}\right) \mathbf{I} \\ \rho_H &= E\left[u_H(n-D) a^*_H(n-D)\right] = \sigma_a^2 \sqrt{1-\gamma} \\ \varrho_V &= E\left[\mathbf{u}_V(n) a^*_H(n-D)\right] = \left[0 \ \cdots \ 0 \ \ \sigma_a^2 \sqrt{\gamma} \ \ 0 \ \cdots \ 0\right]^T. \end{aligned} \tag{74}$$

Finally applying this to Eq. (14) and taking $\sigma_v^2 = 0$ and $\sigma_a^2 = 1$ leads to the optimal AGC gain parameter

$$w_{AGC,H} = \frac{\sqrt{1-\gamma}(1-2\gamma)}{1-4\gamma(1-\gamma)}. \tag{75}$$

For this AGC gain parameter the minimum mean squared error J_{min}=0 and thus corresponds to the simulation.

5.1.2.4 Interpretation of the Simulation Results

A receiver structure without AGC will naturally cause a gain error in the error signal. Therefore an AGC should be implemented in the receiver structure. However when located at the wrong position a small gain error will still remain. This gain error is the outcome of the fact that the AGCs placed in front of the point where the contribution of the XPIC is added are not able to account for this contribution. The best position for the AGC from simulation point of view as well as from theoretical point of view is pointed out to be behind the XPIC.

However, equally good results can be achieved when the error signal for the AGC is derived behind the XPIC, but when the gain correction takes place in front of the XPIC or parallel to the XPIC. Though this will lead to a smaller loop bandwidth of the AGC, decreasing the tracking capability. However this decrease is small only depending on the center tap position of the ATE. Considering this it might be a good idea to place the gain correction in front of the XPIC and ATE, keeping the gain of their input signals at a constant level.

5.1.3 Timing Sensitivity of the XPIC

5.1.3.1 Problem Sketch

The horizontal and vertical receiver links belong to two separate radios. This means that the input signals of the XPICs have to be fed from one radio to the other by means of a cable connection. Such a cable connection will cause an unknown signal delay. Furthermore the two radio paths may differ, which can result in an additional delay. Consequently the received signal and the input of the XPIC are not synchronized. The delay most likely consists of a number of symbol delays plus a fractional delay. The question now is; do these delays have any influence on the XPIC's performance?

Previous work [10] showed that baud spaced XPICs and ATEs need exact synchronization of the time phase between horizontal and vertical path in order to achieve the best cancellation performance. This synchronization is done by means of an Elastic Storage (ES) in front of the XPIC's input. When fractionally spaced XPICs are used there will be no need for clock synchronization [11].

5.1.3.2 Simulation Outline

Two types of XPIC structures are compared under a noiseless channel ($n(t)$=0) and an XPD of γ=0.05. A filter structure with a symbol spaced (T) tapped delay line, depicted in Figure 25 by ① and a filter structure with a fractionally spaced (T/2) tapped delay line, depicted in Figure 25 by ②. The AGC is placed behind the XPIC, because it is known from the former chapter that this is the optimal position. The delay parameter D is set to D=9 for the symbol spaced XPIC and is set to D=4 for the fractionally spaced XPIC. The down-sample factor L is set to L=1 in the case of a symbol spaced XPIC and to L=2 for the case of a fractionally spaced XPIC. Both structures are subjected to several different delay parameters ΔT. The delay parameters investigated are:

1. *ΔT=0 (no delays)*
2. *ΔT=2 (2 symbol delays)*
3. *ΔT=2¼ (2 symbol delays and a fractional delay of a ¼ symbol)*
4. *ΔT=2½ (2 symbol delays and a fractional delay of a ½ symbol)*
5. *ΔT=6 (6 symbol delays)*
6. *ΔT=12 (12 symbol delays)*

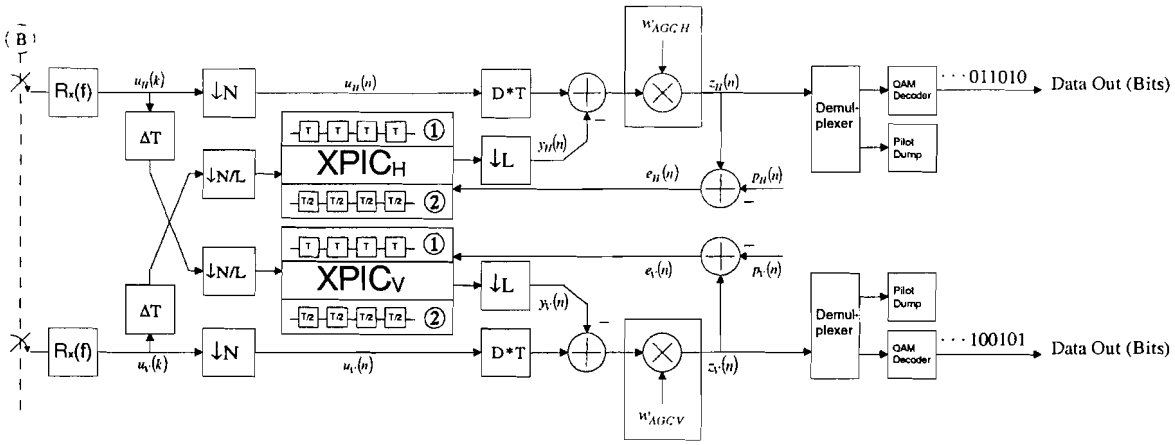

Figure 25: Receiver structure with two types of XPIC structures and including time delays

5.1.3.3 Simulation Results

The first (ΔT=0) and second (ΔT=2) case considered lead to good convergence characteristics for both structure types. The only difference is that the adaptation time constant for the symbol spaced XPIC is $\tau \approx 500$ pilot symbols, whereas the adaptation time constant for the fractionally spaced XPIC is approximately twice as small $\tau \approx 250$ pilot symbols. See Figure 26 for the error signal power curves and Figure 1 and 2 in Appendix A for the accompanying scatter diagrams. The dotted error signal power curve represents again the error measured before the XPIC, the solid black error signal power curve represents the error measured after the symbol spaced XPIC and the solid gray error signal power curve represents the error measured after the fractionally spaced XPIC.

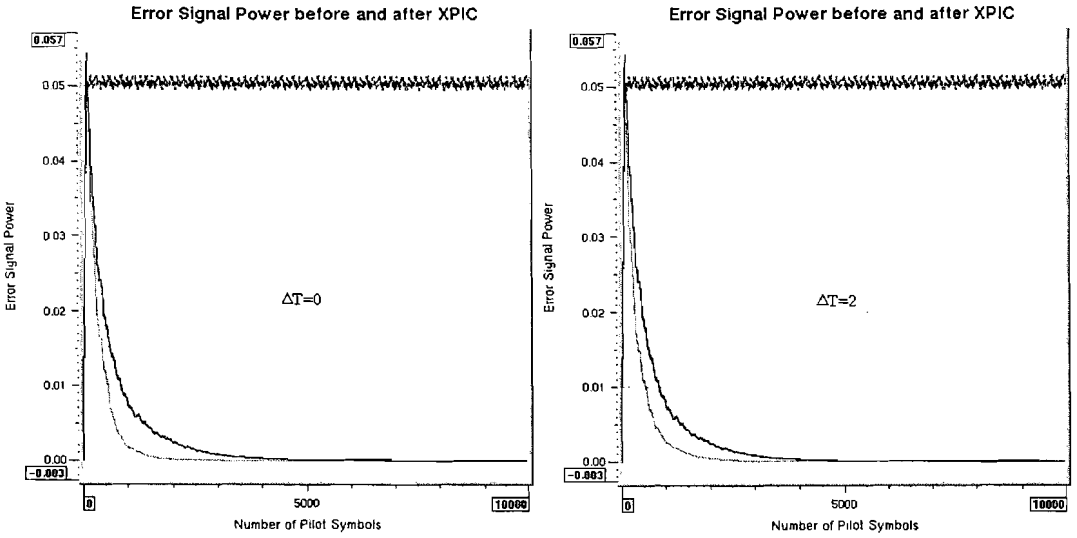

Figure 26: Error signal power curves for the first and second situation

Symbol delays are tolerated because an equalizer structure is used. The number of symbol delays that can be tolerated is in general directly related to the number of filter taps [7].

Situation three (ΔT=2¼) and four (ΔT=2½) show better convergence characteristics for the fractionally spaced XPIC compared to the symbol spaced XPIC. The simulation results are shown in Figure 27 and Figure 3 and 4 in Appendix A for the accompanying scatter diagrams.

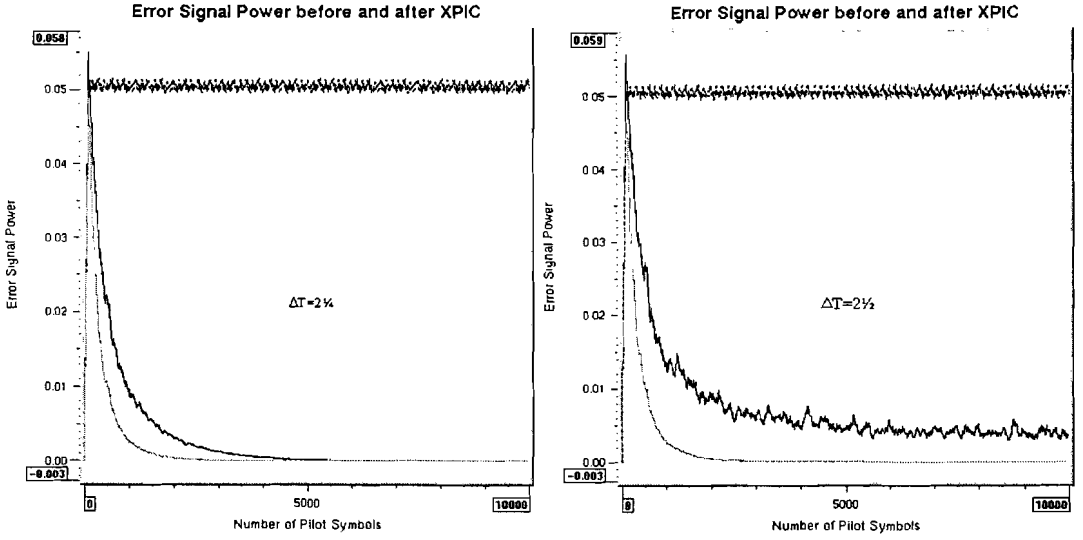

Figure 27: Error signal power curves for case three and four

The fractionally spaced XPIC is able to compensate much more effectively for fractional delay distortion than the symbol spaced XPIC as a matter of fact the fractionally spaced XPIC is almost independent of fractional delay distortions. The symbol spaced XPIC is

still able to compensate for a fractional delay of ¼ with almost no performance loss. Only for the case of a fractional delay of ½ the performance is visibly degraded. The error signal power level decreases, but an error remains.

The same conclusion can also be derived from analytical point of view [12]. To this end consider for the case of a symbol spaced XPIC a ΔT delayed sampled version of the vertically polarized received signal of Eq. (36)

$$u_V(mT-\Delta T)=\sum_n [a_V(n)q_{VV}(mT-nT-\Delta T)+a_H(n)q_{HV}(mT-nT-\Delta T)]+v_V(mT-\Delta T). \quad (76)$$

The noiseless output of the symbol spaced XPIC can be written as

$$y_H(mT-\Delta T)=\sum_n [a_V(n)h_{VV}(mT-nT-\Delta T)+a_H(n)h_{HV}(mT-nT-\Delta T)] \quad (77)$$

where $h_{VV}(mT-nT-\Delta T)$ and $h_{HV}(mT-nT-\Delta T)$ are the filtered signal samples, with their Fourier transform

$$H_T(\Omega)=\sum_l w_{VH,l}e^{-j\Omega lT}\sum_k Q\left(\Omega+k\frac{2\pi}{T}\right)e^{-j\left(\Omega+k\frac{2\pi}{T}\right)\Delta T}=W_{VH,T}(\Omega)Q_T(\Omega) \quad (78)$$

where $w_{VH,l}$ represents the l^{th} tap weight of the XPIC in the horizontal radio link, $Q_T(\Omega)$ is the aliased spectrum of $Q(\Omega)$ and $W_{VH,T}(\Omega)$ is the transfer function of the XPIC. Figure 28 depicts the spectrum of $Q(\Omega)$.

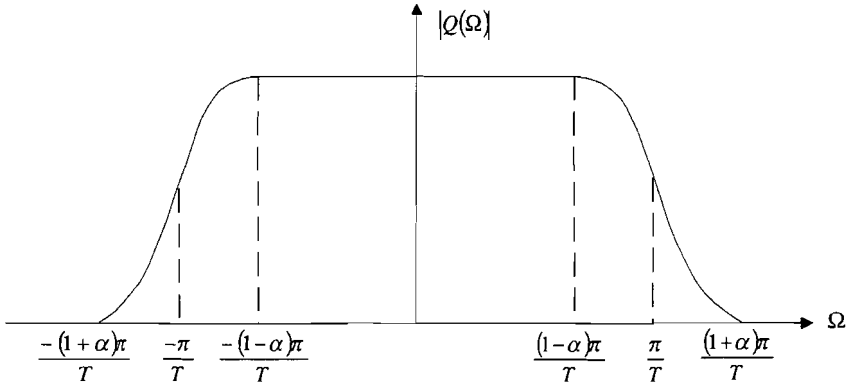

Figure 28: Magnitude spectrum of $Q(\Omega)$

The symbol spaced XPIC can only act on the aliased spectrum of $Q(\Omega)$. Consequently it is not able to exercise independent control over both sides of the rolloff region about $\Omega=\pi/T$. Accordingly it is not able to totally compensate for the fractional part of the delay contribution $e^{-j\Omega\Delta T}$. Therefore suitable sampling instants are of great importance in case of symbol spaced signal processing. To exploit the full potential of a symbol spaced XPIC, synchronized data rates at the input of the XPIC and equalizer are favorable [13].

On the other hand for the case of a fractionally spaced XPIC with spacings of T' the filtered signal spectrum is given by

$$H_{T'}(\Omega)=\sum_{l} w_{VH,l}\, e^{-j\Omega lT'} \sum_{k} Q\left(\Omega + k\frac{2\pi}{T'}\right) e^{-j\left(\Omega+k\frac{2\pi}{T'}\right)\Delta T} = W_{VH,T'}(\Omega) Q_{T'}(\Omega). \qquad (79)$$

When T'<T/(1+α) $Q_{T'}(\Omega)$ is not aliased. Therefore the fractionally spaced XPIC is able to compensate for the delay contribution $e^{-j\Omega\Delta T}$, because of the fact that only the k=0 term is of concern. Then after the filter operation the output is re-sampled at symbol rate.

Situation five (ΔT=6) leads to good performance for the symbol spaced XPIC and to poor performance for the fractionally spaced XPIC. Situation six (ΔT=12) results in poor performance for both kind of XPICs. The results are depicted in Figure 29 and Figure 5 and 6 in Appendix A.

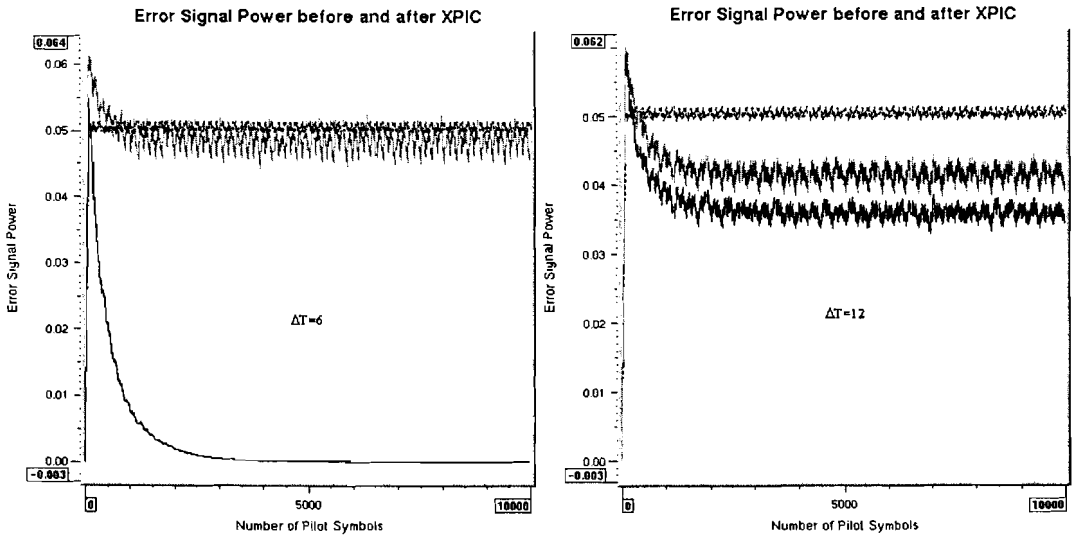

Figure 29: Error signal power curves for case five and six

The delay in situation five and six is too large to be compensated for by the fractionally spaced XPIC. The center tap is located at the tap that corresponds to four delays, so a maximum of four delays can be compensated. The location of the center tap in case of a symbol spaced XPIC corresponds to 9 delays. This is still enough for situation five, but situation six is also in this case out of the filter length's reach.

5.1.3.4 Interpretation of the Simulation Results

A symbol spaced XPIC and a fractionally spaced XPIC are both capable of compensating symbol delays. However when the two structures have the same amount of taps a symbol spaced XPIC is able to handle twice as much symbol delays as a fractionally spaced XPIC. On the other hand a fractionally spaced XPIC is able to handle a fractional delay without performance loss, whereas a symbol spaced XPIC experiences some difficulties.

Though when a symbol spaced XPIC is combined with a Elastic Storage (ES) it will perform equally well, due to the capability of an ES to synchronize data streams [14]. Of course for this purpose an extra module has to be inserted resulting in a more complex schematic. Concluding it can be said that the results are similar to those in the literature.

Finally a remark should be made: It is known that fractionally spaced adaptive filter structures can lead to long term instability, while it is not able to adapt to frequencies outside the rolloff region, due to the fact that the input spectrum is zero for those frequencies. Deeper investigation of the fractionally spaced XPIC should clarify this. Several possible algorithms are presented in the literature to overcome this problem. The simple tap-leakage algorithm [15] and the more complicated algorithm presented by Uyematsu and Sakaniwa [16] are two examples.

5.1.4 Frequency Offsets between the Oscillators of the Radio

5.1.4.1 Problem Sketch

The dual polarized radio link consists of two transmitters and two receivers. Each transmitter consists of a modulator that converts the signal from baseband to IF and an up-converter that raises the frequency to RF. Each receiver consists of a down-converter that lowers the frequency to IF and a demodulator that converts the IF signal into a baseband signal. Every conversion operation at transmitter or receiver involves a local oscillator. Yet it is impossible to design local oscillators that have identical frequency behavior. For this reason frequency offsets occur between the signals in the horizontal and the vertical radio link at transmitter as well as receiver side. These frequency offsets can be eliminated when the local oscillators of the up- and down-converters and the local oscillators of the modulator and demodulator are synchronized. The question that arises; do these frequency offsets degrade the performance of the XPIC?

Previous studies [9], [11], [14] state that a critical issue is system synchronization, suggesting synchronization of the local oscillators at the receiver side. With synchronization of the RF/IF down-converters and IF/BB demodulators the interfering and compensating signal have the same zero-frequency offset. This means that the XPIC does not have to compensate any frequency difference. An advantage of this concept is the independence of the XPIC operation from the lock in state of the carrier recovery loop [9]. The signal exchange takes place at IF, which means that extra demodulators, A/D converters, ND AGCs, etc. are needed. Apart form the signal exchange connection the horizontally and vertically polarized receiver only need one more interconnection, to synchronize the local oscillators of the down-converters.

Other studies [8], [10], [17], [18] suggest synchronization of the modulators and up-converters. This ensures identical center frequencies of both transmitted spectra. Zero-frequency offset between the received horizontally and vertically polarized signal is met by the individual carrier recovery loops in the receiver [8], [18]. The exchange of data can then be done after A/D conversion at baseband, which will save extra A/D converters and demodulators for the XPIC branches.

5.1.4.2 Simulation Outline

Four different situations concerning frequency offsets are considered for a noiseless channel ($n(t)$=0) and an XPD of γ=0.05. The receiver is implemented with a fractionally spaced XPIC resulting in a delay of D=4 and a downsample factor of L=2.

1. *A situation with no frequency offsets in the dual polarized radio is evaluated, which is achieved by sharing or synchronizing the oscillators in the horizontally and vertically polarized radio links. A big disadvantage is the mutual connections between the H and V transmitters and receivers.*
2. *A situation with a frequency offset of 200 kHz at transmitter side is considered. Such a frequency offset is typical for radios that operate in the 18 GHz range according to the ETSI specifications [19]. Thus only the oscillators at the receiver side are shared or synchronized. The frequency offset is indicated by Δf_T and is included in the vertical path, depicted in Figure 30 by ①.*
3. *A situation with a frequency offset of 20 kHz at receiver side is considered. This is a typical value because of the fact that the decision aided modules are becoming active with a residual zero-frequency offset of 20 kHz. Now only the oscillators at the transmitter side are shared or synchronized, resulting in identical carrier frequencies. The frequency offset is indicated by Δf_R and is included in the vertical path, depicted in Figure 30 by ②.*
4. *A situation with a frequency offset of 200 kHz between the transmitters and a frequency offset of 20kHz between the receivers is observed. The frequency offset at the transmitter side is indicated by Δf_T and the frequency offset at the receiver side is indicated by Δf_R, both are included in the vertical path, depicted in Figure 30 by ③.*

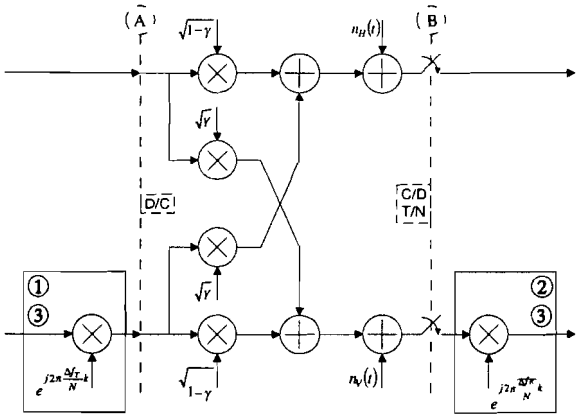

Figure 30: Frequency offsets at transmitter and receiver sides

5.1.4.3 Simulation Results

The first situation naturally leads to good convergence behavior for the XPIC, because it is the same structure as in the previous section and no frequency offset is applied. The results are given in Figure 31.

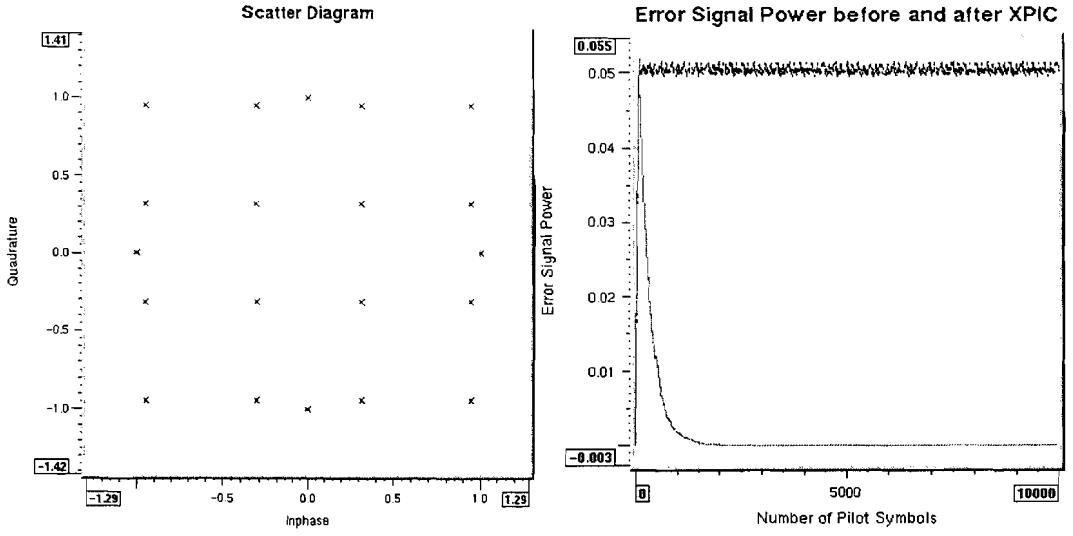

Figure 31: Simulation results for situation one

The results for situation two are depicted in Figure 32. In this case there exists a frequency offset between horizontally and vertically polarized signal in the transmitter. This frequency offset is not visible between the XPIC's error signal and the XPIC's input signal, since they originate from the same polarized radio. A frequency offset only exists between the horizontally polarized signal parts and the vertically polarized signal parts. However all signals will suffer a frequency offset compared to the zero frequency when the demodulator is not able to convert the IF signal to a zero-frequency baseband signal. But this frequency offset is the same for all the signals because the demodulators are shared or synchronized. In time domain a frequency offset is a rotation of the phase. When interference and XPIC input signal have the same rotation velocity this will not have an effect on the performance.

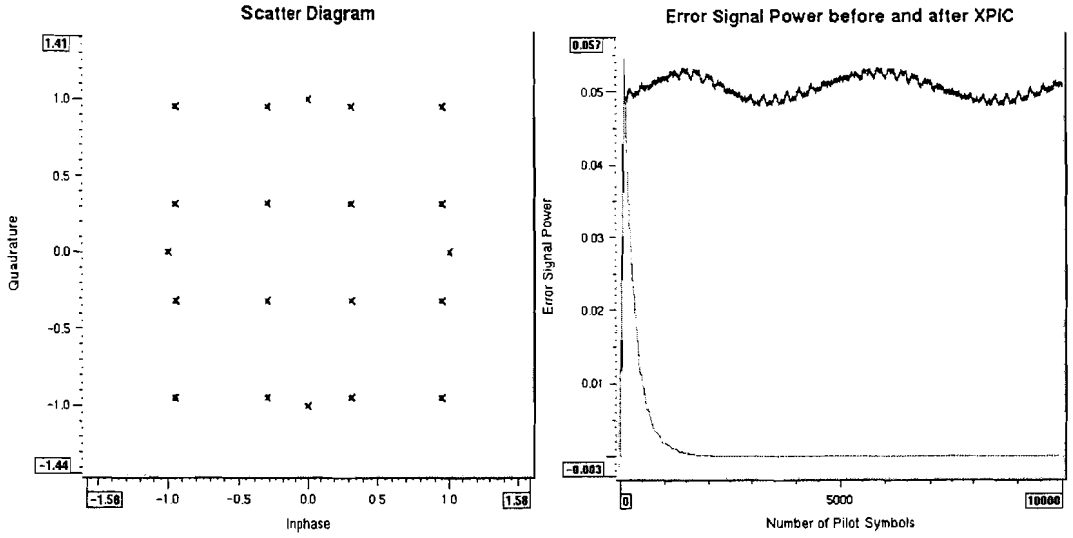

Figure 32: Simulation results for situation two

This situation enforces no restrictions on the oscillators at the transmitter side and signal exchange is made at IF level, thus only an interconnection between the down-converters in the receiver should be made [11], [13], [14].

For case three the simulation results are shown in Figure 33.

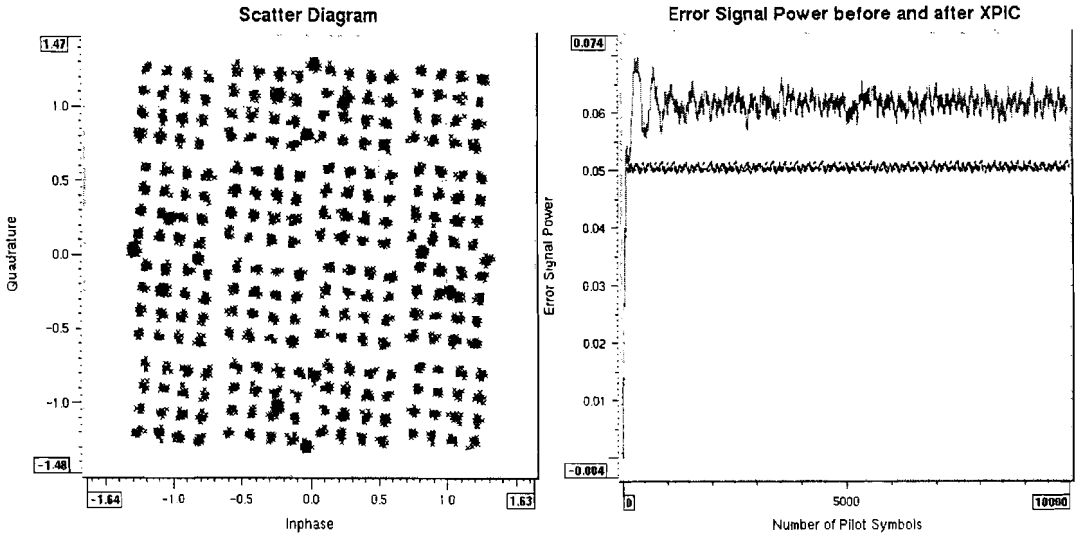

Figure 33: Simulation results for case three

Due to the fact that the horizontally and vertically polarized received signals are down-converted by different oscillators a frequency offset appears between the XPIC's error signal and the XPIC's input signal. This frequency offset results in a continuous change of the optimum filter tap-weights, which can be shown with the same analysis as in subchapter 5.1.2.3 for the case of a symbols spaced XPIC. The horizontal and vertical received baseband signals are in this case given by

$$u_H(n) = \sqrt{1-\gamma}\,a_H(n) + \sqrt{\gamma}\,a_V(n) + v_H(n)$$
$$u_V(n) = \left[\sqrt{1-\gamma}\,a_V(n) + \sqrt{\gamma}\,a_H(n) + v_V(n)\right] e^{j2\pi\Delta f_R n}. \quad (80)$$

After some computations and taking into account that $\sigma_v^2 = 0$ and $\sigma_a^2 = 1$ this will result in the following optimal tap weights for the symbol spaced XPIC

$$\mathbf{w}_{VH,opt} = \left[0 \;\cdots\; 0 \;\; \frac{\sqrt{\gamma}}{\sqrt{1-\gamma}} e^{j2\pi\Delta f_R n} \;\; 0 \;\cdots\; 0\right]^T. \quad (81)$$

The optimal tap weights for the fractionally spaced XPIC take on the same time varying form, but the exact values are difficult to derive.

The simulation results show a lack of convergence because of the fact that an adaptive filter structure is not able to converge to a changing optimum. However when the variations of the optimal tap weights are "slow" enough the XPIC gains the ability to

track those variations to some extent. To what degree depends on the value for the step-size parameter μ. An algorithm with a larger step-size parameter is able to track faster variations than a algorithm with smaller step-size parameter, but as a consequence a bigger excess mean squared error of the tap weights (see Eq. (28)) in the case of $J_{\min} \neq 0$ must be permitted. However the step-size parameter cannot be chosen arbitrary. When it is chosen too large the adaptive filter becomes unstable. The range, which the step-size parameter is allowed to take on, has been given in Chapter 3. For this case this results in

$$0 < \mu < 0.117 \qquad (82)$$

Taking the step-size parameter ten times as high (μ=0.01), gives the XPIC the ability to partially track the frequency offset, see Figure 34. Increasing the step-size parameter to μ=0.1 leads to even better tracking results, see Figure 35. But large peaks can be seen in error signal power curve, due to the fact that this step-size parameter is close to the upper bound of instability.

Though the individual carrier recovery loops of the receivers are able to compensate for the additional baseband frequency offsets, eliminating the frequency offset between the XPIC's error signal and the XPIC's input signal, resulting in convergence recovery of the XPIC. When zero-frequency offset is achieved the XPIC is again able to totally compensate for the interferences [10], [17], [18].

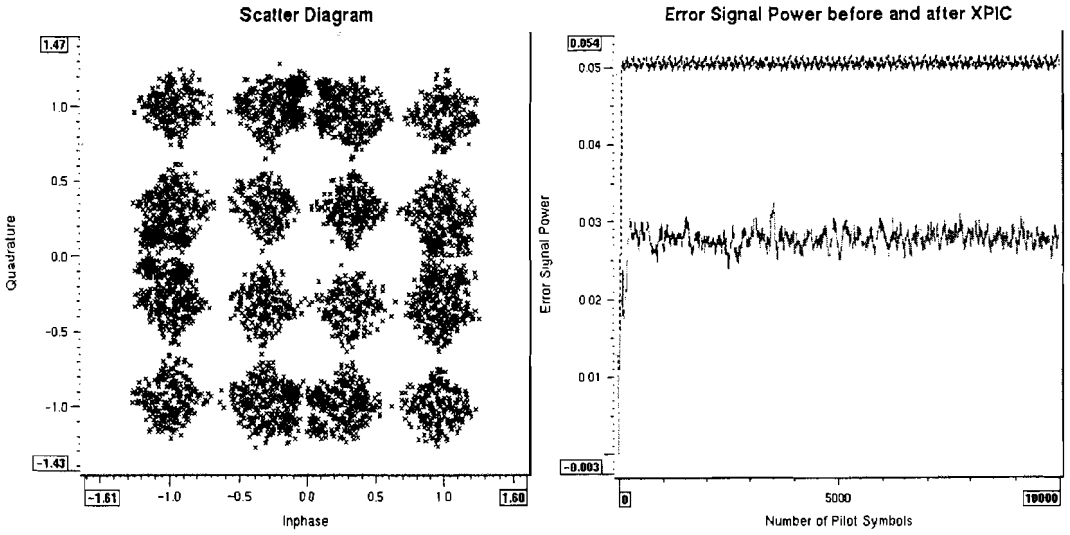

Figure 34: Simulation results for case three with μ=0.01

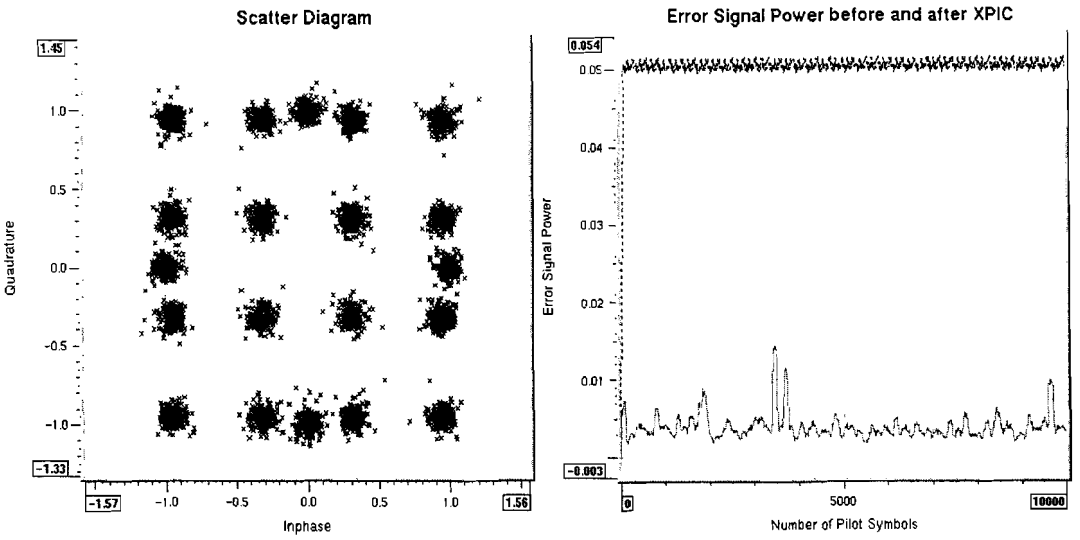

Figure 35: Simulation results for case three with μ=0.1

In Figure 36 the results of situation four are presented.

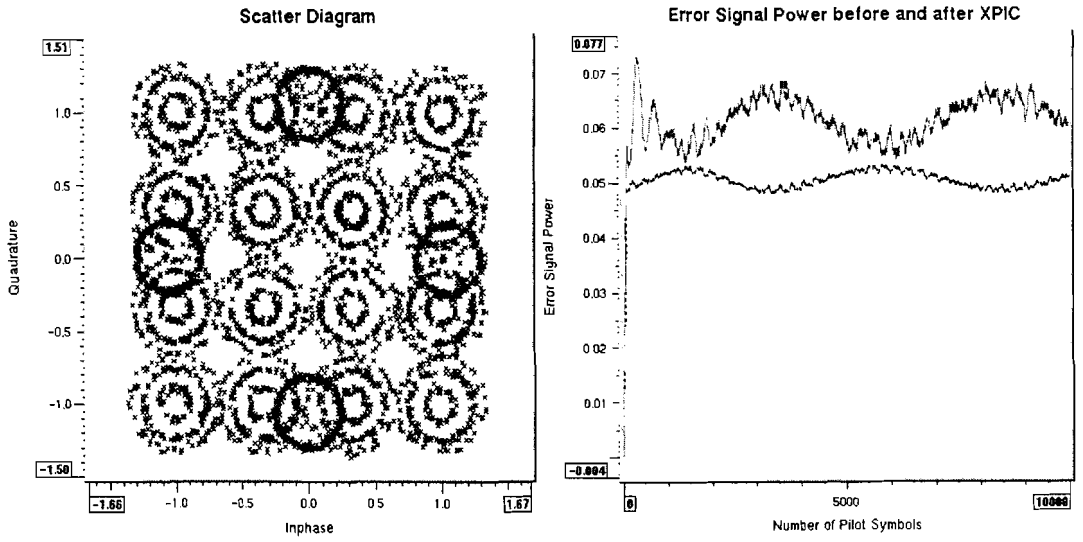

Figure 36: Simulation results for situation four

In this case all signals show mutual frequency offsets and there is no way to compensate for all these offsets. The horizontal and vertical received baseband signals are given by

$$u_H(n) = \sqrt{1-\gamma}\,a_H(n) + \sqrt{\gamma}\,e^{j2\pi\Delta f_T n} a_V(n) + v_H(n) \qquad (83)$$
$$u_V(n) = \left[\sqrt{1-\gamma}\,e^{j2\pi\Delta f_T n} a_V(n) + \sqrt{\gamma}\,a_H(n) + v_V(n)\right] e^{j2\pi\Delta f_R n}.$$

Even if the carrier recovery loops of the receivers are able to compensate for the zero-frequency offsets, a frequency offset will still exist between the XPIC's error signal and the XPIC's input signal. From the scatter diagram of

Figure 36 the rotating nature of the interference contribution clearly shows up. Also this frequency offset can be tracked if the step-size parameter is increased.

5.1.4.4 Interpretation of the Simulation Results

In principle both the synchronized transmitter approach and the synchronized receiver approach are sufficient to ensure XPIC convergence with the chosen step-size parameter. These conclusions are similar to the ones proposed in the literature. To be able to chose between one of the two proposed methods, it must be clear what situation is preferred.

A synchronized transmitter side leads to interconnections between the two transmitters to synchronize the modulator and up-converter and to interconnections between the receivers, because the XPIC's input signal needs to be extracted from the differently polarized receiver. In the receivers less components are needed because the signal exchange can be made after A/D conversion. A prerequisite is a carrier recovery lock state.

A synchronized receiver leads to one more interconnection at the receiver side then in the previous case, because down-converters need to be synchronized. No changes have to be made at the transmitter side. The XPIC is able to work even without a carrier recovery lock state. However extra components like demodulators, filters, A/D converters are needed, because the signal exchange is made at IF level.

I would recommend a synchronized receiver side, due to the fact that it is independent of the carrier lock-in state, and besides it leaves the transmitter side untouched. I consider including extra modules in the path of the XPIC, like demodulators and A/D converters of minor significance, because the extra costs of those modules are small.

5.1.5 Phase Shifts in the Channel Paths

5.1.5.1 Problem Sketch

Until now channel paths are considered where only attenuation effects played a role, but the channel paths normally suffer from phase shifts too. This results in an extended channel model depicted in Figure 37. The phase shifts in the direct paths are denoted by φ_H and φ_V, and the phase shifts in the interference paths by φ_{HV} and φ_{VH}.

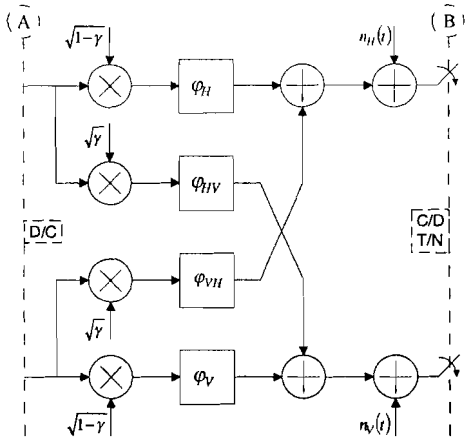

Figure 37: Channel model with phase shifts

In [3] and [17] it is shown that in case of bi-directional XPI the performance of the XPIC controlled by the LMS algorithm is dependent on the phase relationship between the direct and interference channel paths. The following phase relation has been shown favorable

$$\varphi_H + \varphi_V = \varphi_{HV} + \varphi_{VH} - \pi + k(2\pi) \tag{84}$$

for k an integer.

A different channel leads to a different optimal parameter for the AGC. In this situation the horizontal and vertical baseband signals are given by

$$\begin{aligned} u_H(n) &= \sqrt{1-\gamma}\, e^{j\varphi_H} a_H(n) + \sqrt{\gamma}\, e^{j\varphi_{VH}} a_V(n) + v_H(n) \\ u_V(n) &= \sqrt{1-\gamma}\, e^{j\varphi_V} a_V(n) + \sqrt{\gamma}\, e^{j\varphi_{HV}} a_H(n) + v_V(n). \end{aligned} \tag{85}$$

When the same derivations are applied as in section 5.1.2.3, this results after some computations in the following optimal AGC parameter

$$w_{AGC,H} = \sqrt{1-\gamma}\, \frac{\left(1+\frac{\sigma_v^2}{\sigma_a^2}\right) e^{j\varphi_H} - \gamma e^{j\varphi_{HV}} \left(e^{j(\varphi_H - \varphi_{HV})} + e^{j(\varphi_{VH} - \varphi_V)} \right)}{\left(1+\frac{\sigma_v^2}{\sigma_a^2}\right)^2 - 2\gamma(1-\gamma)\left[1+\cos(\varphi_H + \varphi_V - \varphi_{HV} - \varphi_{VH})\right]}. \tag{86}$$

The corresponding minimum mean squared error is given by

$$J_{\min} = \frac{\sigma_v^2 \left(1+\frac{\sigma_v^2}{\sigma_a^2}\right)}{\left(1+\frac{\sigma_v^2}{\sigma_a^2}\right)^2 - 2\gamma(1-\gamma)\left[1+\cos(\varphi_H + \varphi_V - \varphi_{HV} - \varphi_{VH})\right]}. \tag{87}$$

When no noise ($\sigma_v^2 = 0$) is introduced $J_{\min}$=0. The interference signal can be perfectly compensated for all possible phase shifts. On the contrary, in the presence of noise $J_{\min}$ has a minimum that is reached when the second term of the denominator is zero. With XPI this term is indeed zero if the phase condition of Eq. (84) holds, even in the worst case of interference γ=0.5. The phase condition leads to $\mathbf{r}_{VH} = \mathbf{r}_{HV}^* = E\left[\mathbf{u}_V(n)u_H^*(n-D)\right] = [0 \ \cdots \ 0]^T$, thus when the cross-correlations between vertical and horizontal input signal are zero the system performs best. AGC and XPIC are then only working on the auto-correlation contributions, $r_{HH} = E\left[u_H(n-D)u_H^*(n-D)\right]$ respectively $\mathbf{R}_{VV} = E\left[\mathbf{u}_V(n)\mathbf{u}_V^H(n)\right]$, and can be seen to work independently. When the ideal phase condition does not hold the AGC and XPIC influence each other via de cross-correlation parts.

Next a special case is considered. The channel is assumed symmetric and there are only phase shifts applied to the interference paths, leading to $\varphi_H = \varphi_V = 0$ and $\varphi_{HV} = \varphi_{VH} = \varphi$. For this case $J_{\min}$ is plotted in Figure 38 in the phase range of $0 \le \varphi \le 360$ for a SNR of 20 dB and interference levels of γ=0.05, γ=0.1, γ=0.25, γ=0.4 and γ=0.5.

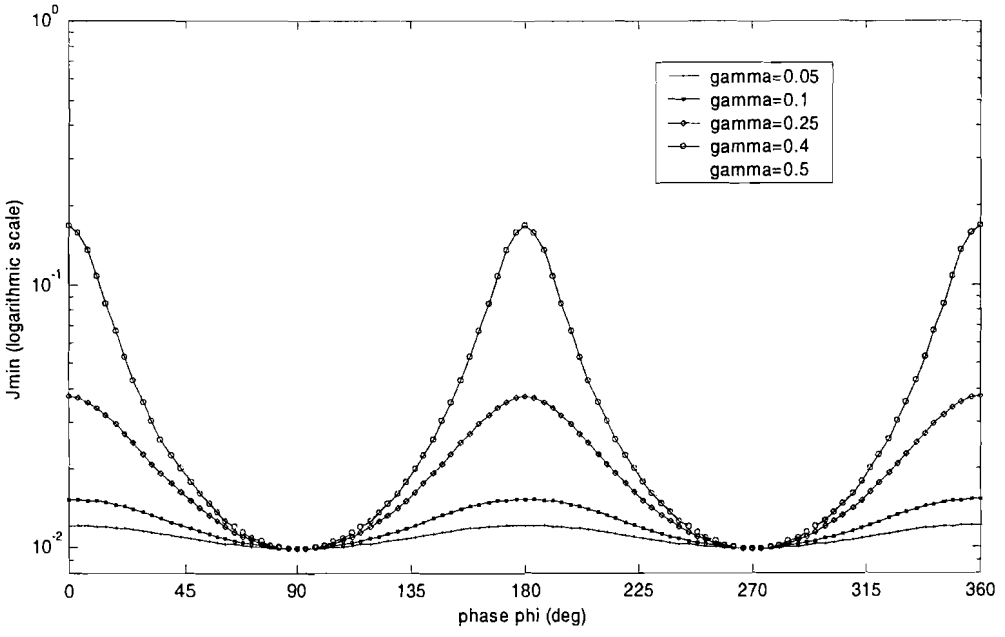

Figure 38: Minimum mean squared error versus phase and interference level

In case of a SNR of 20 dB ($\sigma_v^2 / \sigma_a^2 = 0.01$) and $\sigma_a^2 = 1$ the minimum value of the minimum mean squared error is reached for $\varphi = \pi / 2$ and equals

$$J_{\min} = \frac{\sigma_v^2}{\left(1 + \frac{\sigma_v^2}{\sigma_a^2}\right)} \approx 0.01 \ (= -20dB) \ . \qquad (88)$$

Hence in this case it is preferable to have phase shifts close to $\pi/2$ in the cross channel branches. In reality however the phase shifts in the channel branches cannot be influenced.

The prior analysis holds if the AGC can take on complex values, because the optimal AGC coefficient takes on complex values as denoted in Eq (86). However the AGC in our structure compensates the gain by comparing the amplitude of the received pilots with the amplitude of the reference pilots, it can therefore only correct the amplitude. Accordingly it is not possible to produce the optimal AGC parameter. The AGC parameter $w_{AGC,H}$ can only take on the amplitude of the optimal value, for $\sigma_v^2 = 0$, $\sigma_a^2 = 1$, $\varphi_H = \varphi_V = 0$ and $\varphi_{HV} = \varphi_{VH} = \varphi$ this is

$$|w_{AGC,H}| = \frac{\sqrt{1-\gamma}}{\sqrt{1-4\gamma(1-\gamma)\cos^2\varphi}}. \qquad (89)$$

This will result in an extra phase error on top of the minimum mean squared error $J_{\min}$. This effect is shown in Figure 39, $a_{H,TOT}(n)$ represents total of the horizontally polarized contributions behind the point where the compensation signal from the XPIC is added.

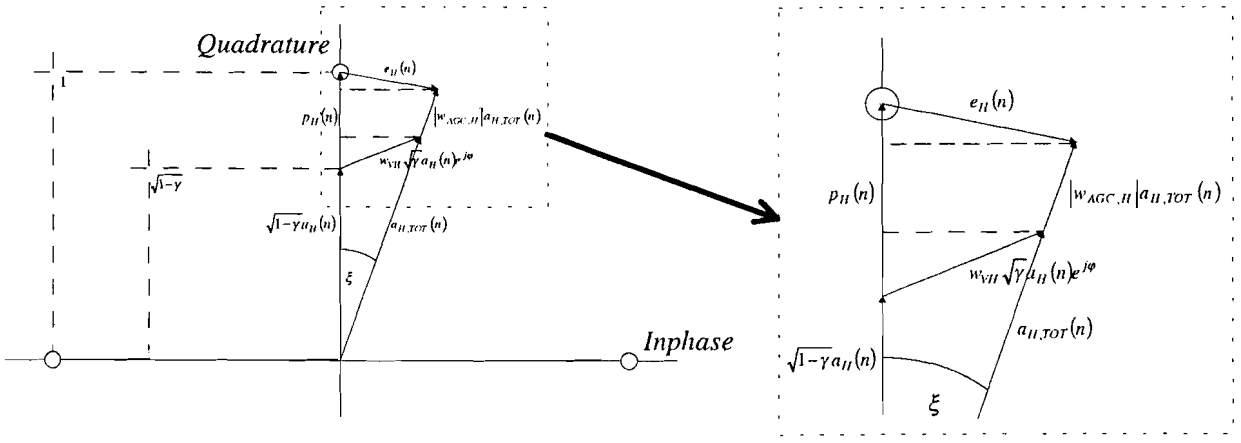

Figure 39: Error due to AGC constraint

However when the pilots are rotated by the angle ξ the limitations of the AGC do not show up anymore, see Figure 39. In the Nokia radio this problem is counteracted by the Phase Estimator (PE). The PE is depicted in Figure 40. It performs two operations.

The first part is really straightforward, the reference pilots take on the same phase as the pilots inside the data stream. This is done by extracting the phase $\theta_{p\_data}(n)$ of the pilots $z_{p,H}(n)$ inside the data stream $z_H(n)$. These pilots are indicated by a trigger signal, not shown in Figure 40. Feeding the phase $\theta_{p\_data}(n)$ to the amplitude of the reference pilots $p_H(n)$ results in the rotated reference pilots $p_{H,rot}(n)$. The feedback loops of the different modules now use the rotated reference pilots for computing their error signal.

The second part, performs the actual phase estimation for the data symbols using the phase error $\theta_{p\_error}(n)$ of the pilots. The implementation of this process is considered to be confidential by Nokia and is therefore not shown. The result is the phase corrected signal $z_{H,\theta}(n)$.

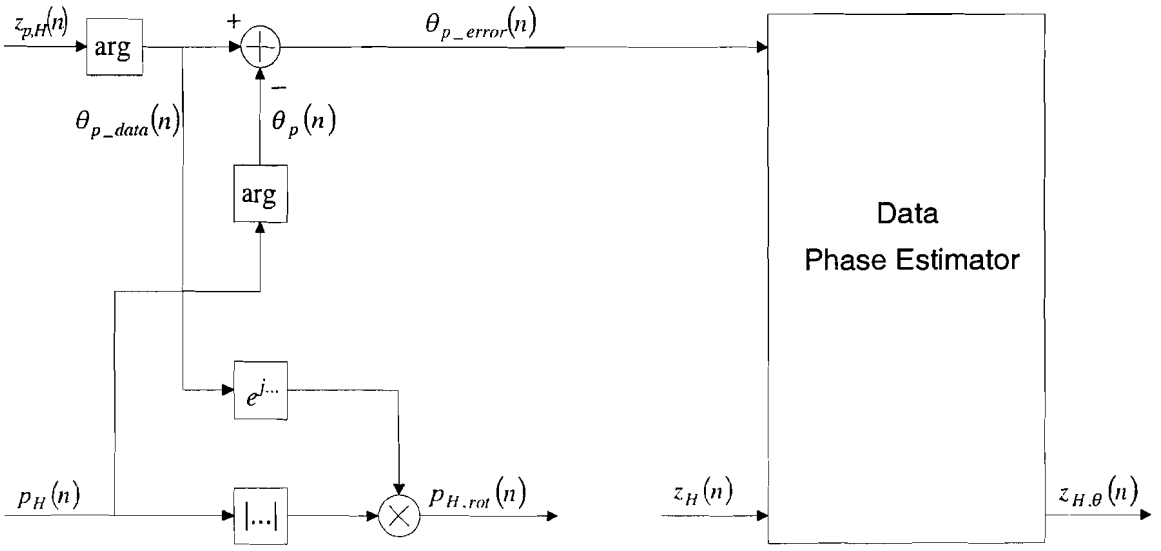

Figure 40: PE structure

5.1.5.2 Simulation Outline

The channel is again assumed symmetric with $\varphi_H = \varphi_V = 0$ and $\varphi_{HV} = \varphi_{VH} = \varphi$. A receiver structure with fractionally spaced XPIC is implemented, resulting in a delay of D=4 and a downsample factor of L=2. Three different situations are analyzed in the phase range of $0 \le \varphi \le 360$:

1. *A receiver structure with real valued AGC is considered. This receiver structure does not include the gray areas in Figure 41. The channel is assumed noiseless.*
2. *A receiver structure with real valued AGC is considered. Again the receiver structure does not include the gray areas in Figure 41. The channel is assumed noisy.*
3. *A receiver structure with real valued AGC and PE is considered. It includes the gray areas in Figure 41. The AGC is implemented in this case as in Figure 19, with K set to 0.001. Furthermore the channel is assumed noisy.*

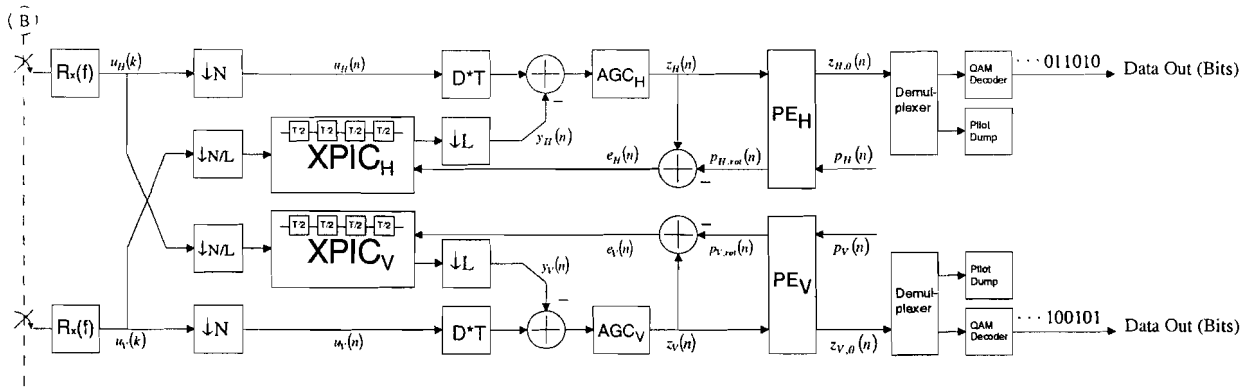

Figure 41: Receiver structure including the PE

5.1.5.3 Simulation Results

First, situation one is considered. The amplitude of the optimal AGC parameter differs form the actual value, consequently an error is introduced for every φ except at values of $\varphi=k\pi/2$, with k an integer. The error is plotted in Figure 42 on a logarithmic scale. From this figure it can be seen that the error interference ratio increase with a higher interference level and that the maximum is shifted towards the phase values $\varphi=k\pi$ for k an integer. The XPI level of $\gamma=0.5$ could not be simulated because the AGC parameter takes on an infinite value for $\gamma=0.5$.

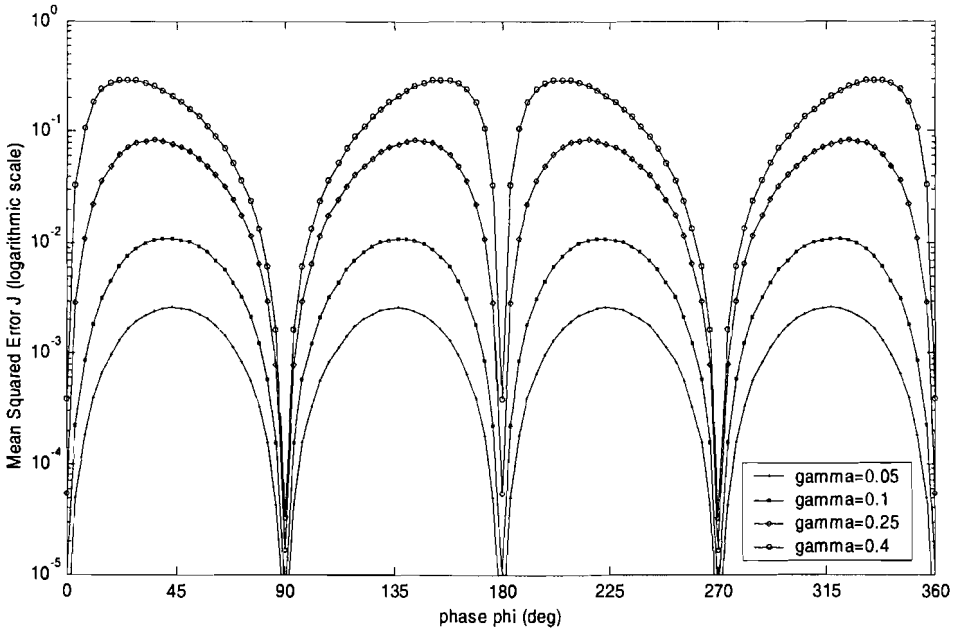

Figure 42: Introduced Mean Squared Error due to AGC constraint (logarithmic scale)

Second situation two is considered. In Figure 43 the mean squared error J versus the phase φ is plotted for an SNR of 20 dB. The amplitude of the optimal AGC parameter value is

$$\left|w_{AGC,H}\right| = \sqrt{1-\gamma}\,\frac{\sqrt{\left(1+\frac{\sigma_v^2}{\sigma_a^2}\right)^2 - 4\gamma\left(\left(1+\frac{\sigma_v^2}{\sigma_a^2}\right)-\gamma\right)\cos^2\varphi}}{\left(1+\frac{\sigma_v^2}{\sigma_a^2}\right)^2 - 4\gamma(1-\gamma)\cos^2\varphi}. \qquad (90)$$

The resulting curves in Figure 43 can be shown to be summations of the minimum mean squared error of Figure 38 and the mean squared error introduced due to limitations of the AGCs. An absolute minimum shows up if φ is a multiple of $\pi/2$. Thus a phase shift of $\pi/2$ in the cross-channels is again preferable.

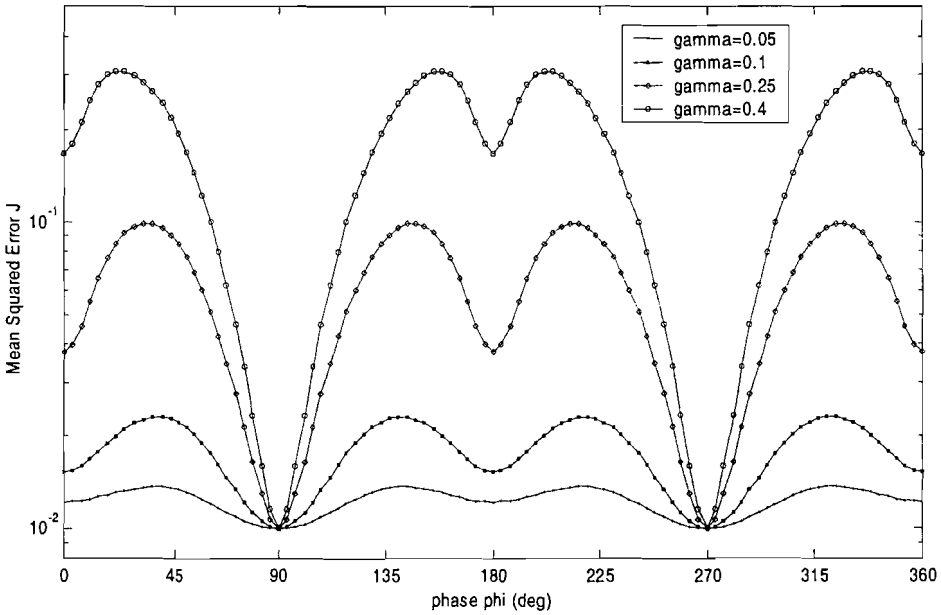

Figure 43: Mean Squared Error due to AGC constraint and noise (logarithmic scale)

The previous results show the impact of a real coefficient AGC without any countermeasures. Though, this degradation can be overcome when including the PE, as shown by the results in Figure 44.

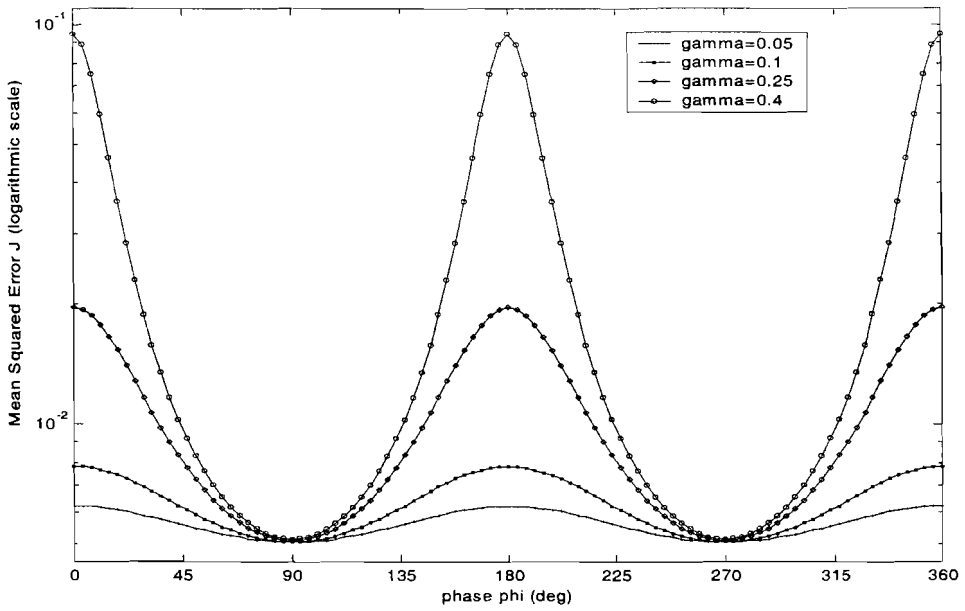

Figure 44: Mean squared error of the system with PE

When comparing Figure 44 with Figure 38 one must notice that the mean squared error curves in Figure 44 are half of that of Figure 38. The mean squared error for the optimal phase value ($\varphi = \pi / 2$) is approximately 0.005, which is twice as low as the noise level (0.01). This can be explained by the fact that the PE compensates the phase offset between the received pilots and the reference pilots exactly, including the phase difference introduced by the noise sources. So the noise sources only impact the amplitude of the error signal, which results in an improvement of a factor two. Of course this applies only for the pilot symbols and not for the data symbols in between the pilot symbols, due to the fact that the pilot symbols are know precisely. The data symbols are phase compensated by the PE, but after processing a remaining phase error will still exist because the noise contributions for each symbol are different. Finally it can be concluded that this solution separates the amplitude correction and the phase correction of the main (fixed) ATE coefficient. The amplitude correction is handled by the AGC and the phase correction is handled by the PE.

5.1.5.4 Interpretation of the Simulation Results

Phase shifts in the channel paths have influence on the performance of the XPIC and AGC. The performance is optimal when the phase condition holds, otherwise it is degraded according to Figure 38. Furthermore a receiver structure with a real valued AGC will cause additional performance degradation, because the phase shifts cause the optimal AGC parameter to be complex valued. This additional performance degradation does not show up when the real valued AGC is accompanied by the PE. The amplitude and phase corrections are then handled separately.

5.2 System Performance Simulations

The measurements in this section are related to the performance of the complete system, whereas the measurements in the previous sections were related to the performance of the XPIC in specific situations. The complete simulation environment is reflected in Appendix B.

5.2.1 System Considerations

The transmitters remain the same, except for the pilot spacing. A pilot spacing of 9 is adopted, analog to the NOKIA LYNX radio specifications [20]. For completeness the transmitters are again depicted in Figure 45. The output sample rate of the transmitter is equal to STM-1 (155.52 MHz).

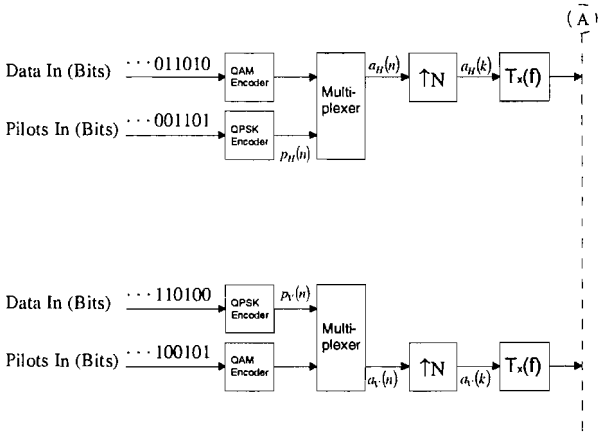

Figure 45: Transmitter structure

The channel model is extended to a general model depicted in Figure 46. This model is overall accepted in the literature [10], [17], [18], [21], representing XPI, multi-path propagation as well as containing two independent noise sources.

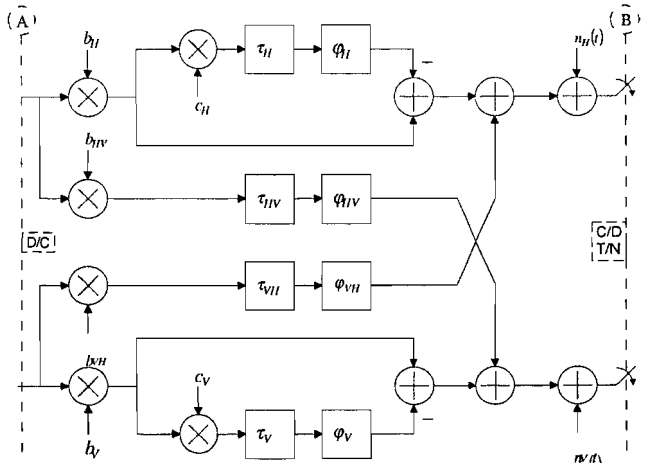

Figure 46: Channel model

The direct paths are modeled by a simplified three-ray Rummler channel by its originator W.D.Rummler and account for frequency selective fading due to multi-path propagation [22], [23]. The transfer functions of the Rummler channels for respectively horizontal and vertical polarization are given by

$$H_H(\Omega) = b_H\left(1 - c_H e^{-j(\Omega\tau_H - \varphi_H)}\right)$$
$$H_V(\Omega) = b_V\left(1 - c_V e^{-j(\Omega\tau_V - \varphi_V)}\right) \quad (91)$$

where b_H and b_V are scale parameters, c_H and c_V are shape parameters, τ_H and τ_V are the delay differences in the channels, and φ_H and φ_V are phase shifts representing the fade minimum or notch position. The notch depths are typically expressed in dB and are defined as $C_H = -20\log(1-c_H)$ and $C_V = -20\log(1-c_V)$. The power transfer function of a Rummler channel with $b = 0.1$, $c = 0.7$ and $\tau = 6.3\,\text{ns}$ is depicted in Figure 47, where $f - f_0 = 1/2\pi(\Omega - \varphi/\tau)$.

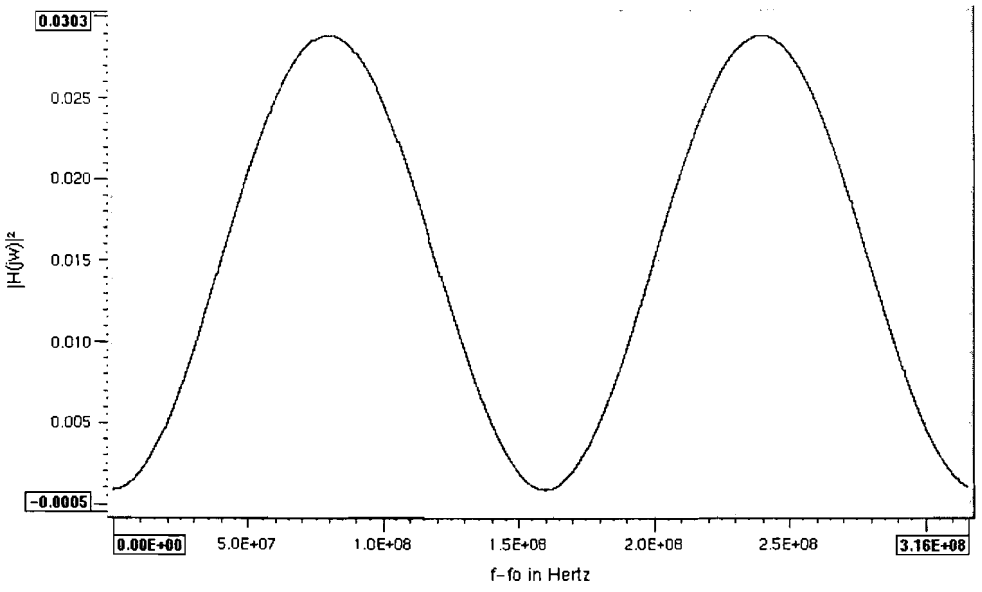

Figure 47: Power transfer function of Rummler Channel with b=0.1, c=0.7 and τ = 6,3 ns

Field trails have shown that the cross paths remain spectrally flat even in the case of multi-path propagation, thus the cross paths are modeled as non-frequency selective and only comprise scale parameters b_{HV} and b_{VH}, time delays τ_{HV} and τ_{VH} and phase shifts φ_{HV} and φ_{VH} [17], [21]. Their transfer functions are given by

$$H_{HV}(\Omega) = b_{HV} e^{-j(\Omega\tau_{HV} - \varphi_{HV})}$$
$$H_{VH}(\Omega) = b_{VH} e^{-j(\Omega\tau_{VH} - \varphi_{VH})}. \quad (92)$$

In the following simulations the parameters of the channel model are set to:

- $b_H = b_V = \sqrt{1-\gamma}$ and $b_{HV} = b_{VH} = \sqrt{\gamma}$.
- c_H and c_V are depending on the type of simulation.
- $\tau_H = \tau_V = 6.3\,\text{ns}$ recommended by W.D.Rummler.
- $\tau_{HV} = \tau_{VH} = 0$.
- $\varphi_H = \varphi_V = 0$ positioning the notch at the bandwidth's center frequency.
- $\varphi_{HV} = \varphi_{VH} = 0$ leading to worst case phase condition.

Both receivers have equal functionality, they are depicted in Figure 48. Rx pulse shaping filters are configured the same as before, just as the downsamplers. Furthermore the horizontal and vertical receiver both contain a fractionally spaced ATE and XPIC, with each 17 coefficients. Updating the coefficients of the XPICs and ATEs is done by means of the LMS algorithm. The step-size parameters for the ATEs and XPICs are set to 0.001. Furthermore the real center coefficients of the ATEs are fixed to 1 and the imaginary center coefficients to 0. After ATE and XPIC the signals are downsampled to symbol rate and summed. Horizontally and vertically polarized receiver also include an AGC and PE, with the loop constant K of the AGC set to 0.001.

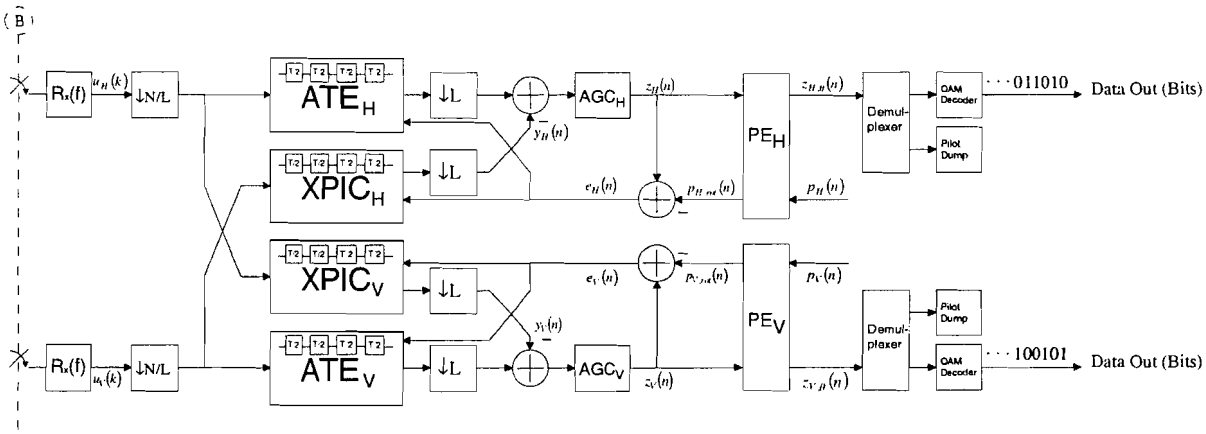

Figure 48: Receiver structure

The transmitters and receiver models do not include any correlated phase noise sources because it dramatically increases the simulation time. Laboratory experiments should provide adequate measurements concerning this matter.

The performance of the system is monitored by measuring the Bit Error Rate (BER) behind the QAM decoder. Several system performance measurement methods are outlined in [24]. A commonly accepted one, varies the amount of XPI/XPD for certain SNR until a specified BER is reached. This is done for a system with and without XPIC. The difference is a measure for the XIF. Another useful measurement measures the XIF for a specified SNR and BER in case of a multipath channel model with different notch depths.

5.2.2 Flat Channel System Measurements

In these measurements the notch depth parameters c_H and c_V are set to 0. The amount of XPI is varied for a system with XPIC and without XPIC until a BER of 10^{-3} is reached. A BER of 10^{-3} is adopted to control the simulation execution time. The results are depicted in Figure 49. The XIF for a SNR of 40 dB is 13.19 dB, which means that the system with XPIC is able to handle 13.19 dB less XPD than the system without XPIC. Concluding it can be said that the use of an XPIC is profitable, especially in cases where the XPD is not so high.

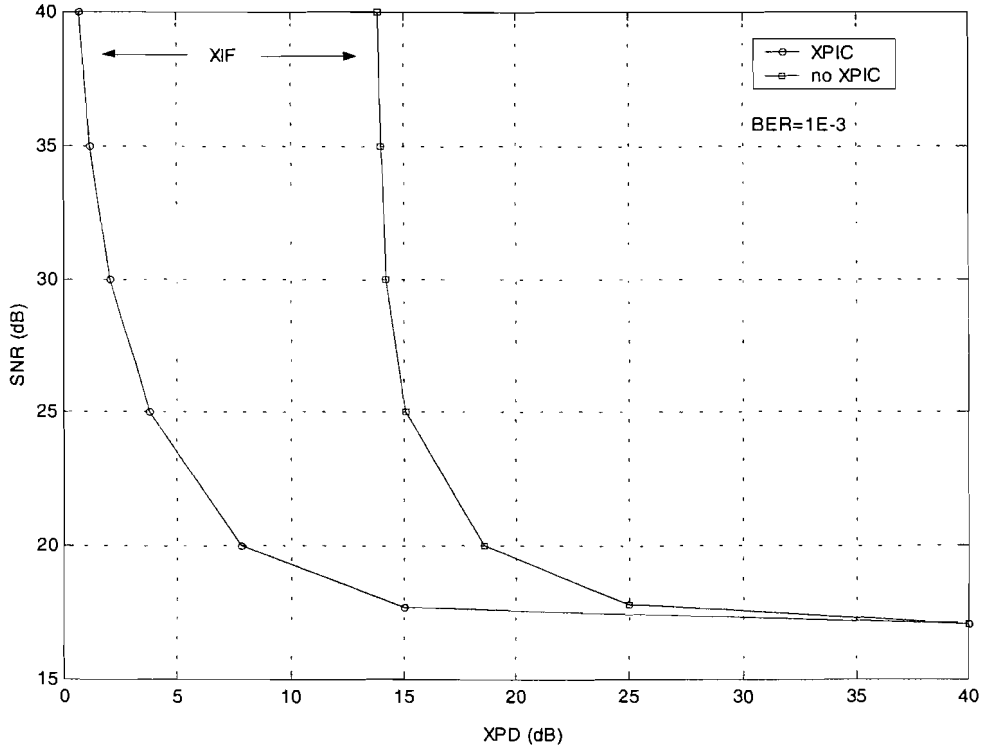

Figure 49: BER measurements for system with and without XPIC

5.2.3 Multipath Channel System Measurements

These measurements provide a mean for the performance difference between a system with XPIC and a system without XPIC in the case of multipath fading and a BER of 10^{-3}. The notch is positioned at the center frequency ($\varphi_H = \varphi_V = 0$). The notch depths C_H and C_V are varied in the range of 0 to 20 dB. The results are depicted in Figure 50. From Figure 50 it can be said that the XIF decreases when the notch deepens, but the XIF is still 11.21 dB for a notch depth of 10 dB. Even in the case of severe multipath fading (notch depth 20 dB) a system with XPIC is still able to handle 5.79 dB less XPD than a system without XPIC. Finally it can be concluded that also in the case of multipath propagation the use of an XPIC is profitable.

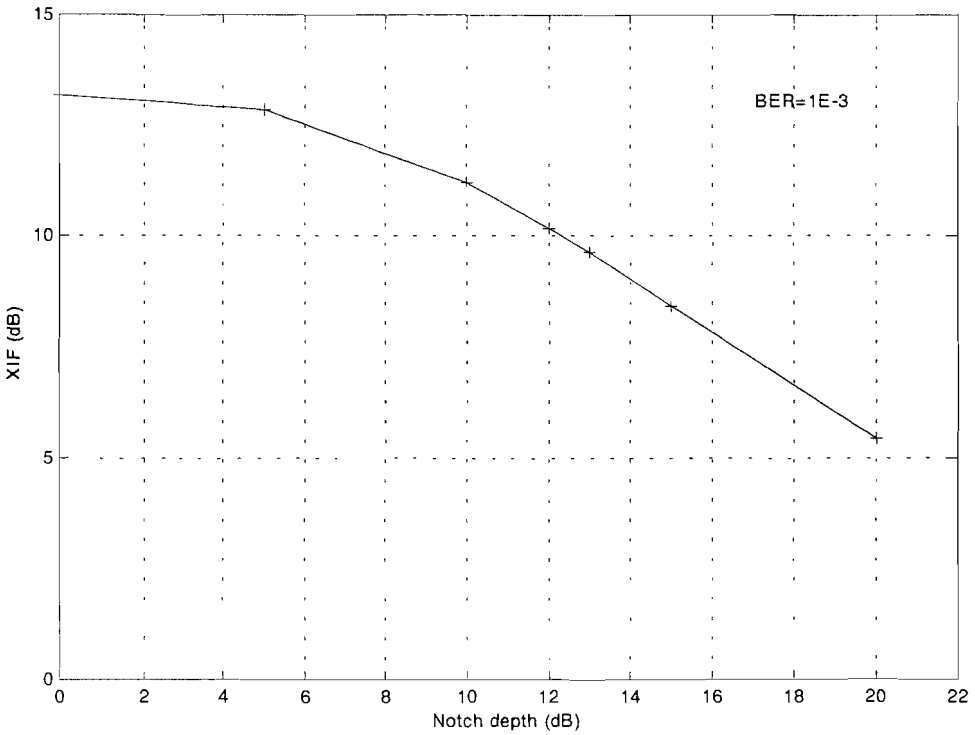

Figure 50: BER measurements for a system's XIF in the presence of multipath fading

6. Conclusions

In this report several problems relating to the integration of an XPIC into an existing Nokia radio architecture have been studied. Results are derived on a simulation basis, supported with theoretical analyses. Detailed description is given of the transmitter, channel, and receiver structures and in specific the functionality of the XPIC and the related units is treated intensively.

First of all several XPIC and AGC combinations are considered. The best position for the AGC from a simulation point of view as well as from a theoretical point of view is found to be behind the XPIC. The other AGC locations lead to residual gain errors. However equally well results can be achieved when the AGC's gain correction takes place at each of the considered positions, if only the error signal of the AGC is derived behind the XPIC. However, this will lead to a smaller loop bandwidth of the AGC, decreasing the tracking capability.

Secondly, the performance of a symbol spaced XPIC is compared to the performance of a fractionally spaced XPIC under several types of signal delays. A symbol spaced XIPC and a fractionally spaced XPIC are shown to be both capable of compensating symbol delays. A symbol spaced XPIC is able to handle twice as much symbol delay as a fractionally spaced XPIC when both structures have the same amount of taps. On the other hand a fractionally spaced XPIC is able to handle fractional delays without performance loss, whereas a symbol spaced XPIC experiences some difficulties. Though when a symbol spaced XPIC is combined with a Elastic Storage (ES) it will perform equally good, due to the capability of an ES to synchronize data streams. Of course this creates the need for an extra module, resulting in a more complex schematic.

Thirdly, the dependency of synchronized transmitters and receivers on the operation of the XPIC is considered. It has been pointed out that synchronization of only the transmitters or the receivers is sufficient to ensure XPIC convergence. A choice between one of the two possibilities depends on the preferred situation.

A synchronized transmitter side leads to interconnections between the two transmitters, to synchronize the modulator and up-converter as well as to interconnections between the receivers, to derive the input of the XPIC. In the receivers less components are needed because the signal exchange can be made after the A/D converter. A prerequisite is a carrier recovery lock state.

A synchronized receiver leads to interconnections at the receiver side, because down-converters need to be synchronized and the input of the XPIC must be derived, but no interconnections have to be made at the transmitter side. The XPIC is able to work even without a carrier recovery lock state. However extra components like demodulators, filters, A/D converters are needed, because the signal exchange is made at IF level.

Fourthly, the influence of phase shifts in the channel paths on the performance of the XPIC is considered. It has been shown that phase shifts in the channel paths influence the performance of the XPIC and AGC. The performance was shown to be optimal when the phases of the main channel paths and the cross channel paths differ 180 degrees. Furthermore a receiver structure with a real valued AGC will cause additional performance degradation, because the phase shifts cause the optimal AGC parameter to be complex valued. This additional performance degradation does not show up when the real valued AGC is accompanied by a PE. The amplitude and phase corrections are then handled separately.

Finally the integration of an XPIC in a Nokia specific radio system is shown to be profitable. The performance of the system increases when a channel suffers from XPI, also in the case of multipath propagation.

7. Recommendations

I would recommend a receiver structure implemented with a fractionally spaced XPIC consisting of the same number of taps as the ATE. Furthermore I would recommend a synchronized receiver side, due to the fact that it is independent of the carrier lock-in state, and besides it leaves the transmitter side untouched. I consider including extra modules in the path of the XPIC, like demodulators and A/D converters of minor significance, because the extra costs of those modules are small. I would also recommend to place the AGC behind or at least derive the error signal of the AGC from behind the point where the signal from the XPIC is added.

Most probably the XPI contribution will interfere with the slow carrier recovery loop and the timing recovery loop, therefore the optimal solution might be adding the XPI cancel contribution of the XPIC in front of the feedback of the slow carrier recovery loop and the timing recovery loop. This would be behind the receiver's pulse shaping filter. The effect of XPI on the functioning of the slow carrier loop and the timing recovery loop should be made clear and will therefore need to be subjected to investigation in the future.

The XPIC depends on the pilot detection block in the receiver, meaning that the XPIC does not work when the pilots are not detected. This might make it necessary to introduce blind adaptation techniques until the pilots are detected. The dependency of the pilot detection lock-in state on XPI should be investigated. Investigations at Nokia revealed the need for these techniques for the ATE. The algorithm used for the blind adaptation in the ATE is the Godard algorithm or also called the Constant Modulus Algorithm (CMA).

Finally it is good to say that it is known that fractionally spaced adaptive filter structures like the one presented for the XPIC can lead to tap wandering, increasing the tap coefficients and maybe causing a register overflow. Deeper investigation of the fractionally spaced XPIC should clarify this and suitable solutions should be presented. Possible solutions for this problem could be the simple tap-leakage algorithm or the more complicated algorithm presented by Uyematsu and Sakaniwa.

8. List of Abbreviations

A/D	Analog / Digital
ADC	Analog Digital Converter
AGC	Automatic Gain Control
AP	Alternating Pattern
ATE	Adaptive Transversal Equalizer
BB	BaseBand
BER	Bit Error Rate
CMA	Constant Modulus Algorithm
CC	Co-Channel
DA	Decision Aided
DAC	Digital Analog Converter
DFG	Data Flow Graph
ES	Elastic Storage
ETSI	European Telecommunications Standard Institute
FIFO	First In First Out
FIR	Finite Impulse Response
GSM	Global System for Mobile communication
ISI	Inter Symbol Interference
IF	Intermediate Frequency
LMS	Least Mean Square
NDA	Non Decision Aided
PDH	Plesiochronous Digital Hierarchy
PE	Phase Estimator
QAM	Quadrature Amplitude Modulation
QPSK	Quadrature Phase Shift Keying
RF	Radio Frequency
SDH	Synchronous Digital Hierarchy
SNR	Signal to Noise Ratio
STM	Synchronous Transport Module

TCM	Trellis Coded Modulation
UMTS	Universal Mobile Telecommunication System
XIF	XPIC Improvement Factor
XPD	Cross Polarization Discrimination
XPI	Cross Polarization Interference
XPIC	Cross Polarization Interference Canceller

9. References

[1] I. Henne and P. Thorvaldsen, "Planning of line-of-sight radio relay systems", Nera Telecommunications, Bergen, September 1999, p.99.

[2] I.R.A. Bahamonde, J.M.T. Romano and J.C.M. Mota, "On the adaptive filtering for cross-polarization interference canceler", IEEE International Telecommunications Symposium 1990, p.317-21.

[3] L. Scarabosio, "Influence of the phase relationship between direct path and interference path on XPIC performance", IEEE Globecom 1995, Communication for global harmony, Vol. 3, p.2017-21.

[4] S. Bregni, "A historical perspective on telecommunications network synchronization", IEEE Communications Magazine, June 1998, Vol. 36, no. 6, p.158-66.

[5] T.S. Rappaport, "Wireless communications principles and practice", Prentice Hall, New Jersey, 1996, p.270.

[6] S. Haykin, "Adaptive filter theory", Prentice-Hall, New Jersey, 1996.

[7] K. Vogel and K.J. Friederichs, "The benefit of cross-polar co-channel operation in digital radio networks", IEE Proceedings 4th ECRR 1993, Edinburgh, UK, p.167-74.

[8] G. Sebald, G. Filiberti, R. Schmidmaier and S. Bianchi, "A STM-1 XPIC-modem for 28/30 MHz cochannel applications", IEE Proceedings. 5th ECRR 1996, Bologna, Italy, p.265-71.

[9] B. Lankl, A. Nist, J.A. Nossek and G. Sebald, "Fully digital ATDE's and XPIC's for a STM-1 cochannel radio system family", IEEE World prosperity through communications ICC, 1989, Boston, Vol. 2, p.1013-19.

[10] B. Lankl and G. Sebald, "Optimization of XPIC-performance", IEEE Globecom 1990, Communications: Connecting the Future, Vol. 2, p.1196-202.

[11] R. Schmidmaier, G. Sebald, K.J. Friederichs, R. Macchi and M. Traverna, "A new cochannel radio system for 28/30 Mhz frequency spacing based on narrow-Band RF branching concept", IEE Proceedings 5th ECRR 1996, Bologna, Italy, p. 232-37

[12] R.D. Gitlin and S.B. Weinstein, "Fractionally-spaced equalization: an improved digital transversal equalizer", The Bell System Technical Journal, Vol. 60, No. 2, February 1981, p.275-96.

[13] R. Schmidmaier, S. Bianchi and E. de Man, "A new single chip QAM-modem for SDH and ATM systems", IEE Proceedings 7th ECRR 2000, Dresden, Germany, p. 115-22.

[14] P. Balducci, M. Bolla, L. Rossi and A. Spalvieri, "A new 32 QAM modem for doubling transmission capacity in 40 MHz channelling plans", IEEE Globecom 1992, Communication for global users, Vol. 3, p.1840-5.

[15] R.D. Gitlin, H.C. Meadors and S.B. Weinstein, "The tap-leakage algorithm: An algorithm for the stable operation of a digitally implemented, fractionally spaced adaptive equalizer", The Bell System Technical Journal, Vol. 61, No. 8, October 1982, p.1817-39.

[16] T. Uyematsu and K. Sakaniwa, "A new tap-adjustment algorithm: an algorithm for the stable operation of a digitally implemented, fractionally spaced adaptive equalizer", IEEE Globecom 1985, p.1420-3.

[17] M. Biester, E. Douverne, U. Hülsen, K. Ruthemann and W. Zimmer, "Hardware realization of an XPIC system/measurement method and results", IEE Proceedings 4th ECRR 1993, Edinburgh, UK, p.255-60.

[18] K.W. Suh, C.Y. Park, G.Y. Hur and D.Y. Lee, "A powerful 13-tap ATDE and XPIC implemented on one chip for co-channel digital radio systems", IEEE National Telesystems Conference 1994, p.201-6.

[19] ETSI DTR/TM04010: High capacity DRRS carrying SDH signals (1xSTM-1) in frequency bands with about 30 MHz channel spacing and using dual polarized (CCDP) operation.

[20] D. Gaschler et al. , "Lynx1b Specification 2.01b", Nokia Networks, Düsseldorf, August 2000.

[21] B. Lankl, J.A. Nossek and G. Sebald, "Cross-polarization interference cancellation in the presence of delay effects", IEEE Communications, ICC 1988, Digital Technology – Spanning the universe, Vol. 3, p. 1355-61.

[22] W.D. Rummler, "A new selective fading model: application to propagation data", The Bell System Technical Journal, Vol. 58, No. 5, May-June 1979, p.158-66.

[23] W.D. Rummler, "A multipath channel model for line-of-sight digital radio systems", Bell Telephone Laboratories, Holmdel, New Jersey, USA, IEEE ICC 1978, p.47.5/1-4.

[24] IEC 835-2-11: Method of measurement for digital microwave radio transmission systems. –Part 2: Measurements on terrestrial radio relay systems. –Section 11: Cross-polar interference canceller.

Appendix A: Timing Sensitivity Simulation Results

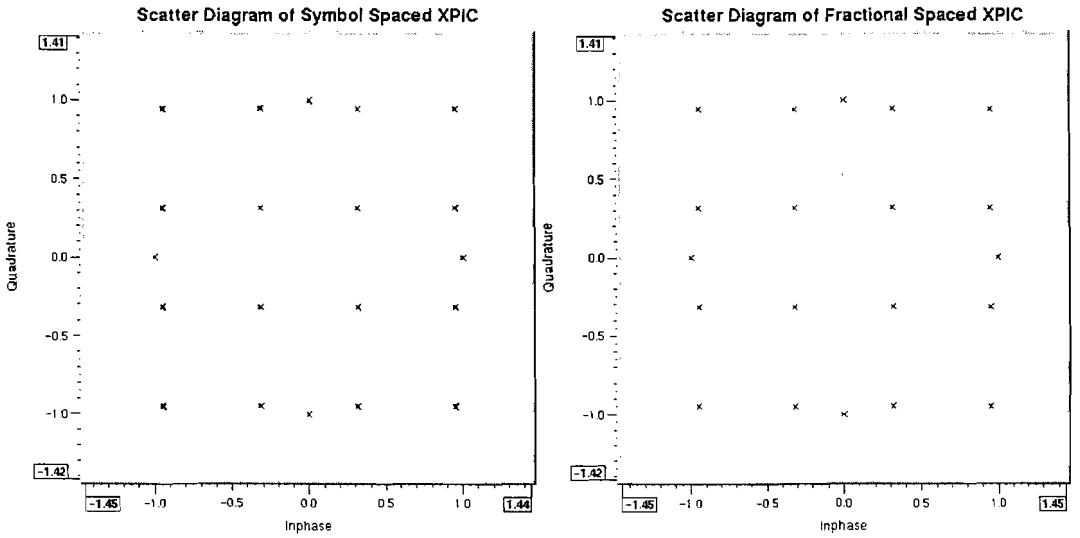

Figure 51: Scatter diagrams for situation 1 (ΔT=0)

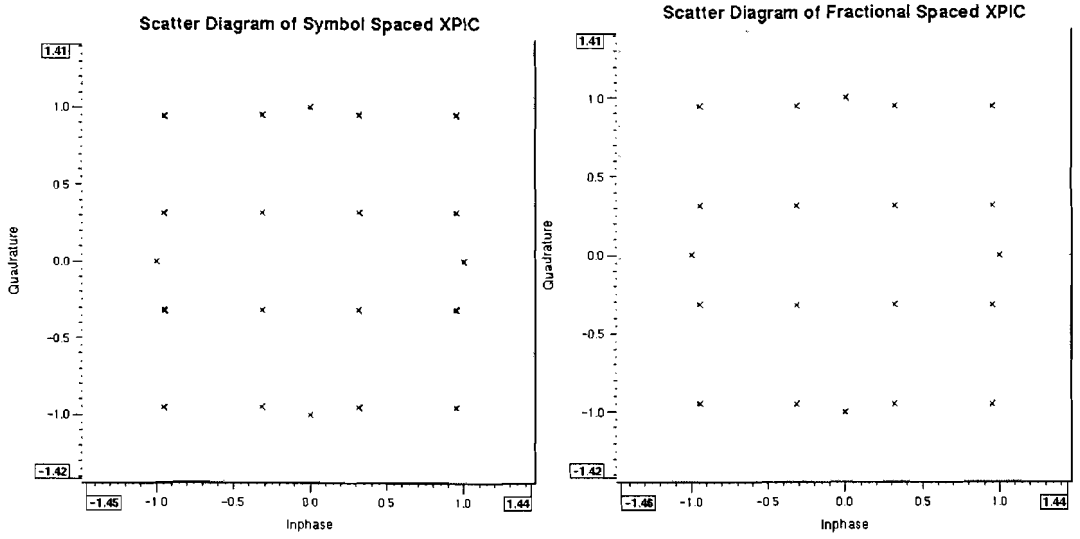

Figure 52: Scatter diagrams for situation 2 (ΔT=2)

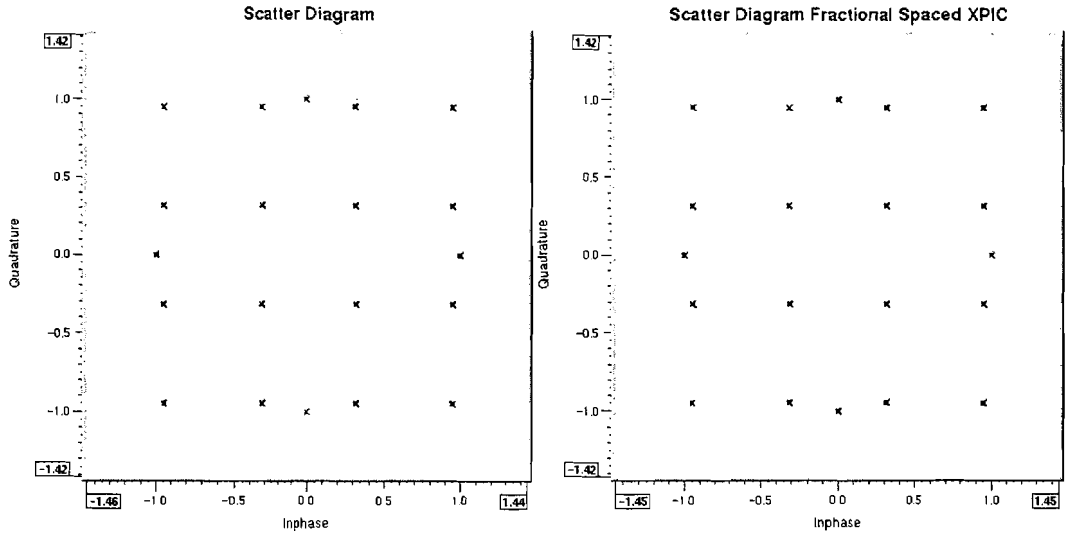

Figure 53: Scatter diagrams for situation 3 (ΔT=2¼)

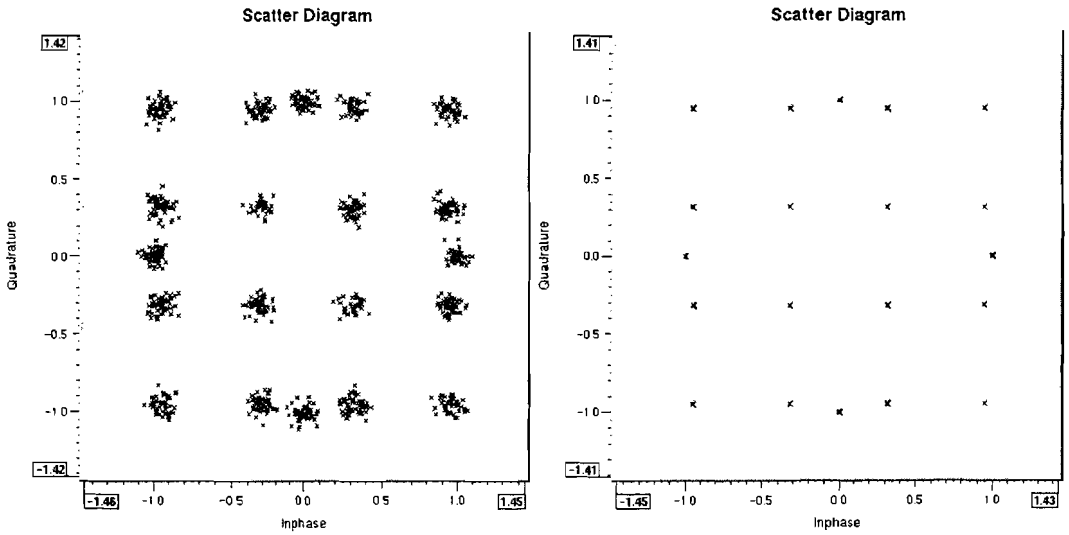

Figure 54: Scatter diagrams for situation 4 (ΔT=2½)

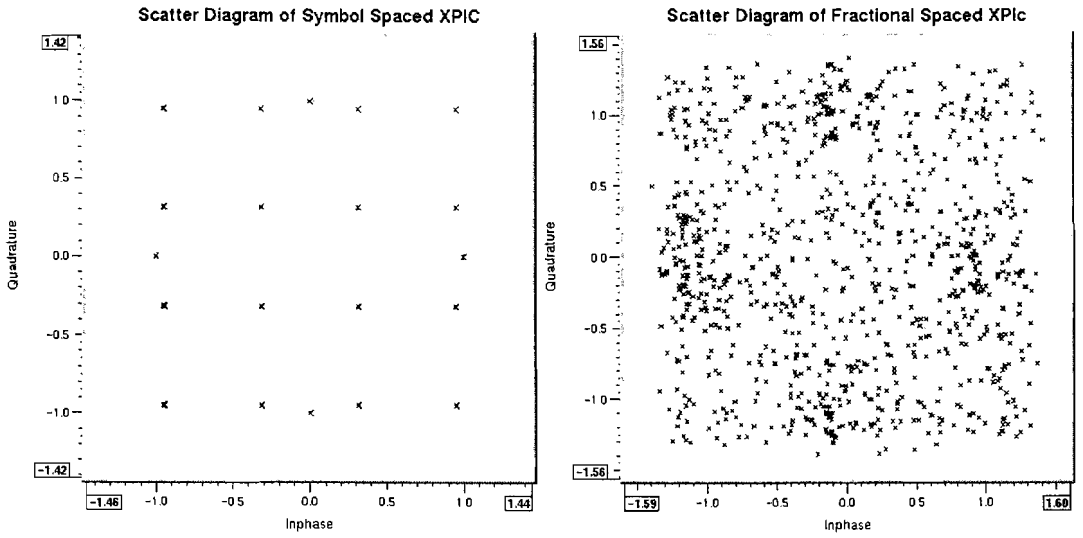

Figure 55: Scatter diagrams for situation 5 (ΔT=6)

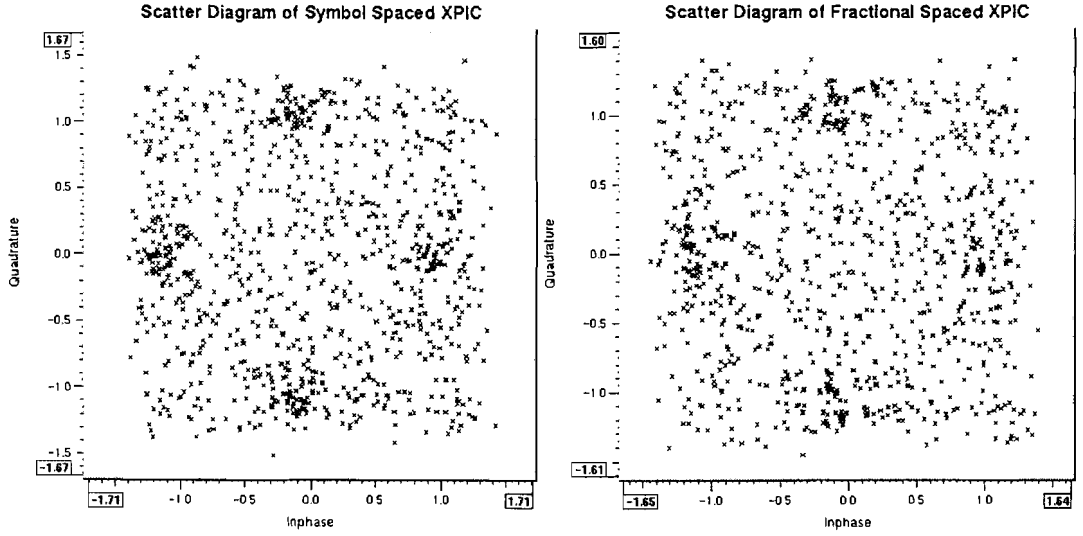

Figure 56: Scatter diagrams for situation 6 (ΔT=12)

Appendix B: Simulation Environment

This appendix gives an overview of the complete simulation environment and all of its sub-blocks –except for the PE– as used in the system performance simulations in Chapter 5. This simulation environment can also be used for the XPIC specific simulations when some small modifications are applied. Figure 57 depicts the top-level simulation environment –the PE dependent blocks are covered–, the main parameters of the top level simulation environment are explained in Table 1.

Table 1: Parameters of the top-level simulation environment

Parameter	Type	Description
M_QAM	Int	Number of QAM constellation points
Pilot_Spacing	int	The pilot spacing
Upsample_Factor	int	Upsample factor N in the horizontally and vertically polarized transmitters
Rolloff	double	Rolloff of the pulse shaping filters in horizontally and vertically polarized transmitters and receivers
FFTLength	int	Specifies the number of points of the pulse shape filters in FFT domain
Gamma	float	Interference parameter γ, which is a measure for the XPD
Shape_Parameter	float	Shape parameter $c = c_H = c_V$ of the Rummler channel in horizontally and vertically polarized channel branches
Noise_Power	double	Variance σ_v^2 of the noise sources in horizontally and vertically polarized channel branches
Downsample_Factor_H	int	Downsample factor N/L in horizontally polarized receiver
Downsample_Factor_V	int	Downsample factor N/L in vertically polarized receiver
Centertap_Delay	int	Delay of D symbols, caused due to fixing the center tap of the ATE
Stepsize_Parameter	float	The joint step-size for ATE, XPIC and AGC

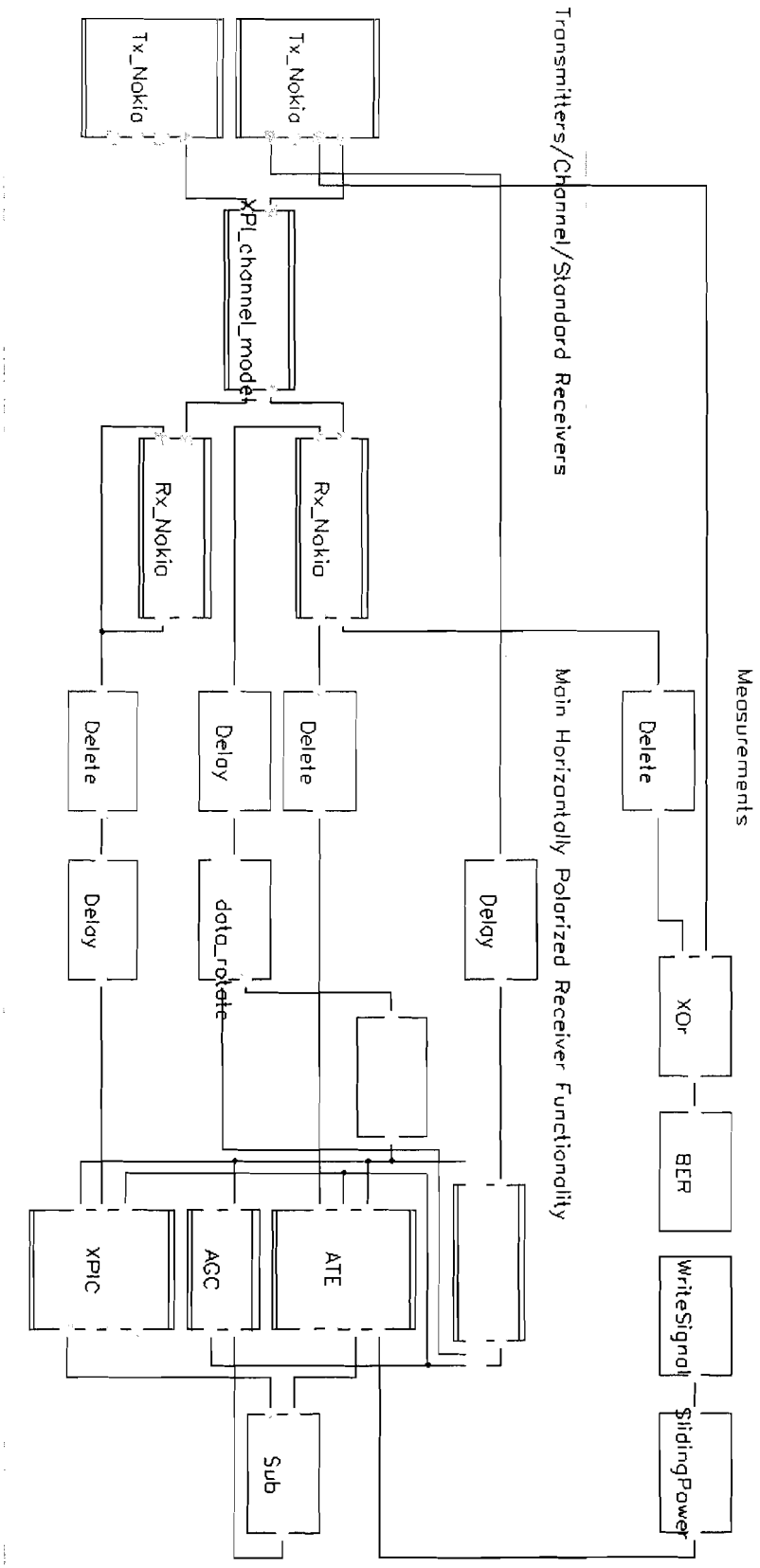

Figure 57: Top-level simulation environment

An overview of the transmitters, the channel and the standard receivers is given in Figure 58, including the I/Os of the sub-blocks. The in- and output signals are explained in Table 2. The transmitter, channel model and receiver sub-blocks are depicted in more detail in Figure 59 to Figure 63, their parameters are explained in Table 3 to Table 5.

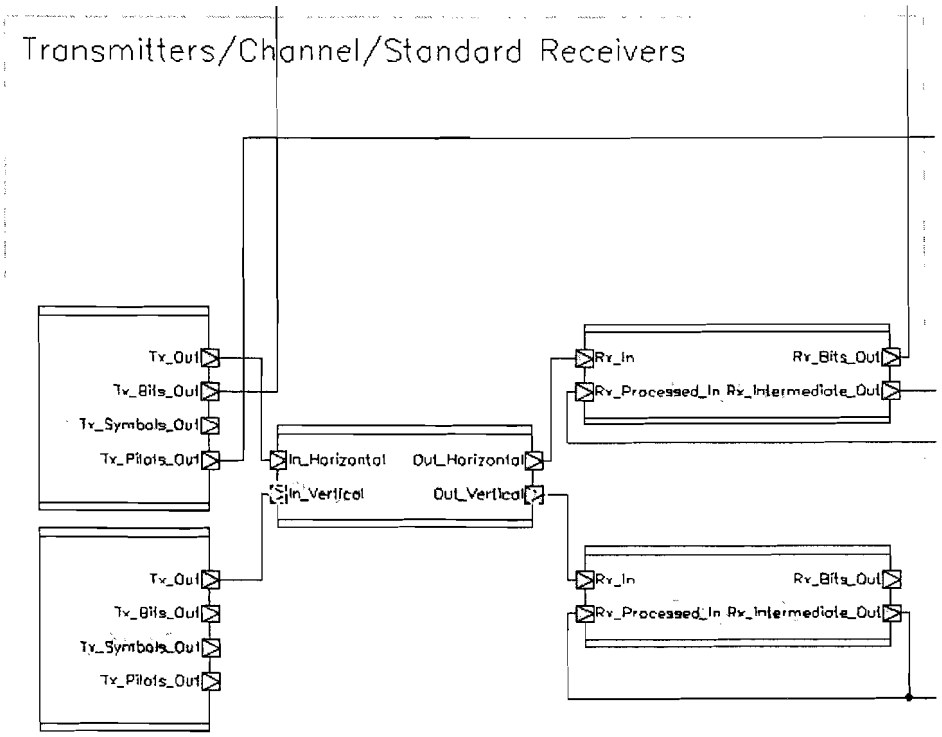

Figure 58: Overview of the transmitter, the channel and the standard receivers

Table 2: In- and output signals of the sub-blocks in Figure 58.

Signal	Type	Description
Tx_out	`complex_float`	Actual output of the transmitter
Tx_Bits_out	`bool`	Transmitter output of the source bits
Tx_Symbols_out	`complex_float`	Transmitter output of the data symbols (the QAM encoded source bits)
Tx_Pilots_out	`complex_float`	Transmitter output of the QPSK encoded pilot symbols
In_Horizontal	`complex_float`	Channel input of the horizontally polarized transmitter
In_Vertical	`complex_float`	Channel input of the vertically polarized transmitter

Out_Horizontal	complex_float	Channel output for the horizontally polarized receiver
Out_Vertical	complex_float	Channel output for the vertically polarized receiver
Rx_In	complex_float	Receiver input
Rx_Intermediate_Out	complex_float	Receiver output of the pulse shaped and downsampled signal
Rx_Processed_In	complex_float	Receiver input of the processed signal by ATE, XPIC, AGC and PE
Rx_Bits_Out	bool	Receiver output of the bits (the QAM decoded processed signal)

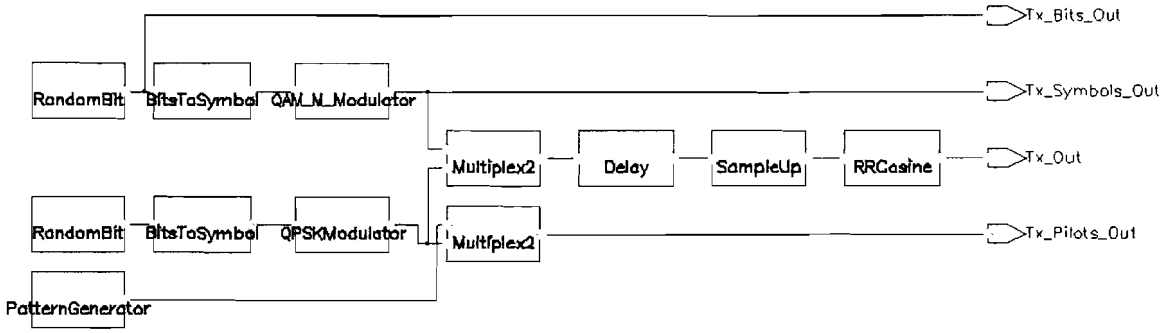

Figure 59: Transmitter architecture

Table 3: Parameters of the transmitter

Parameter	**Type**	**Description**
M_QAM	int	Number of QAM constellation points
Pilot_Spacing	int	The pilot spacing
Delay	int	Delay that enables the horizontally and vertically polarized transmitter to work asynchronious
Upsample_Factor	int	Upsample factor N in the horizontally and vertically polarized transmitters
Cutoff	double	Cutoff frequency of the pulse shaping filter (normalized to the sample rate)
Rolloff	double	Rolloff of the pulse shaping filters in horizontally and vertically polarized transmitters and receivers

FFTLength	int	Specifies the number of points of the pulse shape filters in FFT domain
Gain	double	Gain of the pulse shaping filter, enables compensation of the attenuation caused by upsampling and filtering of the signal
Symbol_Seed	unsigned	Seed of the random bit symbol source
Pilot_Seed	unsigned	Seed of the random bit pilot source

The XIF multipath simulations pointed out that the pilots in the horizontally and vertically polarized transmitters needed to be asynchronous, otherwise the functionality of the ATE and the XPIC is interchanged for deep notches. The parameter Delay in the transmitter makes this possible.

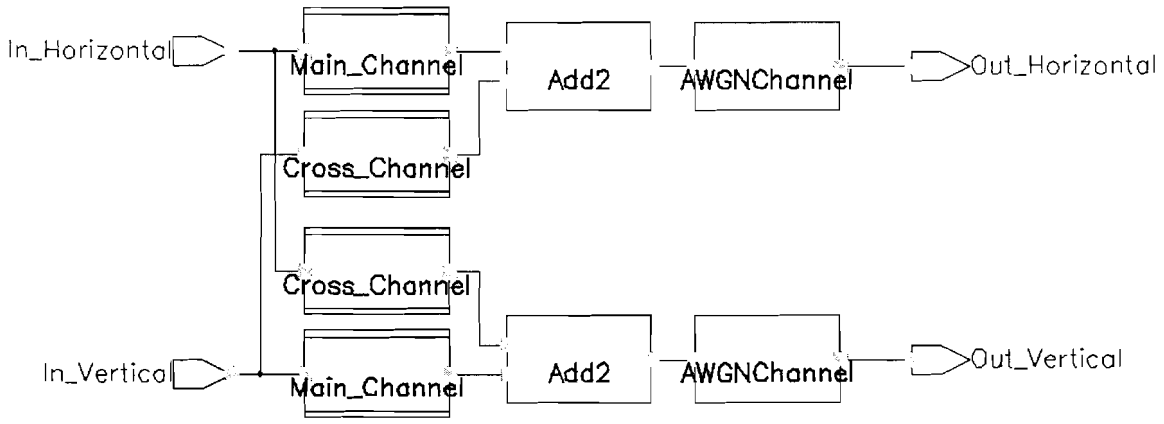

Figure 60: XPI channel architecture

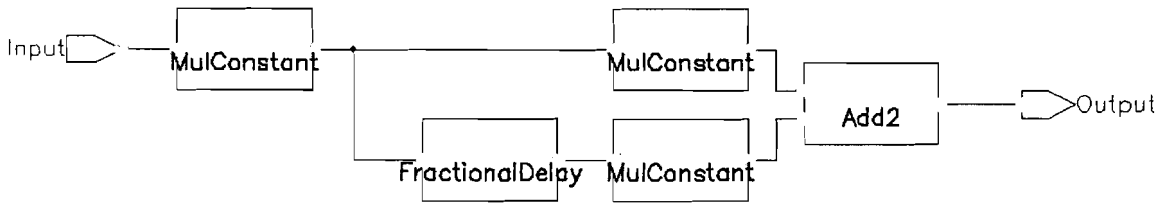

Figure 61: Main channel architecture

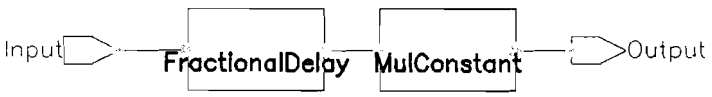

Figure 62: Cross channel architecture

Table 4: Parameters of XPI channel

Parameter	Type	Description
Scale_Parameter_H	`float`	Scale parameter b_H of the horizontally polarized Rummler (main) channel
Scale_Parameter_V	`float`	Scale parameter b_V of the vertically polarized Rummler (main) channel
Scale_Parameter_HV	`float`	Scale parameter b_{HV} of the cross channel from horizontal polarization to vertical polarization
Scale_Parameter_VH	`float`	Scale parameter b_{VH} of the cross channel from horizontal polarization to vertical polarization
Shape_Parameter_H	`float`	Shape parameter c_H of the Rummler channel in horizontal polarization
Shape_Parameter_V	`float`	Shape parameter c_V of the Rummler channel in vertical polarization
Phase_Shift_H	`float`	Phase shift φ_H representing the notch position of the horizontally polarized Rummler channel
Phase_Shift_V	`float`	Phase shift φ_V representing the notch position of the vertically polarized Rummler channel
Phase_Shift_HV	`float`	Phase shift φ_{HV} of the cross channel from horizontal to vertical polarization
Phase_Shift_VH	`float`	Phase shift φ_{VH} of the cross channel from vertical to horizontal polarization
Time_Delay_H	`double`	Delay difference τ_H between direct path and indirect path of the horizontally polarized Rummler channel
Time_Delay_V	`double`	Delay difference τ_V between direct path and indirect path of the vertically polarized Rummler channel
Time_Delay_HV	`double`	Delay difference τ_{HV} between cross channel and the direct path of the horizontally polarized Rummler channel
Time_Delay_VH	`double`	Delay difference τ_{VH} between cross channel and the direct path of the

		vertically polarized Rummler channel
Noise_Power_H	double	Variance of the noise source in horizontally polarized channel branch
Noise_Power_V	double	Variance of the noise source in vertically polarized channel branch
Upsample_Factor	int	Upsample factor N, needed for adjusting the noise power according to the symbol rate
Seed_H	int	Seed of the random noise generator in the horizontally polarized channel path
Seed_V	int	Seed of the random noise generator in the vertically polarized channel path

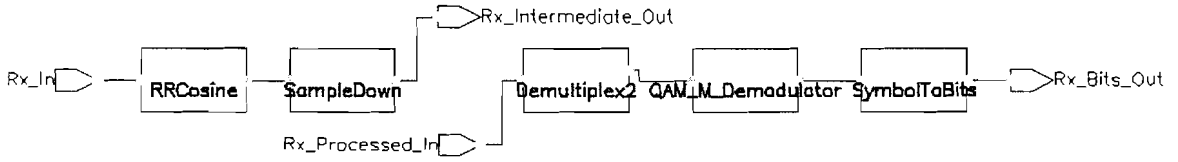

Figure 63: Standard receiver architecture

Table 5: Parameters of the standard receiver

Parameter	**Type**	**Description**
Cutoff	double	Cutoff frequency of the pulse shaping filter (normalized to the sample rate)
Rolloff	double	Rolloff of the pulse shaping filters in horizontally and vertically polarized transmitters and receivers
FFTLength	int	Specifies the number of points of the pulse shape filters in FFT domain
Gain	double	Gain of the pulse shaping filter
Pilot_Spacing	int	The pilot spacing, needed for the demultiplexer to separate the pilots and the data
Downsample_Factor	int	Downsample factor N/L in the horizontally and vertically polarized transmitters
M_QAM	int	Number of QAM constellation points

An overview of the main architecture of the horizontally polarized receiver –the PE dependent blocks are covered– is depicted in Figure 64, including the I/Os of the sub-blocks. The in- and output signals of the main sub-blocks are explained in Table 6. The main sub-blocks –except for the PE– are depicted in more detail in Figure 65 to Figure 67, their parameters are respectively explained in Table 7 to Table 1.

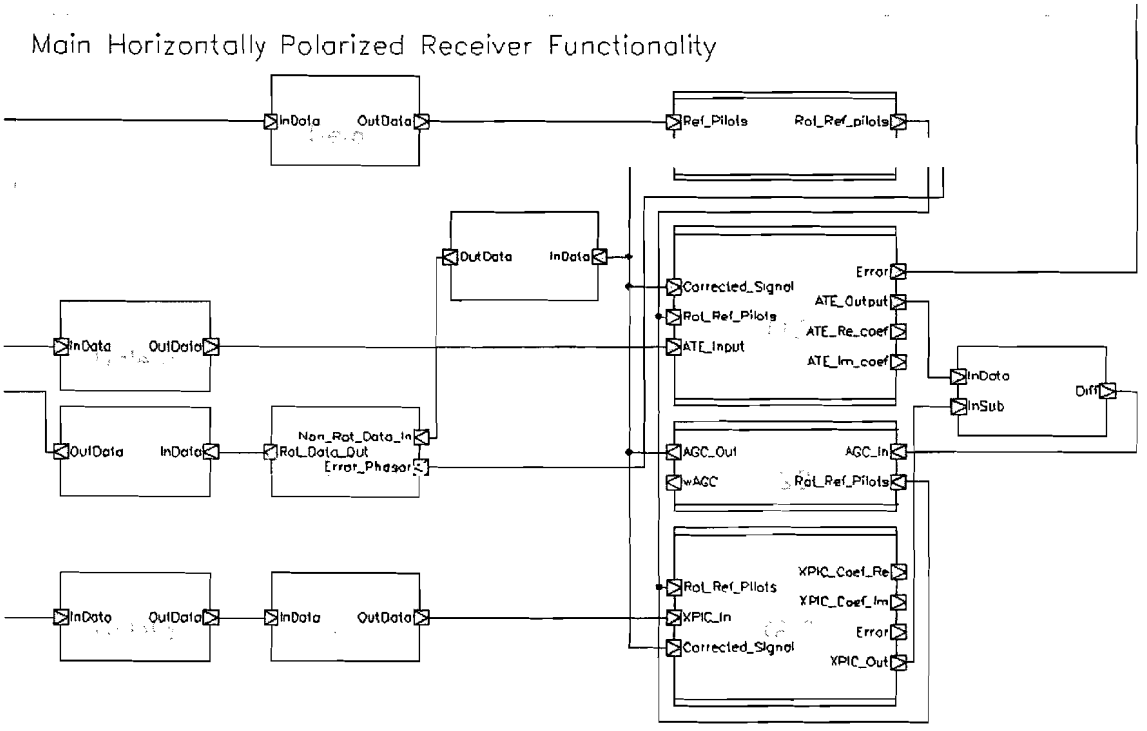

Figure 64: Main architecture of the horizontally polarized receiver

Table 6: In- and output signals of the main sub-blocks in Figure 64.

Signal	Type	Description
ATE_Input	complex_float	Filter input for the ATE.
ATE_Output	complex_float	Equalized output of the ATE
ATE_Re_coef	float	Real coefficients of the ATE
ATE_Im_coef	float	Imaginary coefficients of the ATE
XPIC_In	complex_float	Filter input for the XPIC.
XPIC_Out	complex_float	XPI cancellation output of the XPIC
XPIC_Coef_Re	float	Real coefficients of the XPIC
XPIC_Coef_Im	float	Imaginary coefficients of the XPIC
AGC_In	complex_float	Input to the AGC, the equalized and XPI cancelled signal

AGC_Out	complex_float	Output of the AGC, the gain corrected signal
wAGC	float	Real AGC coefficient
Ref_Pilots	complex_float	QPSK encoded reference pilots, derived from the transmitter
Rot_Ref_Pilots	complex_float	Phase ξ rotated QPSK encoded reference pilots
Corrected_Signal	complex_float	Represents the ISI, XPI and gain corrected signal $z_H(n)$ of the horizontally polarized receiver
Error	complex_float	Error signal $e_H(n)$ of the horizontally polarized receiver for updating the taps of the ATE and XPIC
Non_Rot_Data_In	complex_float	corrected signal $z_H(n)$
Error_Phasor	complex_float	Error phasor for each data symbol, output by the PE
Rot_Data_Out	complex_float	Phase error corrected data

The Filter input for the ATE is the intermediate output of the horizontally polarized standard receiver after eliminating (2*FFTLength/4)/Downsample_Factor_H of samples, necessary due to the overlap-save technique used for pulse shape filtering.

The same applies for the filter input for the XPIC, with the difference that the intermediate output of the vertically polarized standard receiver is used. Thus eliminating (2*FFTLength/4)/Downsample_Factor_V of samples. The extra delay in front of the XPIC can be used to shift the centertap of the XPIC.

The XPI cancellation output of the XPIC is subtracted from the equalized ATE output.

The reference pilots are delayed by the ATE's centertap delay D to achieve synchronized reference pilots and data pilots.

The rotated (phase corrected) data is delayed for synchronization purpose of the demultiplexer in the standard receiver.

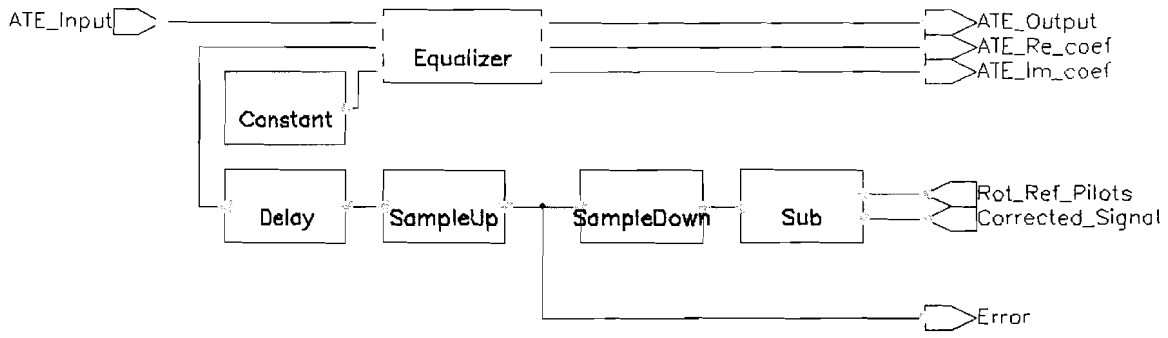

Figure 65: ATE architecture

Table 7: Parameters of the ATE

Parameter	Type	Description
Pilot_Spacing	`int`	The Pilot Spacing, selecting the rate of the down- and upsamplers. In this way only the pilots are extracted
Centertap_Delay	`int`	Delay of D symbols, serves as time shift for the down- and upsamplers
ATE_Oversample_Factor	`long`	Oversample factor of the input data, equal to the Upsample_Factor in the transmitter divided by the Downsample_Factor in the horizontally polarized receiver
ATE_Stepsize_Parameter	`float`	The step-size parameter of the LMS algorithm of the ATE
Num_Coeffs	`long`	Specifies the number of coefficients of the ATE
Fix_Center	`bool`	High when the center coefficient of the ATE is fixed
Center_Position	`long`	Coefficient number of the center tap

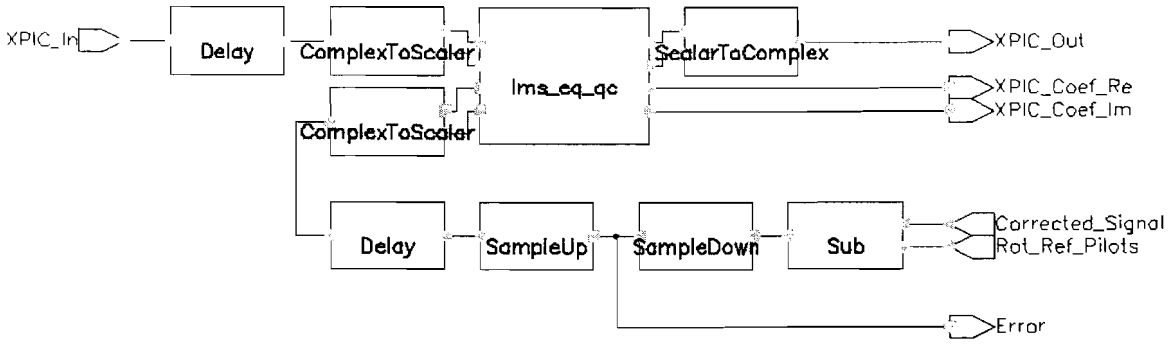

Figure 66: XPIC architecture

Table 8: Parameters of the XPIC

Parameter	Type	Description
Pilot_Spacing	`int`	The Pilot Spacing, selecting the rate of the down- and upsamplers. In this way only the pilots are extracted
Centertap_Delay	`int`	Delay of D symbols, serves as time shift for the down- and upsamplers
XPIC_Oversample_Factor	`int`	Oversample factor of the input data, equal to the Upsample_Factor in the transmitter divided by the Downsample_Factor in the vertically polarized receiver
XPIC_Stepsize_Parameter	`float`	The step-size parameter of the LMS algorithm of the XPIC
XPIC_Initial_Coefficients	`input_data set`	Specifies the initial coefficients of the XPIC

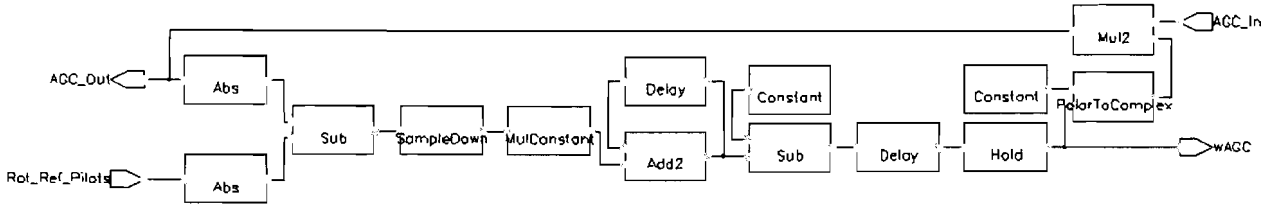

Figure 67: AGC architecture

Table 9: Parameters of the AGC

Parameter	Type	Description
Pilot_Spacing	int	The Pilot Spacing, selecting the rate of the downsampler. In this way only the pilots are extracted
Centertap_Delay	int	Delay of D symbols, serves as time shift for the downsampler
K	float	Loop parameter K, comparable with the step-size parameters of the ATE and XPIC

Figure 68 shows two kind of measurements. The Bit Error Rate (BER) measurement, which compares of course the transmitted bits with the received bits. The error power measurement, measuring the power of the error signal used for ATE and XPIC.

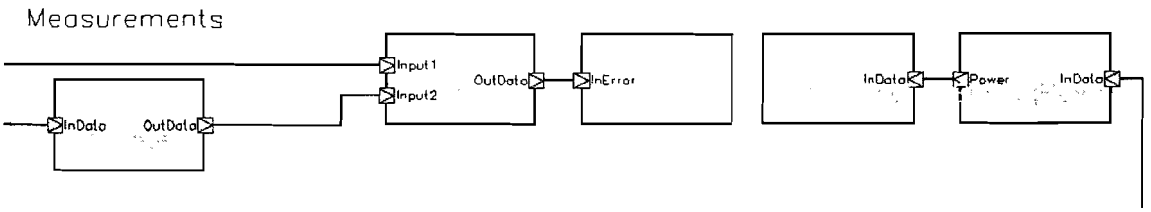

Figure 68: Measurements

The delete block deletes a number of zeros caused by delay blocks in front.

The sliding power block averages the error power over a number of samples for smoothing purposes.